

EMAE/TR-90-200

Catalytic Ignition Model in a Monolithic  
Reactor with In-Depth Reaction

by

Ta-Ching Tien

and

James S. T'ien

Department of Mechanical and Aerospace Engineering  
Case Western Reserve University  
Cleveland, Ohio 44106

December 1990

Final Technical Report

Prepared for

National Aeronautics and Space Administration  
Lewis Research Center  
Under Grant NAG 3-809

CATALYTIC IGNITION MODEL IN A MONOLITHIC REACTOR  
WITH IN-DEPTH REACTION

ABSTRACT

Two transient models have been developed to study the catalytic ignition in a monolithic catalytic reactor. The special feature in these models is the inclusion of thermal and species structures in the porous catalytic layer. There are many time scales involved in the catalytic ignition problem, and these two models are developed with different time scales. In the full transient model, the equations are non-dimensionalized by the shortest time scale (mass diffusion across the catalytic layer). It is therefore accurate but is computationally costly. In the energy-integral model, only the slowest process (solid heat-up) is taken as nonsteady. It is approximate but computationally efficient.

In the computations performed, the catalyst is platinum and the reactants are rich mixtures of hydrogen and oxygen. One-step global chemical reaction rates are used for both gas-phase homogeneous reaction and catalytic heterogeneous reaction. The computed results reveal the transient ignition processes in detail, including the

structure variation with time in the reactive catalytic layer. An ignition map using reactor length and catalyst loading is constructed.

The comparison of computed results between the two transient models verifies the applicability of the energy-integral model when the time is greater than the second largest time scale of the system. It also suggests that a proper combined use of the two models can catch all the transient phenomena while minimizing the computational cost.

#### **ACKNOWLEDGMENTS**

This work was supported by NASA Grant 3-809. We would like to extend our appreciation to Mr. Robert Zurawski, the first technical monitor of this project, for his interest, encouragement, and help; to Ms. Elizabeth Armstrong, the present technical monitor of this grant, for her patience and assistance, and to Mr. James Green and Mr. Gary Williamson for their help during the course of this research. This report is based on the Ph.D. thesis of Ta-Ching Tien.

## TABLE OF CONTENTS

	Page
ABSTRACT	ii
ACKNOWLEDGEMENTS	iv
TABLE OF CONTENTS	v
LIST OF FIGURES	vii
LIST OF TABLES	xi
NOMENCLATURE	xii
CHAPTER I INTRODUCTION	1
1.1 A Description of Catalytic Ignition in a Monolithic Reactor	1
1.2 Literature Review	2
1.3 Present Model	5
CHAPTER II MODEL DEVELOPMENT	7
2.1 Introduction	7
2.2 Governing Equations	9
2.3 Choice of Reference Time Scales	20
2.4 Full Transient Model	21
2.5 Energy-Integral Model	23
CHAPTER III NUMERICAL SCHEME	29
3.1 Full Transient Model Treatment	29
3.2 Energy-Integral Model Treatment	34
CHAPTER IV RESULTS AND DISCUSSIONS	39
4.1 Introduction	39
4.2 General Transient Behavior	40
4.3 The Effect of Catalyst Loading	43
4.4 The Effect of Mixture Fuel/Oxidizer Equivalence Ratio	48
4.5 The Cause of Non-Uniformity in the Solid	49
4.6 Computed Results Using Energy-Integral Model	52
CHAPTER V CONCLUSION	59

REFERENCES	61
APPENDIX A DETERMINATION OF CHEMICAL REACTION RATES	64
A.1 Introduction	64
A.2 Gas-Phase Reaction Rate	65
A.3 Catalytic Reaction Rate	69
A.4 Summary	70
APPENDIX B DAMKÖHLER ANALOGY	71
APPENDIX C DERIVATION OF FINITE DIFFERENCE EQUATIONS	73
APPENDIX D COMPUTER PROGRAMS	82
D.1 Flow Chart	82
D.2 Programs	83
TABLES	103
FIGURES	110

## LIST OF FIGURES

Figure	Page
1 Monolithic reactor model description	110
2 Transient profiles for Case 1 at $t^* = 10, 50, 100 \tau_m^*$ $(\beta^* = 1.8 \text{ kg-pt/m}^3, L^* = 5 \text{ cm}, \phi = 8)$	111
3 Solid contours for Case 1 at $t^* = 10 \tau_m^*$	112
4 Solid contours for Case 1 at $t^* = 50 \tau_m^*$	113
5 Solid contours for Case 1 at $t^* = 100 \tau_m^*$	114
6 Transient profiles for Case 1 at $t^* = 1, 2, 3 \tau_{HT}^*$ $(1 \tau_{HT}^* = 500 \tau_m^*)$	115
7 Solid contours for Case 1 at $t^* = 1 \tau_{HT}^*$	116
8 Solid contours for Case 1 at $t^* = 2 \tau_{HT}^*$	117
9 Solid contours for Case 1 at $t^* = 3 \tau_{HT}^*$	118
10 Transient profiles for Case 2 at $t^* = 5, 7, 15 \tau_{HT}^*$ $(\beta^* = 0.18 \text{ kg-pt/m}^3, L^* = 20 \text{ cm}, \phi = 8)$	119
11 Solid contours for Case 2 at $t^* = 5 \tau_{HT}^*$	120
12 Solid contours for Case 2 at $t^* = 7 \tau_{HT}^*$	121
13 Solid contours for Case 2 at $t^* = 15 \tau_{HT}^*$	122
14 Transient profiles for Case 3 at $t^* = 0.2, 1, 3 \tau_{HT}^*$ $(\beta^* = 18. \text{ kg-pt/m}^3, L^* = 5 \text{ cm}, \phi = 8)$	123
15 Solid contours for Case 3 at $t^* = 0.2 \tau_{HT}^*$	124
16 Solid contours for Case 3 at $t^* = 1 \tau_{HT}^*$	125
17 Solid contours for Case 3 at $t^* = 3 \tau_{HT}^*$	126
18 Ignition boundary map ( $u_\infty = 10 \text{ m/sec}$ )	127

19	Transient profiles for Case 4 at $t^* = 0.2, 1, 2 \tau_{HT}^*$ ( $\beta^* = 1.8 \text{ kg-pt/m}^3$ , $L^* = 5 \text{ cm}$ , $\phi = 4$ )	128
20	Solid contours for Case 4 at $t^* = 0.2 \tau_{HT}^*$	129
21	Solid contours for Case 4 at $t^* = 1 \tau_{HT}^*$	130
22	Solid contours for Case 4 at $t^* = 2 \tau_{HT}^*$	131
23	Solid in-depth temperature profiles for Case 3 at $t^* = 0.2 \tau_{HT}^*$	132
24	Solid in-depth species profiles for Case 3 at $t^* = 0.2 \tau_{HT}^*$	133
25	Solid in-depth temperature profiles for Case 3 at $t^* = 1 \tau_{HT}^*$	134
26	Solid in-depth species profiles for Case 3 at $t^* = 1 \tau_{HT}^*$	135
27	Solid in-depth temperature profiles for Case 3 at $t^* = 3 \tau_{HT}^*$	136
28	Solid in-depth species profiles for Case 3 at $t^* = 3 \tau_{HT}^*$	137
29	Solid in-depth temperature profiles for Case 4 at $t^* = 0.2 \tau_{HT}^*$	138
30	Solid in-depth species profiles for Case 4 at $t^* = 0.2 \tau_{HT}^*$	139
31	Solid in-depth temperature profiles for Case 4 at $t^* = 1 \tau_{HT}^*$	140
32	Solid in-depth species profiles for Case 4 at $t^* = 1 \tau_{HT}^*$	141
33	Solid in-depth temperature profiles for Case 4 at $t^* = 2 \tau_{HT}^*$	142

34	Solid in-depth species profiles for Case 4 at $t^* = 2 \tau_{HT}^*$	143
35	Comparisons of two models for Case 1 on $T_g$ at $t^* = 1, 2, 3 \tau_{HT}^*$	144
36	Comparisons of two models for Case 1 on $y_g$ at $t^* = 1, 2, 3 \tau_{HT}^*$	145
37	Comparisons of two models for Case 1 on $W_g^*$ at $t^* = 1, 2, 3 \tau_{HT}^*$	146
38	Solid contours for Case 1 at $t^* = 1 \tau_{HT}^*$ by energy integral model	147
39	Comparisons of two models for Case 1 on solid in-depth temperature at $t^* = 1 \tau_{HT}^*$	148
40	Comparisons of two models for Case 1 on solid in-depth species at $t^* = 1 \tau_{HT}^*$	149
41	Solid contours for Case 1 at $t^* = 2 \tau_{HT}^*$ by energy integral model	150
42	Comparisons of two models for Case 1 on solid in-depth temperature at $t^* = 2 \tau_{HT}^*$	151
43	Comparisons of two models for Case 1 on solid in-depth species at $t^* = 2 \tau_{HT}^*$	152
44	Solid contours for Case 1 at $t^* = 3 \tau_{HT}^*$ by energy integral model	153
45	Comparisons of two models for Case 1 on solid in-depth temperature at $t^* = 3 \tau_{HT}^*$	154
46	Comparisons of two models for Case 1 on solid in-depth species at $t^* = 3 \tau_{HT}^*$	155

47	Comparisons of two models for Case 3 on $T_g^*$ at $t^* = 0.2, 1, 3 \tau_{HT}^*$	156
48	Comparisons of two models for Case 3 on $y_g^*$ at $t^* = 0.2, 1, 3 \tau_{HT}^*$	157
49	Comparisons of two models for Case 3 on $W_g^*$ at $t^* = 0.2, 1, 3 \tau_{HT}^*$	158
50	Solid contours for Case 3 at $t^* = 0.2 \tau_{HT}^*$ by energy integral model	159
51	Comparisons of two models for Case 3 on solid in-depth temperature at $t^* = 0.2 \tau_{HT}^*$	160
52	Comparisons of two models for Case 3 on solid in-depth species at $t^* = 0.2 \tau_{HT}^*$	161
53	Solid contours for Case 3 at $t^* = 1 \tau_{HT}^*$ by energy integral model	162
54	Comparisons of two models for Case 3 on solid in-depth temperature at $t^* = 1 \tau_{HT}^*$	163
55	Comparisons of two models for Case 3 on solid in-depth species at $t^* = 1 \tau_{HT}^*$	164
56	Solid contours for Case 3 at $t^* = 3 \tau_{HT}^*$ by energy integral model	165
57	Comparisons of two models for Case 3 on solid in-depth temperature at $t^* = 3 \tau_{HT}^*$	166
58	Comparisons of two models for Case 3 on solid in-depth species at $t^* = 3 \tau_{HT}^*$	167
59	Transient profiles for Case 5 at $t^* = 1, 2, 3 \tau_{HT}^*$ ( $\beta^* = 1.8 \text{ kg-pt/m}^3$ , $L^* = 5 \text{ cm}$ , $\phi = 8$ , $\tau_{HT}^* = 2 \text{ sec}$ )	168
A.1	Comparisons of ignition delay time between model predicted by Eqs. (A.10), (A.11) and experimental data [14], [15].	169

## LIST OF TABLES

Table	PAGE
1 Estimate of transient time scales in a monolithic reactor	103
2 List of time scales and nondimensional parameters in Case 1	105
3 Parameteric studies	106
4 List of property values in Case 1	107
5 List of operating parameters in Case 1	108
A.1 Parameters for two sets of gas-phase reaction rates	109

## NOMENCLATURE

$A^*$	Crosssectional area of one gas channel, $m^2$
$A^*$	Solid crosssectional area associated with one gas channel, $m^2$
$a$	Exponent of pressure for gas-phase reaction rate
$B_1^*$	$L_g^* K_g^* P^{*a} \rho^{*b}(0,0) Y_g^{*b-1}(0,0) / \rho^*(0,0) u^*(0,0)$
$B_2^*$	$B_1^* Y_g(0,0)$
$B_c$	$h_t^* h_c^* / \lambda_c^*$ Biot number.
$b$	Exponent of oxygen density for gas-phase reaction rate
$C^*$	Specific heat of catalytic layer or substrate layer, cal/kg/ $^{\circ}$ K
$C_p^*$	Specific heat of gas-phase mixture, cal/kg/ $^{\circ}$ K
$D_e^*$	Oxygen effective diffusivity, $m^2/sec$
$D_{am}$	Damköhler number of gas.
$D_{am}'$	$D_{am} / Y_g(0,0)$
$D_{at}$	Damköhler number of solid.
$D_{at}'$	$D_{at} q_c$
$d^*$	Monolithic reactor channel equivalent diameter, m
$d_s^*$	Half thickness of the solid, m
$E^*$	Activation energy, cal/mole
$J_D$	$J_H (L_e)^{2/3}$
$J_H$	$4 \text{ Nu}_x^* (\alpha_g^*(0,0)/d^{*2}) (L^*/u^*(0,0)) (\lambda_g^*/\lambda_g^*(0,0))$

$h^*$	Thickness of layer, m
$h^*$	Mass transfer coefficient between gas in the channel and catalytic surface, m/sec
$h^*$	Heat transfer coefficient between gas in the channel and catalytic surface, cal/m <sup>2</sup> /sec/°K
$L^*$	Reactor bed length, m
$L_e$	Lewis number of oxygen
M	Molecular weight, g/mole
$Nu_x$	Nusselt number at x
$Nu_\infty$	Nusselt number for fully developed flow.
$p^*$	Pressure, atm
$P^*$	$P^*/P^*(0,0)$ . Nondimensional pressure
$q^*$	Dimensional heat of combustion per unit mass of mixture, cal/kg
$q_g^*$	$q^*/C_p^*T_g^*(0,0)$ . Nondimensional heat of combustion per unit mass of mixture in gas-phase reaction.
$q_c^*$	$q^*/C_c^*T_g^*(0,0)$ . Nondimensional heat of combustion per unit mass of mixture in catalytic reaction.
$R^*$	Universal gas constant, atm-m <sup>3</sup> /kg/°K
$r_c^*$	Radial distance from the center of gas channel to the surface of substrate layer, m
$r_d^*$	Radius of gas channel, m
$r_s^*$	Radial distance from the center of gas channel to the bottom of substrate layer, m
$r_{nk}$	$Nu_x \lambda_g^* / Nu_\infty \lambda_g^*(0,0)$

$S^*$	Circumferential length of one channel cross-section, m
$Sh$	$h_d^* h_c^* / D_e^*$ Sherwood number.
$T$	$T_g^*/T_{g^*}(0,0)$ Nondimensional temperature
$t$	$t^*/\tau^*$ Nondimensional time.
$u^*$	Gas mixture velocity, m/sec
$u^*$	$u^*/u^*(0,0)$ Nondimensional velocity.
$u_{ref}^*$	Reference gas velocity, measured at entrance of reactor.
	$u^*(0,0) = u_{ref}^* A_T^* / A^*$
$w^*$	Chemical reaction rate, $\text{kg-O}_2/\text{m}^3/\text{sec}$
$x^*$	$x^*/L^*$ Nondimensional axial distance measured from entrance of reactor.
$Y$	Mass fraction of oxygen.
$Y_g$	Mass fraction of oxygen in gas channel.
$Y_c$	Mass fraction of oxygen in catalytic layer.
$y$	$Y/Y(0,0)$
$\alpha^*$	Thermal diffusivity, $\text{m}^2/\text{sec}$
$\beta^*$	Catalyst loading, $\text{kg-Pt}/\text{m}^3$
$\lambda^*$	Heat conductivity, $\text{cal}/\text{m/sec}^{\circ}\text{k}$
$\rho_o^*$	Oxygen density, $\text{kg}/\text{m}^3$
$\rho^*$	Dimensional gas density, $\text{kg}/\text{m}^3$
$\rho^*$	$\rho^*/\rho^*(0,0)$ Nondimensional gas density.
$\epsilon$	Porosity of catalytic layer.
$\tau_r^*$	$(L^*/u_{ref}^*)(A^*/A_T^*)$ Gas residence time in reactor, sec

$\tau_m^* \in h_c^{*2}/D_e^*(0,0)$  Mass diffusion time in catalytic layer, sec

$\tau_t^* h_c^{*2}/\alpha_c^*$  Thermal diffusion time in catalytic layer, sec

$\tau_s^* h_s^{*2}/\alpha_s^*$  Thermal diffusion time in substrate layer, sec

$\tau_{HT}^* 2 \int_{r_d^*}^{r_s^*} \rho^* C^* r^* dr^*/Nu_\infty \lambda_g^*(0,0)$  Solid heat-up time, sec

$\delta_c \tau_t^* / \tau_m^*$

$\delta_s h_c^{*2}/\alpha_s^* / \tau_m^*$

$\delta_g L^* / u^*(0,0) / \tau_m^*$

#### Subscript

$g$  Gas-phase property.

$c$  Catalytic layer property

$o$  Oxygen

$s$  Substrate layer property.

$c,s$  Property on catalytic layer surface

#### Superscript

$n$  Time level

$*$  Dimensional quantity.

## CHAPTER I

### INTRODUCTION

#### 1.1 A Description of Catalytic Ignition in a Monolithic Reactor

The catalytic combustor is a device which uses a catalytic active metal on the reactor surface to initiate and stabilize the combustion process. The granular bed catalytic igniter has been in use for many years in small monopropellant rocket thrusters for the altitude control of satellites [1]. The use of monolithic bed catalytic combustors has been considered in gas turbines [2]. Recently, there has been interest in adopting a monolithic reactor for the ignition of hydrogen/oxygen mixture in rockets [3]. This monolithic reactor has the potential of higher performance and longer catalyst life. A monolithic catalytic reactor consists of a solid substrate block with parallel channels (e.g. honeycomb). On the surface of the channel, a layer of porous material is coated. Within the pores, catalysts are deposited. One popular example is the use of platinum catalyst on alumina.

In this work, ignition transient in a monolithic reactor is simulated. The model includes several parts : a non-reactive, impermeable solid substrate; a gas phase in the channel capable of homogeneous reaction; and in between, a porous catalytic layer where gaseous reactants can diffuse into and catalytically react. The

catalytic combustion processes in a monolithic reactor can be described in two phases:

(I) Initially, a premixed fuel/oxidizer mixture is introduced into the reactor, gas reactants diffuse into the porous catalytic layer and are absorbed, a heterogeneous chemical reaction occurs with the help of the catalyst, and heat is released and transferred to the gas phase and substrate. At this stage, the gas-phase reaction is unimportant; it is catalytic-reaction controlled. After a short period of time, a sharp increase of heterogeneous reaction rate can be observed which characterizes the catalytic ignition.

(II) Following phase I, the gas in the channel is gradually heated up by the catalytic layer, and the gas-phase reaction becomes active. Eventually, a sharp increase in the gas reaction rate occurs which characterizes the gas-phase ignition, and it ends phase II. Once the gas is ignited, the reactor goes to steady state rapidly, and all of the reactants are consumed completely short distance after the gas-phase ignition point.

### 1.2 Literature Review

Mathematical models applicable to a catalytic combustor can be divided into two categories : steady-state models and transient models. The most comprehensive steady-state model was one developed by Kelly, et al. [4]. It is one-dimensional and includes

homogeneous and heterogeneous reactions. In addition, the solid heat conduction, radiation and axial diffusion are considered. Their predictions show that the homogeneous reactions in catalytic combustors are " flame-like " and that beyond a certain mass flow rate they are extinguished. The model successfully predicts the effect of design parameters such as channel diameter and inlet gas temperature on operating characteristics such as blowout and breakthrough. For transient models, T'ien [5] was the first one to deal with a monolithic reactor. He developed a quasi-steady, one-dimensional model in which the substrate energy equation is assumed to be transient while the gas-phase energy and species equations are the steady ones. This assumption is based on the fact that the longest characteristic time scale in the monolithic reactor, because of its nature large thermal inertia, is the substrate heat-up time. In addition, heat conduction along flow direction in the gas channel and the solid are neglected for high speed flow. This model correctly predicts transient behavior and is highly efficient in computation. Sinha, et al. [6] proposed a complete coupled two-dimensional transient equation for both the gas and solid phases. But the computation time was too long for parametric studies and the quasi-steady gas phase approximation was used for practical purpose. Prasad, et al. [7] developed a one-dimensional transient model incorporating axial conduction and heat losses but neglecting radiation. For small times, the model is

fully transient and solves time-dependent equations for solid temperature, gas temperature, and gas species concentration. However, because of the small time step needed to solve these equations, making the solution computationally expensive, a quasi-steady model is used as in [5]. One of findings using this model is that the length required for achieving complete conversion in steady-state operation is shorter than that required in transient operation. Kesten, et al. [8] developed a two-dimensional full transient model which permits computation of concentration and temperature in the bulk gas phase and within porous catalyst particles. This model was applied in a reactor packed with porous catalyst particles; the reactants were rich-hydrogen/oxygen mixtures.

Much of the modeling work on the monolithic catalytic combustor has assumed that heterogeneous reactions occurred on the surface of catalytic layer only. In reality, the catalyst particles are deposited in the pores and during reaction there can be a concentration and thermal structure within that layer. Problems involved concentration and temperature transients in a catalyst pellet [9,10] which, used extensively in chemical reactors and automobile converters, has been studied experimentally and theoretically in chemical engineering literature. These results have shown the existence of temperature and concentration gradients inside the pellet because of porous structure effect. They suggest

that an improved monolithic catalytic combustion model can be made by incorporating a porous catalytic layer with finite thickness. A more detailed literature review for catalytic combustion is offered by Pfefferle and Pfefferle [11].

### **1.3 Present Model**

Two transient models have been developed in this work to study the ignition process in a monolithic catalytic reactor. A rich hydrogen/oxygen mixture is used as the reactant, and the catalyst is platinum. One-step global reaction rates are used in both the homogeneous and the heterogeneous reactions. These models differ from the previous ones in that they include the effect of a finite porous catalytic layer, where reactants' diffusion, consumption and heat conduction are important for the results of ignition phenomena.

Two models are developed because of the consideration of computational time. In the first model, all transient processes are included. It is therefore a more complete model but is computationally costly. A second model is formulated with only the longest transient (solid heat-up) included in the unsteady term. It is more computational efficient and is a direct extension of the work in [5].

In chapter II, these models are formulated. Numerical methods are presented in Chapter III. Computed results using both models are given in Chapter IV, both for clarifying the transient ignition

process and for comparing the predictions from two models.

## CHAPTER II

### MODEL DEVELOPMENT

#### 2.1 Introduction

A monolithic reactor is composed of many uniform parallel channels; if the reactor is well insulated, then the study of the whole reactor can be reduced to the consideration of a single cell unit. Each cell consists of an open gas channel and an associated solid fraction (Fig. 1a). The solid is composed of two parts : a porous catalytic layer where catalysts are deposited in the pores (Fig. 1b) and an impermeable solid substrate which provides monolith support. Commercially, the porous layer is often referred to as the washcoat because the catalysts are distributed inside the pores, reactants have to diffuse into the pore before being absorbed on the surface and reacted catalytically. The rate of in-depth reaction can therefore be regulated by the diffusion rate inside the pore. On the other hand, although the substrate does not directly participate in the reaction, during transient ignition, its large thermal inertia can have a great influence on the catalyst temperature and the catalytic reaction rate. The heat transfer through the solid and its heat-up process therefore have to be included in the ignition model. Figure 1c specifies the symbol designations for the dimensions of gas channel, catalytic and

substrate layers. Although the model to be presented can be a variety of transient catalytic combustion processes, the particular calculations performed are for the start-up ignition transient of a rich-hydrogen/oxygen mixture. It is assumed in the theoretical calculation that the reactor is filled with hydrogen; then the deficient species oxygen is admitted at a rate which yields a specified mixture mass ratio. The oxygen convects downstream through the gas channel. In the meantime, it diffuses into the pores in the catalytic layer and becomes absorbed. Catalytic reaction occurs with a rate depending on the local oxygen concentration and temperature. The heat released from the reaction is conducted through the catalytic layer to both the substrate layer and the gas in the channel. As the gas temperature is raised sufficiently, the gas-phase reaction is initiated. This process quickly increases the gas temperature further to that of the adiabatic flame temperature and the ignition is completed.

It is clear that transient phenomena in the monolithic catalytic combustor are complex due to many time scales involved. Following T'ien [5], Table 1 defines these characteristic times and their estimated magnitudes. Several new time scales, which account for the in-depth heat/mass transfer processes in the catalytic layer, are added or modified. Added are the heat and mass transfer scales in the porous layer. The heterogeneous reaction, previously regarded as a surface reaction, is now treated as a volumetric

reaction.

An one-step overall heterogeneous reaction rate in the catalytic layer is adopted from available experimental data [12-14]. The experimental results show that in a hydrogen-rich mixture, the reaction rate depends on the concentration of deficient oxygen only. Therefore, only the species for oxygen is required in the model. The derivation of the catalytic reaction rate expression can be found in Appendix A.3. For the gas-phase reaction, an one-step overall rate is also assumed. The ignition delay data [15-17], matched separately with the expression from the spontaneous ignition theory [18], allows the rate constants to be determined (see Appendix A.2). Although the elementary reaction kinetics for H<sub>2</sub>/O<sub>2</sub> mixture are known, we have adopted the overall rate expression in order to be consistent with the heterogeneous reaction (for which elementary reactions are not fully understood).

## 2.2 Governing Equations

The complete set of equations needed to describe the transient behavior include that (1) the continuity, energy, and species equations in the gas phase; and (2) the energy, species equations in the solid. The following assumptions are made in the derivation of these equations :

- (a) The plug flow approximation is used in the gas channel and the pressure is assumed to be uniform.

- (b) The heat/mass transfer coefficients between the gas and the solid are functions of distance and temperature, and derived from Nusselt number correlation in entrance flow in a tube [19]. A local stagnation flow estimation [4] is made for the first point in the entrance flow.
- (c) Heat conduction and mass diffusion in the axial direction are neglected because the Peclet number based on typical gas velocity ( $\geq 10$  M/S) is much greater than unity [20].
- (d) Radiation heat transfer in both gas and solid phases are neglected.
- (e) An effective diffusion coefficient is used to calculate oxygen diffusion through the porous media. The effective diffusivity is assumed to be proportional to the reciprocal of local gas temperature only, i.e.  $\rho D_e = \text{const.}$  [21].
- (f) The specific heat of mixture is constant.

#### Gas-phase

The general dimensional equations are listed as follows.

equation of state  $P^* = \rho^* R^* T_g^*$  (2.1)

continuity  $\frac{\partial \rho^*}{\partial t^*} + \frac{\partial (\rho^* u^*)}{\partial x^*} = 0$  (2.2)

momentum

$$P^* = P^*(x=0, t=0) \quad (2.3)$$

species       $\rho^* \frac{\partial Y_g}{\partial t} + \rho^* u^* \frac{\partial Y_g}{\partial x} + \frac{h_d^* S^*}{A^*} (Y_g - Y_{c,s}) = W_g^*$       (2.4)

energy       $\rho^* C_p^* \frac{\partial T_g^*}{\partial t} + \rho^* u^* C_p^* \frac{\partial T_g^*}{\partial x} + \frac{h_t^* S^*}{A^*} (T_g^* - T_{c,s}^*) = q^* W_g^*$       (2.5)

where the reaction rate is given by (see Appendix A.3 for results):

$$W_g^* = K^* P^{*a} \rho_{og}^{*b} \exp\left(\frac{-E_g^*}{R T_g^*}\right) \quad (2.6)$$

Defining nondimensional variables by :

$$\begin{aligned} x &= \frac{x^*}{L^*} & t &= \frac{t^*}{\tau^*} & q_g^* &= \frac{q^*}{C_p^* T(0,0)} \\ u &= \frac{u^*}{u(0,0)} & Y_g^* &= \frac{\rho_{og}^*}{\rho^*} & y_g &= \frac{Y_g}{Y_g(0,0)} \\ \rho &= \frac{\rho^*}{\rho(0,0)} & T_g^* &= \frac{T^*}{T(0,0)} & E_g^* &= \frac{E_g^*}{R^* T^*(0,0)} \end{aligned} \quad (2.7)$$

The dimensionless equations are :

$$\text{continuity} \quad \delta_g \frac{\partial \rho}{\partial t} + \frac{\partial (\rho u)}{\partial x} = 0 \quad (2.8)$$

$$\begin{aligned} \text{species} \quad & \rho \delta_g \frac{\partial y_g}{\partial t} + \rho u \frac{\partial y_g}{\partial x} + J_D (y_g - y_{c,s}) \\ & = B_1^* (\rho y_g)^b \exp\left(\frac{-E_g}{T_g}\right) \end{aligned} \quad (2.9)$$

$$\begin{aligned} \text{energy} \quad & \rho \delta_g \frac{\partial T_g}{\partial t} + \rho u \frac{\partial T_g}{\partial x} + J_H (T_g - T_{c,s}) \\ & = q_g B_2^* (\rho y_g)^b \exp\left(\frac{-E_g}{T_g}\right) \end{aligned} \quad (2.10)$$

$$\text{equation of state} \quad P = \rho T_g \quad (2.11)$$

where the length scale in  $x$ -direction is chosen to be the reactor length  $L^*$ , the time scale  $\tau^*$  used for nondimensionalization is yet to be determined, and

$$\delta_g = \frac{L^* / u^*(0,0)}{\tau^*} \quad (2.12)$$

The system of gas-phase equations (2.8) to (2.11) needs initial conditions. In this study, initially the reactor is filled with hydrogen; the start-up is from a step-wise oxygen injection.

Initial conditions

$$\begin{aligned} y_g(x=0, t=0) &= 1 & T_g(x, t=0) &= 1 & (2.13) \\ \rho(x, t=0) &= 1 & u(x, t=0) &= 1 \end{aligned}$$

Solid-phase

Solid phase consists of two layers, a catalytic layer on top of a substrate layer. The dimensional governing equations are :

species in catalytic layer

$$\epsilon r^* \left( \frac{\partial \rho_{oc}^*}{\partial t^*} \right) = - \frac{\partial}{\partial r^*} \left( r^* \rho^* D_e^* \frac{\partial Y_c}{\partial r^*} \right) + r^* \rho^* D_e^* \frac{\partial^2 Y_c}{\partial x^* 2} - r^* W_c^* \quad (2.14)$$

where  $D_e^*$  is the effective oxygen diffusivity and  $D_e^* \propto \frac{T_g^{*\gamma}}{P^*}$ . In this work, we choose  $\gamma=1$  and it gives a constant value for the product  $\rho^* D_e^*$ . Thus Eq. (2.14) becomes

$$\epsilon \left( \frac{\partial \rho_{oc}^*}{\partial t^*} \right) = \rho^* D_e^* \left\{ \frac{\partial}{r^* \partial r^*} \left( r^* \frac{\partial Y_c}{\partial r^*} \right) + \frac{\partial^2 Y_c}{\partial x^* 2} \right\} - W_c^* \quad (2.14a)$$

Boundary conditions

$$\text{at } r^* = r_d^* ; \quad h_d^* \rho^* (Y_c - Y_g) = \rho^* D_e^* \left( \frac{\partial Y_c}{\partial r^*} \right) \quad (2.15a)$$

$$\text{at } r^* = r_c^* ; \quad \frac{\partial Y_c}{\partial r^*} = 0 \quad (2.15b)$$

energy in catalytic layer

$$\rho_c^* C_c^* \left( \frac{\partial T_c^*}{\partial t^*} \right) = \lambda_c^* \left\{ \frac{\partial}{r^* \partial r^*} \left( r^* \frac{\partial T_c^*}{\partial r^*} \right) + \frac{\partial^2 T_c^*}{\partial x^* 2} \right\} + q^* w_c^* \quad (2.16)$$

Boundary conditions

$$\text{at } r^* = r_d^* ; \quad h_t^* (T_c^* - T_g^*) = \lambda_c^* \left( \frac{\partial T_c^*}{\partial r^*} \right) \quad (2.17a)$$

$$\text{at } r^* = r_c^* ; \quad \lambda_c^* \left( \frac{\partial T_c^*}{\partial r^*} \right) = \lambda_s^* \left( \frac{\partial T_s^*}{\partial r^*} \right) \quad (2.17b)$$

$$\text{reaction rate } w_c^* = \beta^* 1.772 (\rho_{oc}^* T_c^*)^{0.8} \exp\left(\frac{-E_c^*}{R^* T_c^*}\right) \quad (2.18)$$

where  $\beta^*$  is the catalyst loading. It describes the amount of catalysts deposited in the porous layer and the unit is  $[\text{kg-pt/m}^3]$

where it is based on the substrate volume. Equation (2.18) is derived in Appendix A.

energy in substrate layer

$$\rho_s^* C_s^* \left( \frac{\partial T_s^*}{\partial t^*} \right) = \lambda_s^* \left\{ \frac{\partial}{r^* \partial r^*} \left( r^* \frac{\partial T_s^*}{\partial r^*} \right) + \frac{\partial^2 T_s^*}{\partial x^*^2} \right\} \quad (2.19)$$

#### Boundary conditions

$$\text{at } r^* = r_c^* ; \quad \lambda_s^* \left( \frac{\partial T_s^*}{\partial r^*} \right) = \lambda_c^* \left( \frac{\partial T_c^*}{\partial r^*} \right) \quad (2.20a)$$

$$\text{at } r^* = r_s^* ; \quad \frac{\partial T_s^*}{\partial r^*} = 0 \quad (2.20b)$$

Before nondimensionalizing the solid equations, the following quantities are defined :

$$\alpha_c^* = \frac{\lambda_c^*}{\rho_c^* C_c^*} \quad \alpha_s^* = \frac{\lambda_s^*}{\rho_s^* C_s^*} \quad (2.21)$$

$$\tau_t^* = \frac{h_c^{*2}}{\alpha_c^*} \quad \tau_m^* = \frac{\epsilon h_c^{*2}}{D_e^*(0,0)}$$

$$Sh = \frac{h_d^*}{D_e^*/h_c^*} \quad B_c = \frac{h_t^*}{\lambda_c^*/h_c^*}$$

$$K_c^* = \left[ \beta^* \cdot 1.772 \cdot p^* \cdot Y_g(0,0) \cdot \frac{M_g^*}{M_o^*} \right]^{0.8} \exp(-E_c)$$

$$D_{at} = \frac{K_c^* h_c^{*2}}{\rho_c^* \alpha_c^*} \quad D'_{at} = D_{at} q_c$$

$$D_{am} = \frac{K_c^* h_c^{*2}}{\rho_s^* (0,0) D_e^*(0,0)} \quad D'_{am} = \frac{D_{am}}{Y_g(0,0)}$$

where  $\alpha_c^*$  and  $\alpha_s^*$  are the thermal diffusivity in the catalytic and substrate layer, respectively,  $\tau_t^*$  is the thermal diffusion time in the catalytic layer ( $h_c^*$  is the catalytic layer thickness),  $\tau_m^*$  is the mass diffusion time in the catalytic layer,  $S_h$  and  $B_c$  are the Sherwood and Biot number, respectively,  $K_c^*$  is a group number from the catalytic reaction rate,  $D_{am}$  and  $D_{at}$  are the Damköhler numbers which have the following physical meaning :

$$D_{am} \propto \frac{\text{catalytic reaction rate}}{O_2 \text{ mass diffusion rate in catalytic layer}} \quad (2.22a)$$

$$D_{at} \propto \frac{\text{catalytic reaction rate}}{\text{thermal diffusion rate in catalytic layer}} \quad (2.22b)$$

Several time ratios are also defined :

$$\delta_c = \frac{\tau_t^*}{\tau^*} \quad \delta_s = \frac{h_c^{*2}/\alpha_s^*}{\tau^*} \quad (2.23)$$

$$\delta_m = \frac{\tau_m^*}{\tau^*}$$

Introducing the nondimensional parameters :

$$r = \frac{r^*}{h_c^*} \quad x = \frac{x^*}{L^*} \quad t = \frac{t^*}{\tau^*} \quad (2.24)$$

$$Y_c = \frac{\rho_{oc}^*}{\rho^*} \quad E_c = \frac{E_c^*}{R^* T^*(0,0)} \quad q_c = \frac{q^*}{C_c^* T_g^*(0,0)}$$

$$y_c = \frac{Y_c}{Y_g(0,0)} \quad T_c = \frac{T_c^*}{T_g^*(0,0)} \quad \lambda = \frac{\lambda_s^*}{\lambda_c^*}$$

Eq. (2.14a) for O<sub>2</sub> becomes :

$$\delta_m \frac{1}{T_g} \frac{\partial y_c}{\partial t} = \frac{\partial}{r} \frac{\partial y_c}{\partial r} (r \frac{\partial y_c}{\partial r}) - D'_{am} y_c^{0.8} \exp \left[ E_c (1 - \frac{1}{T_c}) \right] \quad (2.25)$$

Boundary conditions

$$\text{at } r = r_d ; \quad \frac{\partial y_c}{\partial r} = Sh (y_c - y_g) \quad (2.26a)$$

$$\text{at } r = r_c ; \quad \frac{\partial y_c}{\partial r} = 0 \quad (2.26b)$$

energy in catalytic layer

$$\delta_c \frac{\partial T_c}{\partial t} = \frac{\partial}{r} \frac{\partial T_c}{\partial r} (r \frac{\partial T_c}{\partial r}) + D'_{at} y_c^{0.8} \exp \left[ E_c (1 - \frac{1}{T_c}) \right] \quad (2.27)$$

Boundary conditions

$$\text{at } r = r_d ; \quad \frac{\partial T_c}{\partial r} = B_c (T_c - T_g) \quad (2.28a)$$

$$\text{at } r = r_c ; \quad \frac{\partial T_c}{\partial r} = \lambda \frac{\partial T_s}{\partial r} \quad (2.28b)$$

energy in substrate layer

$$\delta_s (\frac{\partial T_s}{\partial t}) = \frac{\partial}{r} \frac{\partial T_s}{\partial r} (r \frac{\partial T_s}{\partial r}) \quad (2.29)$$

Boundary conditions

$$\text{at } r = r_c ; \quad \frac{\partial T_s}{\partial r} = \lambda \frac{\partial T_c}{\partial r} \quad (2.30a)$$

$$\text{at } r = r_s ; \quad \frac{\partial T_s}{\partial r} = 0. \quad (2.30b)$$

Initial conditions

catalytic layer

$$T_c(x, r, t=0) = 1 ; \quad y_c(x, r, t=0) = 0 \quad (2.31)$$

substrate layer

$$T_s(x, r, t=0) = 1 \quad (2.32)$$

In deducing the above system of equations, it is assumed that  $h_c^*/L^* \ll 1$ . Hence the diffusion and conduction in the  $x$ -direction are negligible compared with those in the  $r$ -direction. It is assumed that we have a cold start-up initial condition, i.e. the solid temperature is uniform and equals the inlet gas temperature at the initial moment ( $t=0$ ), and the catalytic layer has no absorbed oxygen.

### 2.3 Choice of Reference Time Scales

In the dimensionless equations, a number of time ratios appears but the characteristic time scale has yet to be specified. The choice of the proper reference time scale is clearly dictated by the physical processes we would like to investigate. In Table 1, various time scales are estimated. One sees that mass diffusion time in the catalytic layer is the shortest while the solid heat-up time is the longest. If we choose mass diffusion as the time scale to be resolved, then we clearly have accounted for all the transient events in the combustor (except for acoustic wave phenomena). Such a model will be referred to as the "full transient model". The full transient model is, in principle, the most accurate. But the calculation can become very time-consuming if it is carried out over a period of solid heat-up time. This is because the ratio of solid heat-up time to mass diffusion time is in general a very large number. So the full transient model is best reserved for instances where a fast transient events need to be resolved.

On the other hand, if we choose the longest solid heat-up time as the reference time scale, then Table 1 shows that all other processes can be regarded as quasi-steady. Although fast transient phenomena can not be captured, the model can describe the global heat-up/ignition process and is fast in computation. Such a model will be referred to as the "energy integral model". In the

following section, both the full transient and the energy-integral model will be derived or formulated.

#### 2.4 Full Transient Model

Substituting  $\tau^*$  by  $\tau_m^*$  into Eq. (2.23), we get

$$\delta_g = \frac{L^*/u^*(0,0)}{\tau_m^*} \quad \delta_m = 1 \quad (2.33)$$

$$\delta_c = \frac{\tau_t^*}{\tau_m^*} \quad \delta_s = \frac{h_c^{*2}/\alpha_s^*}{\tau_m^*}$$

and Eqs. (2.8, 2.9, 2.10, 2.11, 2.25, 2.27, 2.29) are reduced to

#### Gas-phase

$$\text{continuity} \quad \delta_g \frac{\partial \rho}{\partial t} + \frac{\partial (\rho u)}{\partial x} = 0 \quad (2.34)$$

$$\text{species} \quad \rho \delta_g \frac{\partial y_g}{\partial t} + \rho u \frac{\partial y_g}{\partial x} + J_D (y_g - y_{c,s}) \quad (2.35)$$

$$= B_1^* (\rho y_g)^b \exp\left(-\frac{E_g}{T_g}\right)$$

energy

$$\rho \delta_g \frac{\partial T_g}{\partial t} + \rho u \frac{\partial T_g}{\partial x} + J_H (T_g - T_{c,s}) = q_g B_2^* (\rho y_g)^b \exp\left(-\frac{E_g}{T_g}\right) \quad (2.36)$$

equation of state

$$P = \rho T_g \quad (2.37)$$

### Solid phase

species in catalytic layer

$$\frac{1}{T_g} \frac{\partial y_c}{\partial t} = r \frac{\partial}{\partial r} \left( r \frac{\partial y_c}{\partial r} \right) - D_{at}' y_c^{0.8} \exp\left[ E_c \left( 1 - \frac{1}{T_c} \right) \right] \quad (2.38)$$

energy in catalytic layer

$$\delta_c \frac{\partial T_c}{\partial t} = r \frac{\partial}{\partial r} \left( r \frac{\partial T_c}{\partial r} \right) + D_{at}' y_c^{0.8} \exp\left[ E_c \left( 1 - \frac{1}{T_c} \right) \right] \quad (2.39)$$

energy in substrate layer

$$\delta_s \left( \frac{\partial T_s}{\partial t} \right) = r \frac{\partial}{\partial r} \left( r \frac{\partial T_s}{\partial r} \right) \quad (2.40)$$

## 2.5 Energy Integral Model

Consider a control volume in the solid phase which includes the catalytic and substrate layer (see Fig. 1c). Three parts constitute the overall transient solid energy balance :

- (1) Time rate of change in internal energy in the control volume which includes the catalytic layer from  $r_d^*$  to  $r_c^*$  and the substrate layer from  $r_c^*$  to  $r_s^*$ .

$$\int_{r_d^*}^{r_s^*} 2 \rho^* C^* \pi r^* \frac{\partial T^*}{\partial t^*} dr^* dx^* \quad (2.41)$$

- (2) Time rate of energy transfer into the control volume from the gas phase

$$h_t^* 2 \pi r_d^* dx^* (T_g^* - T_{c,s}^*) \quad (2.42)$$

- (3) Energy generated in the control volume per unit time

$$\int_{r_d^*}^{r_s^*} W_c^* q^* 2 \pi r^* dr^* dx^* \quad (2.43)$$

Taking energy balance, i.e. (1) = (2) + (3), the result is:

$$\int_{r_d^*}^{r_s^*} \rho^* C^* \frac{\partial T^*}{\partial t^*} r^* dr^* = h_t^* r_d^* (T_g^* - T_{c,s}^*) + \int_{r_d^*}^{r_s^*} W_c^* q^* r^* dr^* \quad (2.44)$$

Eq. (2.44) can be used to define a solid heat-up time. By equating the unsteady term with the convection term, we get

$$\tau_{HT}^{*(1)} = \frac{2 \int_{r_d}^{r_s} \rho^* C^* r^* dr^*}{Nu_\infty^* \lambda_g^* (0,0)} \quad (2.45)$$

If we equate the unsteady term with the reaction term, we obtain

$$\tau_{HT}^{*(2)} = \frac{\int_{r_d}^{r_s} \rho^* C^* r^* dr^*}{h_c^{*2} K_c^* q^* / T^*(0,0)} \quad (2.46)$$

Since both heat transfer with gas and catalytic chemical reaction can contribute to the heat-up process, one way of defining the total heat-up time  $\tau_{HT}^*$  is

$$\frac{1}{\tau_{HT}^*} = \frac{1}{\tau_{HT}^{*(1)}} + \frac{1}{\tau_{HT}^{*(2)}} \quad (2.47)$$

However, this formulation does complicate the nondimensional equations. In the computations performed, we find that  $\tau_{HT}^{*(1)}$  is always smaller than  $\tau_{HT}^{*(2)}$ . Therefore, for simplicity,  $\tau_{HT}^*$  is taken to be  $\tau_{HT}^{*(1)}$  as given by Eq. (2.45). With this choice, the dimensionless form of Eq. (2.44) becomes :

$$\int_{r_d}^{r_s} \rho C \frac{\partial T}{\partial t} r dr = r_{nk} (T_g - T_{c,s}) \quad (2.48)$$

$$+ \frac{\lambda_c^* 2 D_{at}'}{\lambda_g^*(0,0) Nu_\infty} \int_{r_d}^{r_c} y_c^{0.8} \exp\left[ E_c (1 - \frac{1}{T_c}) \right] r dr$$

where

$$r_{nk} = \frac{Nu_x \lambda_g^*}{Nu_\infty \lambda_g^*(0,0)} \quad (2.49)$$

With  $\tau^* = \tau_{HT}^*$ , we also get

in gas phase  $\delta_g = \frac{\tau_r^*}{\tau_{HT}^*} \ll 1$

in catalytic layer  $\delta_c = \frac{\tau_t^*}{\tau_{HT}^*} \ll 1, \quad \delta_m = \frac{\tau_m^*}{\tau_{HT}^*} \ll 1$

in substrate layer  $\delta_s = \frac{h_c^{*2} / \alpha_s^*}{\tau_{HT}^*} \ll 1$

Neglecting these terms with small parameter  $\delta$ 's, the dimensionless equations all become quasi-steady and are presented as follows :

### Gas-phase

$$\text{continuity} \quad \rho u = \rho(0,0) u(0,0) \quad (2.50)$$

$$\text{species } \rho u \frac{\partial y_g}{\partial x} + J_D(y_g - y_{c,s}) = B_1^*(\rho y_g)^b \exp\left(\frac{-E_g}{T_g}\right) \quad (2.51)$$

$$\text{energy} \quad \rho u \frac{\partial T_g}{\partial x} + J_H (T_g - T_{c,s}) = q_g B_2^* (py_g)^b \exp\left(\frac{-E_g}{T_g}\right) \quad (2.52)$$

$$\text{equation of state} \quad P = \rho T_g \quad (2.53)$$

Boundary conditions are given at the inlet of the reactor

$$y_g(x=0) = 1 \quad ; \quad T_g(x=0) = 1 \quad (2.54)$$

$$\rho(x=0) = 1 \quad ; \quad u(x=0) = 1$$

### Solid-phase

### species in catalytic layer

$$\frac{\partial}{\partial r} \left( r \frac{\partial y_c}{\partial r} \right) - D'_{am} y_c^{0.8} \exp \left[ E_c \left( 1 - \frac{1}{T_c} \right) \right] = 0 \quad (2.55)$$

energy in catalytic layer

$$\frac{\partial}{r \partial r} (r \frac{\partial T_c}{\partial r}) + D'_{at} y_c^{0.8} \exp \left[ E_c \left( 1 - \frac{1}{T_c} \right) \right] = 0 \quad (2.56)$$

The similarity between the energy Eq.(2.55) and the species Eq.(2.56) suggests that a Damköhler analogy [22] can be used to eliminate one of two equations in the computation. A detailed derivation of the Damköhler analogy is carried out in Appendix B.

The analogy is given by :

$$T_c = T_{c,s} + \frac{D'_{at}}{D'_{am}} (y_{c,s} - y_c) \quad (2.57)$$

Substituting Eq. (2.57) into Eq. (2.55) for  $T_c$  gives a modified species equation as :

$$\frac{\partial}{r \partial r} (r \frac{\partial y_c}{\partial r}) = D'_{am} y_c^{0.8} \exp \left\{ E_c \left[ 1 - \frac{1}{T_{c,s} + \frac{D'_{at}}{D'_{am}} (y_{c,s} - y_c)} \right] \right\} \quad (2.58)$$

The energy equation for the substrate layer, Eq. (2.40), is reduced to

$$\frac{\partial}{r \partial r} (r \frac{\partial T_s}{\partial r}) = 0 \quad (2.59)$$

Integrating Eq. (2.59) twice, the result is :

$$T_s(r) = c \ln(r) + d \quad (2.60)$$

where  $c$  and  $d$  are constants and it subjects the following boundary conditions:

$$\text{at } r = r_c ; \quad T_s = T_c \quad (2.61a)$$

$$\lambda \frac{\partial T_s}{\partial r} = \frac{\partial T_c}{\partial r} \quad (2.61b)$$

$$\text{at } r = r_s ; \quad \frac{\partial T_s}{\partial r} = 0 \quad (2.61c)$$

Applying Eqs. (2.61a) and (2.61c) gives

$$T_s(r) = T_c(r_c) \quad (2.62)$$

that is, the substrate temperature is uniform in  $r$ -direction. Notice that it can be a function of time during transient heat-up .

The energy-integral model represents an extension of the transient model in [5] where the catalytic layer is a surface (no structure). In the present transient model, finite catalytic layer thickness is included; temperature and species non-uniformity are allowed.

## CHAPTER III

### NUMERICAL SCHEME

#### 3.1 Full Transient Model Treatment

For the gas-phase part which includes four Eqs.— (2.34) to (2.37)— and four unknowns—  $y_g$ ,  $T_g$ ,  $u$ , and  $\rho$ — the Euler explicit method with an upwind space difference is applied on the species equation and the energy equation for  $y_g$  and  $T_g$ ; the Euler backward implicit method is applied to solve the continuity equation for  $u$ . Finally,  $\rho$  is solved from the equation of state. Finite difference representations for the gas-phase equations are listed in the following: (superscript  $n+1$  denotes quantity at new time level, and without  $n+1$  denotes quantity at old time level  $n$  )

#### Gas phase

##### species

$$y_{gi}^{n+1} = \left( \frac{\Delta t}{\Delta x} \right) \frac{u}{\delta_g} (y_{gi-1} - y_{gi}) + \frac{\Delta t}{\delta_g} \frac{J_{Di}}{\rho_i} (y_{c,si} - y_{gi}) + \frac{\Delta t}{\delta_g} B_i^* \rho_i^{b-1} y_{gi}^b \exp \left( \frac{-E}{T_i} \right) + y_{gi}$$
 (3.1)

energy

$$T_{g,i}^{n+1} = \left( \frac{\Delta t}{\Delta x} \right) \frac{u}{\delta_g} (T_{g,i-1} - T_{g,i}) + \frac{\Delta t}{\delta_g} \frac{J_{H,i}}{\rho_i} (T_{c,s,i} - T_{g,i}) + q_g \frac{\Delta t}{\delta_g} B_2^* \rho_i^{b-1} y_{g,i}^b \exp \left( -\frac{E}{T_i} \right) + T_{g,i} \quad (3.2)$$

continuity

$$u_i^{n+1} = \frac{\left( \delta_g (\rho_i - \rho_i^{n+1}) + \left( \frac{\Delta t}{\Delta x} \right) \rho_i^{n+1} u_{i-1}^{n+1} \right)}{(2\rho_i^{n+1} - \rho_{i-1}^{n+1}) \left( \frac{\Delta t}{\Delta x} \right)} \quad (3.3)$$

equation of state

$$\rho_i^{n+1} = \frac{P}{T_i^{n+1}} \quad (3.4)$$

Considering the Von Neuman stability analysis for the Euler explicit method, this method is stable when the following condition is satisfied :

$$0 \leq \left( \frac{\Delta t}{\Delta x} \right) \left( \frac{\tau_m^*}{\tau_r^*} \right) \leq 1 \quad (3.5)$$

Solid phase

For the solid phase part, Eqs.(2.38) to (2.40) are solved by the implicit Crank-Nicolson method [23] which is an unconditional stable scheme with accuracy of  $O[(\Delta t)^2, (\Delta x)^2]$ . A quasi-linearization technique (also called Newton linearization) [24] is implemented on the nonlinear heterogeneous chemical reaction rate to avoid numerical stability difficulties [25]. The resulting tridiagonal systems of linear algebraic equations which are diagonally dominant are usually solved by the LU-decompositions method [26]. The finite difference equations are derived in Appendix C and the following equations are obtained (where bracket denotes a matrix).

species in catalytic layer

$$\begin{bmatrix} A_1 \end{bmatrix} \begin{bmatrix} y_c^{n+1} \end{bmatrix} = \begin{bmatrix} D_1 \end{bmatrix} \quad (3.6)$$

energy in catalytic layer

$$\begin{bmatrix} A_2 \end{bmatrix} \begin{bmatrix} T_c^{n+1} \end{bmatrix} = \begin{bmatrix} D_2 \end{bmatrix} \quad (3.7)$$

energy in substrate layer

$$\begin{bmatrix} A_3 \\ T_s^{n+1} \end{bmatrix} = \begin{bmatrix} D_3 \end{bmatrix} \quad (3.8)$$

The order of computational execution for a monolithic reactor under cold start-up operation using the full transient model is

- (1) Specify the initial values of  $T_g(x)$ ,  $y_g(x=0)$ ,  $\rho(x)$ ,  $u(x)$  in the gas phase, and  $T_c(x, r)$ ,  $y_c(x, r)$ ,  $T_s(x, r)$  in the solid phase.
- (2) Solve the gas-phase equations (3.1) through (3.4) to obtain  $T_g(x)$ ,  $y_g(x)$ ,  $\rho(x)$ , and  $u(x)$  at axial location  $\Delta x$  and new time level  $n+1$ .
- (3) Substitute the updated gas-phase properties from step (2) for matrix coefficients  $A_1$ ,  $A_2$ ,  $A_3$ ,  $D_1$ ,  $D_2$ ,  $D_3$ . Due to the application of quasi-linearization on the reaction rate, iterations are required in Eqs. (3.6) (3.7) (3.8) by using a simple iterative updating procedure. To do this, the profiles  $y_c(r)$ ,  $T_c(r)$ ,  $T_s(r)$  used to start iterations are those of the previous time step, and the system solved for new  $y_c(r)$ ,  $T_c(r)$ ,  $T_s(r)$  at the new time level  $\Delta t$ . This procedure can be repeated iteratively until a convergence criterion is reached. (Agreement of successive iterations within a tolerance of 0.1 % of the dimensionless temperature is used in this study.)
- (4) Through steps (1), (2), (3), the full transient model proceeds to the next axial location  $2\Delta x$  at the new time level  $\Delta t$ . In

summary, computations are carried out by sweeping the x-axis from the inlet of reactor to the exit at every  $\Delta t$ , then advancing to next time step.

Gas-phase equations (3.1) to (3.4) and solid-phase equations (3.6) to (3.8) are coupled, and they must be solved simultaneously. This complicates the problem considerably. However, the gas-phase properties are not sensitive to the variation in the solid phase, and a also small time step is used in computation. Therefore, the values of  $T_{c,s}^{n+1}$  and  $y_{c,s}^{n+1}$  in the gas-phase equations are approximated by  $T_{c,s}^n$  and  $y_{c,s}^n$ , respectively. The finite differences are evaluated on uniform grids in axial x direction and non-uniform grid in radial r direction. In x direction, it is divided by 31 points and gives  $\Delta x = 0.033$ . Because reaction occurs in the catalytic layer only, steep temperature and species gradient may exist in this layer but not in the substrate layer. Therefore, a smaller radial space step is used in the catalytic layer ( $\Delta r=0.05$ ) and a larger grid step is used in the substrate layer. In the sample calculations to be presented, the catalytic layer is one third of the total solid thickness and the substrate is the other two third. Twenty one grid points are utilized in each of these layers. The time step  $\Delta t=0.1$  is used in most cases. However, varied time steps are used for cases in which the gas ignition is strong. A smaller time step,  $\Delta t=0.01$ , is used during the gas ignition period.

### 3.2 Energy Integral Model Treatment

Rewrite the governing equations of the energy-integral model derived in chapter II.

#### Gas phase

continuity  $\rho u = \rho (0,0) u (0,0)$  (3.9)

#### species

$$\rho u \frac{\partial y_g}{\partial x} + J_D (y_g - y_{c,s}) = B_1^* (\rho y_g)^b \exp(-E_g/T_g) \quad (3.10)$$

#### energy

$$\rho u \frac{\partial T_g}{\partial x} + J_H (T_g - T_{c,s}) = q_g B_2^* (\rho y_g)^b \exp(-E_g/T_g) \quad (3.11)$$

equation of state  $P = \rho T_g$  (3.12)

#### Boundary conditions

$$T_g(x=0) = 1 \quad ; \quad y_g(x=0) = 1 \quad (3.13)$$

$$\rho(x=0) = 1 \quad ; \quad u(x=0) = 1$$

Solid phase

The overall transient solid energy equation (2.48) is written in finite difference form :

$$\int_{r_d}^{r_s} \rho C T(t+\Delta t, r) r dr = \int_{r_d}^{r_s} \rho C T(t, r) r dr + \Delta t \left\{ r_{nk} (T_g - T_{c,s}) + \frac{\lambda_c^* 2 D'_{at}}{\lambda_g^*(0,0) N u_\infty} \int_{r_d}^{r_c} y_c^{0.8} \exp \left[ E_c \left( 1 - \frac{1}{T_c} \right) \right] r dr \right\} \quad (3.14)$$

The left hand side of the above equation represents the thermal energy in the solid (catalytic layer plus substrate layer) at time  $t+\Delta t$ .

## species in catalytic layer

$$\frac{\partial}{r \partial r} (r \frac{\partial y_c}{\partial r}) = D'_{am} y_c^{0.8} \exp \left\{ E_c \left[ 1 - \frac{1}{T_{c,s} + \frac{D'_{at}}{D'_{am}} (y_{c,s} - y_c)} \right] \right\} \quad (3.15)$$

Boundary conditions

$$\text{at } r = r_d ; \quad \frac{\partial y_c}{\partial r} = S_h (y_c - y_g) \quad (3.16a)$$

$$\text{at } r = r_c ; \quad \frac{\partial y_c}{\partial r} = 0 \quad (3.16b)$$

Temperature profile in catalytic layer

$$T_c = T_{c,s} + \frac{D'_{at}}{D_{am}} (y_{c,s} - y_c) \quad (3.17)$$

Temperature profile in substrate layer

$$T_s(r) = T_c(r_c) \quad (3.18)$$

The overall transient solid energy equation (3.14) needs initial profiles for temperature  $T_c(r)$ ,  $T_s(r)$ , and species  $y_c(r)$  at every  $\Delta x$  location along the channel. These profiles can be obtained from the full transient model results, assuming computation is switched from the full transient model to the energy-integral model at time  $t_0$ .

#### Initial conditions

catalytic layer

$$T_c(x, r, t_0) = \text{specified} \quad (3.19a)$$

$$y_c(x, r, t_0) = \text{specified} \quad (3.19b)$$

substrate layer

$$T_s(x, r, t_0) = T_c(x, r_c, t_0) \quad (3.20)$$

The computational procedures are listed as follows :

- (a) The overall transient solid energy equation (3.14) is integrated for one time step ( $\Delta t$ ) at each  $x$  to find the new thermal energy integral  $\int_{r_d}^{r_s} \rho C T(t+\Delta t, r) r dr$  at that  $x$  location.

The values at present time  $t$  are used in the right hand side of Eq. (3.14) in this calculation.

- (b) To find the temperature profile which satisfies the energy integral at  $t+\Delta t$ , Eq. (3.15) and (3.17) are solved iteratively. The iterative procedure is as follows. First, estimating the boundary value  $T_{c,s}$  and Eq. (3.15) is solved by shooting technique [27] for  $y_c(r)$  subject to boundary conditions (3.16a, b). Once  $y_c(r)$  is obtained, it is substituted into Eq. (3.17) for  $T_c(r)$ . The temperature profile is then used to evaluate the energy integral. If the value of the integral is not equal to that obtained in (a), a new  $T_{c,s}$  is estimated. This procedure is repeated until convergence is obtained. The solid  $T_s$  and  $y_c$  which satisfy the energy integral is the solid temperature and oxygen mass fraction at  $t+\Delta t$ . The process is repeated for all the grid points in the  $x$ -direction.
- (c) With the surface temperature and oxygen mass fraction obtained, the gas-phase properties are to be updated to  $t+\Delta t$ . This process involved the solutions of quasi-steady equations (3.9) to (3.12). Since these equations are first order in  $x$ , the

Runge-Kutta method is used to integrate them from the channel entrance ( $x=0$ ) to the exit ( $x=1$ ).

- (d) The whole cycle is then repeated for the next time step.

The shooting method reduces the solution of a boundary value problem to the iterative solution of an initial value problem. The usual approaches involve a trial-error procedure. In order to have a good initial guess, the first guessed  $y_{c,s}$  and  $T_{c,s}$  is selected from the previous time step. The advantages of using this model are that

- (1) The Damköhler analogy eliminates the computation of the catalytic energy equation.
- (2) Assumption of " thermally-thin layer " eliminates the computation of the substrate energy equation.
- (3) Quasi-steady assumption also eliminates the computation of the continuity equation.
- (4) A large time step is allowed in computation.

## CHAPTER IV

### RESULTS AND DISCUSSIONS

#### 4.1 Introduction

There are a large number of nondimensional parameters in the equations and in the boundary conditions derived in Chapter II. Associated with these nondimensional parameters are many time scales as shown in Table 2. Clearly the catalytic ignition problem can have a variety of complex behaviors depending on the choice of the values of these parameters. Instead of investigating the influence of all these parameters, in this study, we will limit our computational effort to fulfilling two basic objectives.

The first objective is to understand the reactive structure variation with time in the catalytic layer during the ignition transient, since the new element of our model is the inclusion of catalytic layer in-depth reaction. The second objective is to test the energy-integral model as an efficient way to compute the heat-up transient of the igniter.

To fulfill these two objectives, we need to be able to perform computation through the whole ignition transient using both the full transient model and the energy-integral model. Because of the smallness of the time step needed in the full transient method, the parameters of the test cases are deliberately chosen in such a way

that a reasonable computing resource is adequate. This means that the heat-up time of the solid is purposefully chosen to be small (as compared with values listed in Table 1). Nevertheless, the order between the various time scales is still preserved.

#### 4.2 General Transient Behavior

A representative case (referred to as Case 1) that illustrates the combustion processes from reactor start-up through transient to steady states are presented here. The values of properties for Case 1 are listed in Table 4 and the values of operating parameters are listed in Table 5.

Figure 2 shows the axial profiles in the gas channel for gas temperature ( $T_g$ ), gas-phase oxygen fraction ( $y_g$ ), gas-phase reaction rate ( $W_g^*$ ), surface temperature ( $T_{c,s}$ ), surface oxygen fraction ( $y_{c,s}$ ) and maximum catalytic reaction rate ( $W_c^*$ ) at times 10, 50, 100  $\tau_m^*$  (where  $\tau_{HT}^* = 500 \tau_m^*$ ). At  $t^* = 0$  the temperatures of the gas and the solid are uniform and equal to the inlet temperature ( $400^\circ\text{K}$ ). The gas channel has been filled up with hydrogen and oxygen is introduced at the inlet. At very early times ( $t^* = 10\tau_m^* = 0.13\tau_r^*$ ), the oxygen front has not been convected through the entire reactor and the oxygen concentration drops to zero abruptly at  $x=0.3$  in the gas channel which can be seen in Fig. 2b. When the oxygen is flowing downstream, it is also absorbed by the catalytic layer. Oxygen is also consumed by the catalytic reaction which is represented by the

increased catalytic reaction rate in Fig. 2f. The gas temperature (Fig. 2a) is still at the level of the inlet temperature, but the solid temperature has a slight rise at the inlet (Fig. 2d) due to the catalytic reaction occurring there (Fig. 2f). Figure 3 shows the contour plot for  $T_c(x,r)$ ,  $T_s(x,r)$ ,  $y_c(x,r)$  and  $W_c(x,r)$  at time  $t^* = 10 \tau_m^*$ . Oxygen is absorbed uniformly in the radial direction and gradually propagates in the axial direction (Fig. 3b). Similar profiles in the solid reaction rate can be seen in Fig. 3c. Therefore, the non-uniformities such as species and reaction rate in the solid are primarily in the axial direction only.

At slightly longer time ( $t^* = 50 \tau_m^*$ ), the oxygen front just passes through the exit of reactor (Fig. 2b). The oxygen in the solid extends further in the axial direction, and non-uniform profiles appear near the inlet section (Fig. 4b). A concentrated hot spot can be seen in Fig. 4a in accordance with the local high reaction rate shown in Fig. 4c. As time increases ( $t^* = 100 \tau_m^*$ , Fig. 2d), the solid temperature rises rapidly from a lower inlet temperature to a peak which is located slightly behind the entrance, then decreases monotonically until the exit of reactor. By contrast, the gas phase receives heat from the solid, and the gas temperature rises slowly and uniformly ( $t^* = 100 \tau_m^*$ , Fig. 2a) because of receiving heat from the solid phase and the convection effect.

Because there is more oxygen in the gas phase near the tube entrance and also a larger heat and mass transfer coefficient, the

oxygen concentrations are higher near the entrance (Fig. 3b). It may be noticed that the solid temperature is non-uniform in the r-direction in the catalytic layer but is uniform in the substrate layer (e.g. Fig. 4b). The computed uniform substrate temperature from the full transient model is consistent with Eq. (2.59) because at  $t^* = 100 \tau_m^*$ , it is much greater than the thermal diffusion time of the substrate, and the substrate behaves as thermally thin. The reason that there is a temperature gradient in the catalytic layer is because of the existence of reaction.

As time increases, from one to two heat-up time ( $\tau_{HT}^*$ ), the peaks in  $T_g$  (Fig. 6a) and  $T_{c,s}$  (Fig. 6d) grow larger. At time 2  $\tau_{HT}^*$ , the gas-phase reaction becomes active near the exit of the reactor (Fig. 6c). As may be seen from Fig. 7 and 8, the catalytic reaction rate reaches the maximum value at time 2  $\tau_{HT}^*$  while the onset of gas-phase reaction occurs. It implies that the gas phase becomes active when the solid phase has reached maximum catalytic reaction rate. The oxygen has been consumed in most of the solid part except at the inlet region and near the surface in the downstream region (Fig. 7b and 8b). Likewise, the active solid region is shrinking to the inlet and the surface (Fig. 7c and 8c). The in-depth reaction zone in the inlet indicates that the reaction is kinetically controlled and the surface-confined reaction zone in the downstream indicates that reaction is diffusionally controlled.

At steady state ( $t^* = 3 \tau_{HT}^*$ ), both the gas and the solid

temperatures reach the adiabatic flame temperature  $1360^{\circ}\text{k}$  (Fig. 6a and 6d). The abrupt rise in  $T_g$  and  $W_g^*$  (Fig. 7c) is due to the gas ignition. Once the gas is ignited, the gas temperature starts to exceed the solid temperature, and the heating of the solid is via energy transfer from the gas. This results in a slight temperature rise on the solid surface (Fig. 9a). Beyond the gas-phase ignition point (about two thirds of the bed length), the oxygen concentration drops to zero abruptly everywhere: the gas phase (Fig. 6b), the solid surface (Fig. 6e) and the in-depth layer (Fig. 9b). Therefore, the active catalytic reaction regions at steady state are further reduced to about two thirds of the total solid volume. The attainment of complete oxygen conversion in a short distance depends on the presence of homogeneous reaction in the gas channel; this special feature of catalytic combustor [28] also has been observed in experiments (in contrast to catalytic converter with only heterogeneous reaction).

#### 4.3 The Effect of Catalyst Loading

Catalyst loading is defined as the weight of catalyst applied to the solid [29]. It is usually expressed either as a percent of total substrate weight or as weight per unit substrate volume. The influences of catalyst loading are twofold. First a larger catalyst loading leads to the faster heterogeneous reaction, and consequently the solid phase will generate more non-uniformities during the

transient period. Second, the catalytic ignition point moves toward the inlet as the catalyst loading increases. A reasonable catalyst loading of  $1.8 \text{ kg/m}^3$  [30] has been selected in Case 1, and the computed results are shown in Fig. 2 to 9. In order to investigate the effect of catalyst loading, two catalyst loading values are assigned in Case 2 and Case 3 for  $0.18$  and  $18 \text{ kg/m}^3$ , respectively, while the other parameters are the same as Case 1 (the catalyst loading  $\beta^*$  appears in Eq. (2.18)). Due to the lower catalyst loading in Case 2, the longer reactor length (20 cm) is needed to achieve both the catalytic ignition and the gas ignition in comparison with the shorter length used in Case 1 (5 cm).

In Case 2, the transient responses in the reactor are very slow compared with Case 1, as shown in Fig. 10 at three time levels  $5$ ,  $7$ ,  $15 \tau_{HT}^*$ . The influences of reduced catalyst loading are obvious. Since the initiation of catalytic reaction is delayed, the whole combustion process in the reactor takes more time ( $15 \tau_{HT}^*$ ) to reach steady state and a longer length (20 cm) to complete reactions.

At  $t = 5 \tau_{HT}^*$ , the solid and the gas temperatures are almost identical (Fig. 10a and 10d). Figure 10f and 11c show that the maximum catalytic reaction occurs at the exit but not at the inlet as in Case 1. The in-depth solid temperature (Fig. 11a) and species (Fig. 11b) are uniform in the radial direction but not in the axial direction.

As time increases to  $7 \tau_{HT}^*$ , the gas and the solid temperatures

are rising at the same speed (Fig. 10a and 10d). Catalytic reaction rate increases and the peak region moves upstream as shown in Fig. 10f. The solid temperature is rising in the aft bed (Fig. 12a) and the solid species is decreasing similarly (Fig. 12b).

At steady state ( $t^* = 15 \tau_{HT}^*$ ), the gas-phase reaction is triggered, which can be seen by a sudden rise in the gas temperature (Fig. 10a) and the gas reaction rate (Fig. 10c). Because of low reactivity, the oxygen penetrates all the way into the catalytic layer and there is little radial-direction gradient as shown in Fig. 13b. The maximum catalytic reaction rate exists in the middle of reactor (Fig. 13c) and the gas-phase ignition point is located right after it. It implies that the solid phase and the gas phase response at the same speed.

Case 3 has a higher catalyst loading which is ten times higher than Case 1 and one hundred times higher than Case 2 (see Table 3). The increase in the catalyst loading causes the catalytic ignition to occur at the inlet (Fig. 14f) and also moves the gas-phase ignition point toward the inlet (Fig. 14c). Initially, there are strong radial gradients in the solid phase for  $T_c$ ,  $y_c$ , and  $W_c^*$  (Fig. 15) due to a sudden catalytic ignition occurring at the front while the rest of the solid phase is not active yet. In addition, the catalytic reaction is so strong that oxygen is consumed near the solid surface and does not have a chance to diffuse into the solid (Fig. 15b).

As time increases ( $t^* = 1 \tau_{HT}^*$ ), the peak in  $T_{c,s}$  moves slightly backward from the inlet (Fig. 14d), although the highest catalytic reaction rate is still at the inlet, and the active solid region is enlarged toward downstream (Fig. 14f). The solid temperature has less gradient in the radial direction (Fig. 16a) because most oxygen has been consumed by the surface layer (Fig. 16b). The maximum value of heterogeneous reaction rate is located at the inlet and is stabilized (Fig. 16c).

At steady state ( $t^* = 3 \tau_{HT}^*$ ), the gas ignition occurs in the middle of the reactor (Fig. 14c), and the whole solid reaches the adiabatic flame temperature except in a very small inlet region where it has a slightly lower temperature (Fig. 14d). Oxygen in the gas phase is consumed quickly downstream of the gas-phase ignition point (Fig. 14b). Therefore, in the downstream region there is little reaction (Fig. 17c). The gas and the solid temperatures become equilibrated in this zone.

Figure 18 gives the ignition boundary map as a function of reactor length and catalyst loading. Figure 18 shows that there are three different regions for ignition of monolithic catalytic combustor : a region with small reactor length and catalyst loading where no ignition occurs; a region with sufficiently large reactor length and loading factor where both catalytic and gas ignitions occur; and a region in-between where catalytic ignition occurs but not gas-phase ignition. Figure 18 shows that catalytic

ignition has to occur first before gas-phase ignition. It shows that at high loading, the catalytic ignition occurs at the tube inlet and the gas-phase ignition length becomes constant. But at low loading, the ignition length increases steeply with decreasing loading. For practical device (where there is a length limit), there will be a minimum catalyst loading below which the igniter does not function. Notice that Fig. 18 is plotted with a fixed incoming velocity and mixture ratio. In addition to its influence in the ignition boundary which is deduced from steady-state results, catalyst loading affects the transient response of the igniter.

In summary, as the catalyst loading increases, the non-uniformities in the reactor, which include the gas phase and the solid phase, are diminishing at steady state. Concerning the time to reach steady state, if the catalyst loading is significantly reduced such as in Case 2, then it takes longer time. However, when the catalyst loading is increased, such as in Case 3 ( $\beta^* = 18 \text{ kg/m}^3$ ), it still takes  $3 \tau_{HT}^*$ , as in case 1 ( $\beta^* = 1.8 \text{ kg/m}^3$ ). This happens because the higher catalyst loading only strengthens a local heterogeneous reaction but the major parts of the solid are not affected. Therefore, the whole solid still takes the same time to reach steady state as a low catalyst loading case.

#### 4.4 The Effect of Mixture Fuel/Oxidizer Equivalence Ratio

The inlet equivalence ratio is a measure of the oxygen concentration in the mixture. In a fuel-rich mixture, when  $\phi$  is reduced toward unity (stoichiometric ratio), the heat of reaction per mole of mixture increases. This raises the adiabatic flame temperature which affects reactions in both the gas phase and the solid phase.

Case 4 is given a higher oxygen concentration ( $\phi=4$ ) than Case 1 ( $\phi=8$ ) and is used to investigate the effect of equivalence ratio. At time  $t^*=0.2 \tau_{HT}^*$  ( $=100 \tau_m^*$ ), the solid has a slight temperature rise at the inlet (Fig. 19d), but the species on the solid surface are dropped suddenly (Fig. 19e) due to the strong heterogeneous reaction which can be seen in Fig. 19f. More detailed in-depth solid behavior can be obtained from the solid contour plot in Fig. 20. The highest solid temperature is located at the inlet (Fig. 20a) which is in accordance with the highest heterogeneous reaction rate shown in Fig. 20c. The in-depth species increases from the inlet to the exit (Fig. 20b).

As time increases to  $t^*=1\tau_{HT}^*$ , the solid ignites near the inlet ( $1\tau_{HT}^*$ , Fig. 19d), the gas phase is triggered after the solid ignition position and a strong gas temperature rise can be seen in Fig. 19a. Two peaks appear in the solid surface temperature profile : the first peak is due to the catalytic ignition and the second one is due to the gas-phase ignition. After the gas phase is ignited,

the gas temperature exceeds the solid temperature after the gas ignition point. Therefore, a slight temperature jump appears in the solid surface temperature profile due to the heat transfer from the gas phase to the solid. However, before the gas ignition point, the heating process is reversed. Also these two hot spots on the solid surface can be seen clearly in Fig. 21a. As the gas ignition is achieved, the oxygen is consumed almost completely after the ignition point (Fig. 19b and 19e), and the heterogeneous reaction in the catalytic layer also ceases at the same location (Fig. 21c).

By comparing the transient profiles in Case 1 and 3, we find that the effects of a more stoichiometric mixture are : (a) temperatures in the gas phase and the solid phase are higher; (b) less reactor length is needed to achieve the gas ignition; (c) there is less oxygen penetration into the catalytic layer; (d) less time is needed to reach steady state (Case 4,  $2 \tau_{HT}^*$  and Case 1,  $3 \tau_{HT}^*$ ). All those are due to the enhanced homogeneous and the heterogeneous reactions at higher flame temperature.

#### 4.5 The Cause of Non-uniformity in the Solid

In the model development, it has been assumed that the gas phase is one-dimensional and the solid is two-dimensional. In the above computations, we have discussed the cause of non-uniformities in the axial direction of the reactor. In this section, we discuss the non-uniformities in the radial direction of the solid.

Notice that associated with the solid energy equation and the species equation in the catalytic layer are the two Damköhler numbers  $Dat$  and  $Dam$ , and the other parameters such as  $q$ ,  $Y_g(0,0)$ ,  $S_h$  and  $B_c$ . First, concerning the species equation of the catalytic layer Eq.(2.22), the value of  $Dam$  is an important controlling factor which is the ratio between the mass diffusion time and the heterogeneous reaction time. Hence, when the mass diffusion time is slower than that of the mass consumption, a species gradient will exist in the radial direction. Similarly, in the energy equation of the catalytic layer, Eq.(2.25), the value of  $Dat$ , which is the ratio between the heat conduction time to the heterogeneous reaction time, controls the temperature gradients in the solid. When the heat conduction rate is slower than the heat release rate, temperature gradients will exist. In addition to conduction-reaction balance, the unsteady term is also a source for radial gradient.

Case 3 is an example of increasing the catalytic reaction rate by increasing the catalyst loading ten times from Case 1. At early time ( $0.2 \tau_{HT}^*$ ), a sequence of in-depth solid temperature profiles from the inlet ( $x=0$ ) to the middle of bed ( $x=0.5$ ) is shown in Fig. 23. The most non-uniform temperature profile exists at the inlet, and the peak is located in the middle of catalytic layer ( $r=0.3$ ). Further downstream ( $x=0.005, 0.01, 0.5$ ), the radial temperature profiles become more monotonic, decreasing from the surface toward the interior. Figure 24 shows the oxygen species

profiles, all monotonically decreasing from the surface as expected. The steeper gradient exists at the inlet. As time increases ( $1 \tau_{HT}^*$ , Fig. 25), the hump-type temperature profile at the inlet disappears; a monotonically profile increasing from the surface toward the interior is evolved. These monotonic profiles indicate the approach toward a quasi-steady distribution. When the steady state is reached at  $3 \tau_{HT}^*$  (Fig. 27), all temperature profiles are monotonic. Except at the inlet, the temperature distributions are almost uniform. The fact that the lowest temperature occurs on the surface of inlet is due to the higher heat transfer from the solid to the gas at that position.

Another example is given by Case 4 in which the amount of oxygen concentration in the approaching mixture is double that in Case 1. Consequently, the value of  $D_{at}$  increases due to the increase of heat of reaction  $q_c$ , and  $D_{am}$  decreases because of decreasing of  $Y_g(0,0)$ . This trend implies that the energy will be generated faster than the consumption of the species. In addition, the value of mass transfer coefficient  $S_h$  increases at the inlet region. Therefore, the species can diffuse into the solid more efficiently through the effect of increased Sherwood number.

At small time ( $t^* = 0.2\tau_{HT}^*$ ), a sequence of in-depth solid temperature profiles from the inlet ( $x=0$ ) to the middle of bed ( $x=0.5$ ) is shown in Fig. 29. At the inlet, the temperature profile is the opposite of the other locations ( $x=0.06, 0.12, 0.5$ ). This

profile is due to the inlet has reached quasi-steady state. Oxygen is monotonically decreasing from the surface to the interior of the solid (Fig. 30).

At larger time ( $t^* = 1\tau_{HT}^*$ ), the solid temperature is rising and the gradients in the radial direction are decreasing (Fig. 31). The inlet is the coolest part, and the rest of the solid has higher but uniform temperature. The temperature profiles reflect on the species profiles in Fig. 32, which shows a steep gradient at inlet and becomes small afterwards because of strong consumption.

At steady state ( $t^* = 2\tau_{HT}^*$ ), the temperature profiles are similar as early time ( $t^* = 1\tau_{HT}^*$ ) but the temperature magnitudes are increased (Fig. 33). The species profiles are also similar as before and the magnitudes are decreased (Fig. 34).

#### 4.6 Computed Results Using Energy-Integral Model

Although the full transient model is theoretically more accurate, it can be computationally costly. When the short transient period can be ignored, the energy-integral method can offer an attractive alternative. There are two ways to apply the energy-integral model. One is to apply it right from the beginning of the transient, and the other is to first start with the full transient calculation and switch it to the energy-integral at a specified time.

In this section, the computed results using the integral model

will be presented and compared with the results using the full-transient model. The purpose is to access the accuracy of the energy-integral model. In the first comparison, parameters of the Case 1 are computed using the energy-integral model initially. Figure 35 shows comparisons of the gas temperature at three time levels — 1, 2, and  $3 \tau_{HT}^*$ . At early time  $1 \tau_{HT}^*$ , the energy-integral model predicts lower gas temperature than the full transient model. However, at later times (e.g.  $2, 3 \tau_{HT}^*$ ), results from the two models compare favorably. Comparisons for the gas species are shown in Fig. 36. It indicates that the gas species is slightly over-predicted by the energy-integral model at  $1 \tau_{HT}^*$ , but predictions from two models fall on one line afterwards. Hence, the predictions on the gas species profiles are reversed from the gas temperature. Figure 37 shows the comparisons of the gas reaction rates. Since the gas reaction becomes important after  $1 \tau_{HT}^*$ , and at that time two models predict almost identical gas temperature and gas species, the comparisons of gas reaction rate have shown good agreement.

To compare the detailed predictions in the solid phase, it is better to look simultaneously at the two dimensional contour plot in the solid and the in-depth plot for the radial profile. By comparing the solid contours in Fig. 7a with that in Fig. 38a at  $1 \tau_{HT}^*$ , we notice that although the oxygen and the reaction rate plots compare favorably, the temperature profiles predicted by two models

are somewhat different. Figure 39 for the in-depth solid temperature shows that the deviation is the smallest at the inlet ( $x=0$ ) and increases afterwards. At the middle of bed ( $x=0.5$ ), the slopes predicted by two models are different. This is because the aft bed reaches quasi-steady state later than the front part. (The energy-integral model implies a quasi-steady temperature distribution as shown by Eq. (2.57).) Thus, applying the energy-integral model too early makes deviations at the aft bed section. Comparisons of the gas species profiles (Fig. 40) also show more deviation downstream, but the monotonic trend of  $y_c$  is the same.

As time increases ( $t^*=2 \tau_{HT}^*$ ), the catalytic reaction in the solid phase has reached maximum value. Therefore, the deviations from the two models' predictions in  $T$ ,  $y_c$ ,  $W_c$  become smaller. The contour plots are compared by Fig. 8 and 41. For the solid temperature, both models predict a hot spot at inlet region; and the temperature distributions are very close. In addition, the in-depth temperature profiles compared in Fig. 42 show good agreement from the inlet to the middle of bed. Comparisons in the species are shown in Fig. 43; the two models predict identical profiles. These good agreements continue to exist up to the steady state as shown in Fig. 44 and 9.

In summary, although the energy-integral model is applied at the beginning, the comparisons such as  $T$ ,  $y_c$ , and  $W_c^*$  have shown

great compatibility by using the simpler energy-integral model. The maximum deviation between two models predictions is the solid surface temperature at  $1 \tau_{HT}^*$  — the value is 10 %. The maximum deviation in the gas temperature is 3 %. The saving in computational time has been achieved by using the energy-integral model in Case 1. Using Sun Spark Work station, Case 1 takes 52 minutes to reach steady state at  $3 \tau_{HT}^*$  in comparison to 30 minutes by the energy-integral model. If the heat-up time  $\tau_{HT}^*$  is increased 100-fold, which is a more realistic value, the computational time using the energy-integral model should remain unchanged, but the computational time using the full transient model would be 5200 minutes.

In the next example, Case 3 is chosen to compare the results computed by the two models. The reason for choosing Case 3 is that it has a higher catalyst loading ( $\beta^* = 18 \text{ kg-Pt/m}^3$ ) which results in more non-uniform temperature profiles than Case 1 ( $\beta^* = 1.8 \text{ kg-Pt/m}^3$ ). These constitute a more critical test for the energy-integral model which assumes quasi-steady state profiles for solid temperature and species; these profiles are monotonic. Moreover, due to the higher solid temperature gradient occurring at the inlet, more grid points are needed there. Hence, non-uniform and more grid points are applied in this case.

Figure 47 shows the comparisons of the gas temperature. At early time ( $t^* = 0.2 \tau_{HT}^*$ ), the energy-integral model predicts lower

gas temperature in the middle of the bed, and both models predict consistently at the inlet and the exit region. As time increases ( $t^* = 1\tau_{HT}^*$ ), the energy-integral model predicts higher gas temperature than the full transient model. At steady state ( $t^* = 3\tau_{HT}^*$ ), comparison between two models is in good agreement. Figure 48 shows that the energy-integral model always predicts lower gas species, but the differences are small. Figure 49 shows the comparison of gas reaction rate. Both models predict the same maximum gas reaction rate and identical gas ignition position.

A comparison of the solid contour plot at  $0.2 \tau_{HT}^*$  in Fig. 50 with those in Fig. 15 shows that the energy-integral model predicts higher solid temperature, lower species and narrower reactive region than the full transient model. These deviations can be seen more closely in Fig. 51. The relatively large discrepancy indicates that the profiles are still in the full transient region and that using the energy-integral model is not valid.

As time increases to  $t^* = 1\tau_{HT}^*$ , deviations between two models are decreasing. From a comparison of Fig. 16 and 53, it seems that the energy-integral model predicts less temperature gradient in the radial direction. However, looking into the in-depth temperature profiles in Fig. 54, we can confirm that the deviations in the solid temperature are small. Near the inlet region ( $x=0, 0.01$ ), both models predictions fall on one line, but separate afterwards ( $x=0.5$ ). Comparisons of the solid species are shown in Fig. 55, and

are in good agreement.

At steady state ( $t^* = 3\tau_{HT}^*$ ), the comparisons of two models in the solid phase (Fig. 56 and 17) are similar as time  $t^* = 1\tau_{HT}^*$ . Because the solid phase has reached the maximum catalytic reaction rate after  $1\tau_{HT}^*$ . During  $1\tau_{HT}^*$  to  $3\tau_{HT}^*$ , the aft part of the solid is receiving heat from the gas phase until the solid reaches steady state. These good agreements of the two models can be seen clearly in the solid in-depth profiles shown in Fig. 57 and 58.

In summary, the comparisons of two models for Case 3 have shown the effect of catalyst loading on the deviations in the gas phase and the solid phase. The highest deviation in the gas temperature occurs at transient  $1\tau_{HT}^*$ , the difference is 4 %. The deviations in the solid phase are decreasing as time increases (maximum 15 % at  $0.2\tau_{HT}^*$ ) and reach the minimum (less than 1 %) at steady state. Due to finer grid size (51 points) used in Case 3 than Case 1 (31 points), computational time is longer in Case 3. The full transient models takes 74 minutes and the energy-integral model takes 46 minutes to reach steady state.

In order to simulate a real monolithic reactor which has a longer solid heat-up time than those in the model's cases, Case 5 is presented. In Case 5, the solid heat-up time is two seconds which is 100 times longer than that in Case 1. This is achieved by increasing the thermal inertia of the solid 100 times. The transient calculation is made by using the energy-integral model.

Figure 59 shows the computed transient results. Comparing the results in Fig. 59 with those in Fig. 6 (Case 1), we find that they are identical. These results are physically reasonable. They imply that the solid heat-up time is the correct time scale to nondimensionalize the transient equations. They also illustrate the advantage for using the energy-integral model. By using the energy-integral model, the computational time is identical in Case 1 and 5. If the full transient model is used, the computational time needed in Case 5 will be 100 times longer than that used in Case 1.

In order to have accurate transient results during whole combustion processes, the switching time from the full transient model to the energy-integral model should be greater than any time scales involved except the solid heat-up time.

## CHAPTER V

### CONCLUSION

Two transient models for a monolithic catalytic igniter with in-depth heterogeneous reaction have been developed and solved numerically to study the ignition and transient phenomena. These models include a full transient model which accounts for the fastest unsteady event, such as mass diffusion across the catalytic layer, and an energy-integral model which accounts for only the slowest heat-up process in the transient. In this study, the reactants used are mixtures of rich-hydrogen/oxygen, and the catalyst is platinum. Two ignition phenomena are observed. First catalytic ignition occurs within the catalytic layer; later, gas ignition is triggered downstream in the gas channel. Once the onset of gas ignition begins, the reactor rapidly approaches steady state, and an abrupt gas temperature rise can be seen. Nevertheless, the solid temperature rises more uniformly due to the effect of low activation energy possessed by the catalyst and the large thermal inertia of the solid. During combustion processes, the front part of the reactor is the catalytic reaction controlled and the aft part is the gas reaction controlled. Moreover, initially the catalytic reaction is kinetically-controlled and becomes diffusionally-controlled after the catalytic ignition is achieved.

Computation using selected model parameters shows that both the oxygen concentration and the temperature gradients can exist across the catalytic layer. The oxygen concentration always decreases from the surface toward the interior. But temperature profile can be nonmonotonic in the reactive layer during the initial fast transient. At a later time, the temperature distribution behaves in a quasi-steady manner and becomes monotonic.

The effect of catalyst loading has been investigated, the study indicates a large effect on the ignition length and ignition delay time. An ignition map using reactor length and catalyst loading has been constructed; the map shows the existence of three regions : no ignition, catalytic ignition only, and catalytic and gas-phase ignitions.

Comparisons between the calculated results using the full transient model and the energy-integral model show that after the initial short transient period (greater than all the time scales except the heat-up time), the two models produce similar results. Therefore, unless short transient information is needed, the use of the energy-integral model will yield correct results and save a lot of computation time. If initial transient is important, the most logical approach is first to use the full transient model and then switch to the energy-integral model.

## REFERENCES

1. Sackheim, R. L.: Survey of Space Applications of Mono-propellant Hydrazine Propulsion System, Tenth Int. Sym. in Space Technology and Science, Tokyo, 1973.
2. Kesselring, J. P.: Catalytic Combustion, "Advanced Combustion Methods ", Academic Press, ed. F. J. Weinberg, 1986.
3. Zurawski, R. L. and Green, J.: Catalytic Ignition of Hydrogen/Oxygen, Presented at the AIAA/ASME/SAE/ASEE 24 th. Joint Propulsion Conf., July, pp. 11-13, 1988.
4. Kelly, J. T., Kendall, R. M., Chu, E. and Kesselring, J. P.: Development and Application of the PROF-HET Catalytic Combustor Code, Paper Presented at the 1977 Fall Meeting Western States Section, The Combustion Institute.
5. T'ien, J. S.: Modeling of Transient Operation of Catalytic Combustion, Combustion Science and Technology, Vol. 26, p. 65, 1981.
6. Sinha, N., Bruno, C., and Bracco, F. V.: Two-Dimensional Transient Combustion of CO / Air on Platinum, J. Physicochem. Hydrodynamics, 1982.
7. Prasad, R., Kennedy, L. A., and Ruckenstein, E.: A Model for the Transient Behavior of Catalytic Combustor, Combustion Science and Technology, Vol. 30, P. 59, 1983.
8. Kesten, A. S. and Sangiovanni, J. J.: Transient Model of Hydrogen/Oxygen Reactor, NASA CR-120799, Feburary, 1971.
9. Weisz, P. B. and Hicks, J. S.: The Behavior of Porous Catalyst Particles in View of Internal Mass and Heat Diffusion Effects, Chemical Engineering Science, Vol. 17, PP 265-275, 1962.
10. Wakao, N. and Smith, J. M.: Diffusion in Catalyst Pellets, Chemical Engineering Science, Vol. 17, PP. 825-834, 1962.
11. Pfefferle, L. D. and Pfefferle, W. C.: Catalysis in Combustion, Catal. Rev. Sci. Eng., Vol.29, pp. 219-267, 1987.
12. Maymo, J. A. and Smith, J. M.: Catalytic Oxidation of Hydrogen-Intrapellet Heat and Mass Transfer, A. I. Ch. E. J. Vol. 12, P. 845, 1966.

13. Hoiberg, J. A., Lyche, B. C. and Foss, A. S.: Experimental Evaluation of Dynamic Model for a Fixed-Bed Catalytic Reactor, A. I. Ch. E. J. Vol. 17, P. 1434, 1971.
14. Miller, F. W. and Deans, H. A.: An Experimental Study of Nonisothermal Effectiveness Factors in a Porous Catalyst, A. I. Ch. E. J. Vol. 13, P. 45, 1967.
15. Skinner, G. B. and Ringrose, G. H.: Ignition Delay of a Hydrogen-Oxygen-Argon Mixture at Relatively Low Temperatures, J. Chem. Phys. Vol. 42, No. 6, P. 2190, 1965.
16. Musiak, J. D.: Experimentally Measured Ignition Delay Times and Proposed Kinetic Model for Hydrogen-Oxygen, M. S. Thesis, Case Western Reserve University, 1989.
17. Meyer, J. W. and Oppenheim, A. K.: On the Shock-Induced Ignition of Explosive Gases, Thirteen Symposium (Int) on Combustion, The Combustion Institute, PP 1153 - 1164, 1971.
18. Kanury, A. M.: Introduction to Combustion Phenomena, Gordon and Beach, New York, 1982.
19. Kays, W. M.: Convective Heat and Mass Transfer, McGraw-Hill, New York, 1966.
20. Ablow, C. M. and Wise, H.: Theoretical Analysis of Combustion in a Monolithic Reactor, Combustion Science and Technology, Vol. 21, P. 35, 1979
21. Frank-Kamenetskii: Diffusion and Heat Transfer in Chemical Kinetics, Plenum Press, New York, 1969.
22. Bidner, M. S. and Calvelo, A.: Transient Analysis of Exothermic Reactions within Catalyst Pellets, Effect of Initial Conditions, Chemical Engineering Science, Vol. 29, PP. 1237-1246, 1974.
23. Anderson, D. A., Tannehill, J. C. and Pletcher, R. H.: Computational Fluid and Heat Transfer, McGraw-Hill, New York, 1984.
24. Lee, E. S.: Quasilinearization and Invariant Imbedding, Academic Press, New York, 1968.

25. Lee, E. S.: Quasilinearization, Difference Approximation, and Nonlinear Boundary Value Problems, A. I. Ch. E. J. Vol. 14, p. 490, 1968.
26. Jameson, A. and Turkel, E.: Implicit Scheme and LU-Decompositions, Mathematics of Computation, Vol. 37, No. 156, P. 385, 1981.
27. Carnahan, B., Luther, H. A. and Wilkes, J. O.: Applied Numerical Methods, John Wiley and Sons, New York 1969.
28. Pfefferle, W. C., Carrubba, R. V., Heck, R. M. and Roberts, G. W.: Catathermal Combustion : A New Process for Low-Emissions Fuel Conversion. ASME Paper 75-WA/FU-1, 1975.
29. Anderson, D. N.: Effect of Catalytic Reactor Length and Cell on Performance. Paper Presented at The Second Workshop on Catalytic Combustion, Raleigh, N. C., June 21-22, 1977.
30. Anderson, D. N.: Preliminary Results From Screening Tests of Commercial Catalysts with Potential Use in Gas Turbine Combustors, Part I, Furnace Studies of Catalyst Activity, NASA TMX-73410, 1976.

## APPENDIX A

### DETERMINATION OF CHEMICAL REACTION RATES

#### A.1 Introduction

The combustion processes in a monolithic reactor include two parts: one is a homogeneous reaction taking place in the bulk gas phase; another is a heterogeneous reaction occurring on the catalyst which is deposited on the solid wall. In this study, rich-hydrogen/oxygen mixtures are used as reactants; the catalyst is platinum. In order to simplify the model formulation, one-step global reaction rates in the gas and the solid phases are desirable.

Concerning the homogeneous chemical reaction occurring in the gas phase, the reaction rate is deduced from the concept of ignition delay. The parameters of the reaction rate are calibrated by experimental data. Experimental data also have shown that the reaction rate depends on deficient oxygen only. On the other hand, for the heterogeneous chemical reaction occurring in the solid phase, several experimental studies have been reviewed. These studies give a consistent activation energy 5500 cal/mole, and the reaction rate depends on the oxygen concentration  $\rho_o^{0.8}$  only.

### A.2 Gas Phase Reaction Rate

We propose a one-step global model for rich-hydrogen/oxygen reaction. The proposed model is based on the spontaneous ignition theory [10], and the parameters of the global rate are calibrated by the experimental data. The overall energy equation for an adiabatic reaction within the gas channel is written as follows.

$$\rho^* C_p^* \frac{d T^*}{d x} = q^* W^* \quad (A.1)$$

A one-step global reaction rate is assumed as.

$$W^* = K^* P^* \rho_0^{*a} \rho^* \exp(-E^*/R^* T^*) \quad [\text{kg-O}_2/\text{m}^3/\text{sec}] \quad (A.2)$$

Let  $T_0^*$  be the initial temperature of the mixture and assume that the preignition reactant consumption is negligible and  $T^* - T_0^* \ll T_0^*$ .

Nondimensional parameters are :

$$\theta = \frac{E^*}{R^* T_0^*} , \quad \eta = \frac{T^* - T_0^*}{T_0^*} \quad (A.3)$$

One approximation is made for exponential term in reaction rate as follows :

$$\begin{aligned} \exp\left(-\frac{E^*}{R T^*}\right) &= \exp\left[\frac{-E^*}{R(T^* - T_o^* + T_o^*)}\right] \\ &= \exp\left[\frac{-E^*}{R T^*}\left(1 + \frac{T^* - T_o^*}{T_o^*}\right)^{-1}\right] \approx \exp\left[-\theta(1-\eta)\right] \end{aligned} \quad (\text{A.4})$$

Substitute Eq.(A.4) into Eq.(A.2), and integrate Eq.(A.1) after arrangement :

$$1 - \frac{1}{e^{\theta\eta}} = \left(\frac{\theta q^* W(T_o^*)}{\rho^* C_p^*}\right) t^* \quad (\text{A.5})$$

When the mixture is ignited, i.e.  $e^{\theta\eta} \Rightarrow \infty$ , the critical time is called the ignition delay time  $t_i$ . Therefore  $t_i$  is defined as:

$$t_i \equiv \frac{\rho^* C_p^* R^* T_o^*}{E^* q^* W(T_o^*)} \quad (\text{A.6})$$

The one-step global reaction rate Eq.(A.2) has four parameters: rate constant  $K^*$ , exponents  $a$  and  $b$ , and activation energy  $E^*$ . They will be determined by fitting the computed ignition delay time into the experimental data[ 11, 12] which supply the ignition delay time for mixtures with various equivalence ratio, pressure and temperature. Therefore, the reaction rates from the fuel-rich to the

stoichiometric case can be calibrated. Procedures for calibration are discussed in the following section.

### Activation energy E\*

Differentiation of Eq.(A.6) with the neglect of  $T_o^*$  relative to  $E^*/R^*$  provides a way of obtaining the activation energy.

$$\frac{d(\ln t_i^*)}{d(1/T_o^*)} = -\frac{E^*}{R^*} \quad (A.7)$$

where  $E^*$  is the slope of plot  $t_i^*$  vs.  $1/T_o^*$ , and value  $E^*$  can be read directly from the experimental curve.

### Exponent of oxygen b

Choose two mixtures (denoted by 1 and 2) with different equivalence ratios, and their ignition delay times are measured under the same temperature and pressure. Then the exponent of oxygen  $b$  can be deduced from the following equation :

$$\frac{t_{i1}^*}{t_{i2}^*} = \frac{C_{p1}^*}{C_{p2}^*} \left( \frac{\rho_{o1}^*}{\rho_{o2}^*} \right)^b \quad (A.8)$$

Exponent of pressure a

Choosing one mixture, two ignition delay times are measured at the same temperature but different pressure level. Then the exponent of pressure a can be defined.

$$\frac{t_{i1}^*}{t_{i2}^*} = \left( \frac{P_2^*}{P_1^*} \right)^a \quad (A.9)$$

Rate constant K\*

Substitute these three parameters  $E^*$ ,  $a^*$ ,  $b^*$  into Eq.(A.6) for a specified mixture for which the ignition delay time is known, the value for rate constant  $K^*$  can be determined.

Critical temperature  $T_{cr}^*$ 

Unfortunately, one global reaction rate can not fit the experimental data over a wide temperature range; the reason is due to the chain reactions involving  $\text{HO}_2$  [13] having opposite effects on the ignition only at low temperature and high pressure conditions. Therefore, two global reaction rates are required to fit the whole temperature range, and the switching point is determined by the critical temperature  $T_{cr}^*$ . For specified pressure and oxygen concentration conditions, if we equalize these two global reaction rates, a critical temperature  $T_{cr}^*$  can be obtained.

Table A.1 lists the corresponding parameters for two sets of gas-phase reaction rates. Fig. A1 shows that the computed ignition delay time based on two derived reaction rates is in good agreement with the measured ones in both fuel-rich and diluted stoichiometric cases.

### **A.3 Catalytic Reaction Rate**

A number of experimental studies [14, 15, 16] to determine the overall rate of rich-hydrogen/oxygen reaction occurring in a porous catalytic layer have been reviewed. Even though they used a different amount of catalyst loading and size of catalyst, and operated at a different temperature range, the conclusions are the same : (1) the catalyst reaction rate depends on the concentration of oxygen only; (2) the exponent of oxygen concentration is 0.8 and the activation energy is 5500 cal/mole. The reason to choose the selected reaction rate reduced from Maymo, et. al [14] is because it is based upon the catalyst loading  $\beta^*$  which is defined as the total amount of catalyst deposited on the solid. Therefore, it will give more flexibility to study the influence of the catalytic reaction rate on ignition phenomena.

A.4 Summary

A set of chemical reaction rates, the unit given as  $[\text{kg-O}_2/\text{m}^3/\text{sec}]$ , has been derived, and it will be used in this study.

Two reaction rates are required in the gas phase, and the switch point is determined by a critical temperature  $T_{cr}^*$ , which is the interception point between these two rates. In this study we have  $T_{cr}^* = 1200^\circ\text{K}$ .

gas-phase reaction rates

when  $T^* \leq T_{cr}^*$

$$W_L^* = 4 \times 10^{18} P^* \rho_o^*^{0.1} \exp(-79480/R^* T^*) \quad (\text{A.10})$$

when  $T^* \geq T_{cr}^*$

$$W_H^* = 9 \times 10^{18} P^* \rho_o^* \exp(-19780/R^* T^*) \quad (\text{A.11})$$

catalytic reaction rate

$$W_c^* = \beta^* 1.772 (\rho_o^* T^*)^{0.8} \exp(-5230/R^* T^*) \quad (\text{A.12})$$

where  $\beta^*$  is the catalyst loading  $[\text{kg-pt}/\text{m}^3]$ .

## APPENDIX B

### DAMKÖHLER ANALOGY

Rewrite the steady state equation (2.55) and (2.56) in the catalytic layer which have been derived in chapter II.

#### species in catalytic layer

$$0 = \frac{\partial}{r \partial r} (r \frac{\partial y_c}{\partial r}) - D'_{\text{am}} y_c^{0.8} \exp(-E_c/T_c) \quad (\text{B.1})$$

#### energy in catalytic layer

$$0 = \frac{\partial}{r \partial r} (r \frac{\partial T_c}{\partial r}) + D'_{\text{at}} y_c^{0.8} \exp(-E_c/T_c) \quad (\text{B.2})$$

The similarity between Eq. (B.1) and (B.2) results in the following equation.

$$\frac{\partial}{r \partial r} \left\{ r \frac{\partial}{\partial r} (D'_{\text{am}} T_c + D'_{\text{at}} y_c) \right\} = 0 \quad (\text{B.3})$$

Integrate Eq. (B.3) once :

$$r \frac{\partial}{\partial r} (D'_{am} T_c + D'_{at} y_c) = \text{constant} \quad (B.4)$$

Integrate Eq.(B.4) from the catalytic layer surface  $r_d$  to the in-depth distance  $r$ .

$$\int_{r_d}^r d (D'_{am} T_c + D'_{at} y_c) = \text{constant} \quad (B.5)$$

$$\left. D'_{am} T_c \right|_{r_d}^r + \left. D'_{at} y_c \right|_{r_d}^r = 0 \quad (B.6)$$

Equation (B.6) is subject to the following boundary conditions :

$$\text{at } r = r_d ; \quad T_c = T_{c,s} \quad (B.7a)$$

$$y_c = y_{c,s} \quad (B.7b)$$

Solving Eq.(B.6) results in the Damköhler Analogy :

$$T_c = T_{c,s} + \frac{D'_{at}}{D'_{am}} (y_{c,s} - y_c) \quad (B.8)$$

## APPENDIX C

### DERIVATION OF FINITE DIFFERENCE EQUATIONS

In the full transient model, the solid-phase equations which include species, energy in the catalytic layer and energy in the substrate layer are solved by the implicit Crank-Nicolson scheme. The finite difference equations are derived in the following steps.

#### species in catalytic layer

transient species equation (2.38)

$$\frac{1}{T_g} \frac{\partial y_c}{\partial t} = \frac{\partial}{r} \frac{\partial r}{\partial r} (r \frac{\partial y_c}{\partial r}) - D'_m y_c^{0.8} \exp \left[ E_c (1 - \frac{1}{T_c}) \right] \quad (C.1)$$

Each term of Eq.(C.1) is discretized by using the central difference. The subscripts i and j denote the axial and the radial grids, respectively.

$$\frac{\partial y_c}{\partial t} = \frac{y_{cj}^{n+1} - y_{cj}}{\Delta t} \quad (C.2)$$

$$\frac{\partial^2 y_c}{\partial r^2} = \frac{1}{2\Delta r^2} \left[ y_{cj+1}^{n+1} + y_{cj+1} - 2(y_{cj}^{n+1} + y_{cj}) + y_{cj-1}^{n+1} + y_{cj-1} \right] \quad (C.3)$$

$$\frac{1}{r} \frac{\partial y_c}{\partial r} = \frac{y_{cj+1}^{n+1} - y_{cj-1}^{n+1} + y_{cj+1} + y_{cj-1}}{4 r_j \Delta r} \quad (C.4)$$

A quasi-linearization technique is implemented on the nonlinear part of catalytic reaction rate, which is obtained from the Taylor series with second and higher orders neglected. By using the form

$$f(T^{n+1}, y^{n+1}) = f(T, y) + \left[ \frac{\partial f}{\partial T}, \frac{\partial f}{\partial y} \right] \begin{bmatrix} T^{n+1} - T \\ y^{n+1} - y \end{bmatrix} \quad (C.5)$$

The nonlinear part of reaction rate is assigned as

$$f(T_c, y_c) = y_c^{0.8} \exp\left(-\frac{E_c}{T_c}\right) \quad (C.6)$$

The linearized reacion rate can be obtained :

$$f(T_c^{n+1}, y_c^{n+1}) = \exp\left(-\frac{E_c}{T_c}\right) \left[ y_c^{0.8} \left( .2 - \frac{E_c}{T_c} \right) + \left( \frac{y_c^{0.8} E_c}{T_c^2} \right) T_c^{n+1} + (.8 y_c^{0.2}) y_c^{n+1} \right] \quad (C.7)$$

Boundary condition at  $r = r_d$  ( where denotes  $j=1$  )

$$\frac{\partial y_{c1}}{\partial r} = Sh (y_{c1} - y_g) \quad (C.8)$$

The second order derivative term at  $r = r_d$  is obtained from the Taylor series

$$y_{c2} = y_{c1} + \left( \frac{\partial y_{c1}}{\partial r} \right) \Delta r + \left( \frac{\partial^2 y_{c1}}{\partial r^2} \right) \frac{\Delta r^2}{2} + O(\Delta r^2) \quad (C.9)$$

Solving Eq. (C.9) for  $\left( \frac{\partial^2 y_{c1}}{\partial r^2} \right)$ , we obtain

$$\frac{\partial^2 y_{c1}}{\partial r^2} = -\frac{2}{\Delta r^2} \left[ y_{c2} - y_{c1} (1 + \Delta r Sh) + \Delta r Sh y_g \right] \quad (C.10)$$

Similarly, at  $r = r_c$ , the boundary condition is (where denotes  $j=N$  )

$$\frac{\partial y_{cN}}{\partial r} = 0 \quad (C.11)$$

$$\frac{\partial^2 y_{cN}}{\partial r^2} = -\frac{2}{\Delta r^2} \left[ y_{cN-1} - y_{cN} \right] \quad (C.12)$$

Substituting Eq. (C.2) through Eq. (C.12) into Eq. (C.1) for  $j = 1, 2, \dots, N$ , the following  $N$  simultaneous algebraic equations can be obtained.

$$\begin{bmatrix} A_1 \end{bmatrix} \begin{bmatrix} y_c^{n+1} \end{bmatrix} = \begin{bmatrix} D_1 \end{bmatrix} \quad (C.13)$$

where  $[A_1]$  represents the following tridiagonal matrix:

$$\begin{bmatrix} A_1 \end{bmatrix} = \begin{bmatrix} a_{11} & c_1 & 0 & \cdot & \cdot \\ b_2 & a_{12} & c_2 & \cdot & \cdot \\ 0 & b_3 & a_{13} & \cdot & \cdot \\ \cdot & \cdot & \cdot & \cdot & c_{N-1} \\ \cdot & \cdot & \cdot & b_N & a_{1N} \end{bmatrix} \quad (C.14)$$

where  $\begin{bmatrix} y_c^{n+1} \end{bmatrix}$  and  $\begin{bmatrix} D_1 \end{bmatrix}$  represent the following vectors :

$$\begin{bmatrix} y_c^{n+1} \end{bmatrix} = \begin{bmatrix} y_{c1}^{n+1} \\ y_{c2}^{n+1} \\ \cdot \\ \cdot \\ y_{cN}^{n+1} \end{bmatrix} \quad \text{and} \quad \begin{bmatrix} D_1 \end{bmatrix} = \begin{bmatrix} D_{11} \\ D_{12} \\ \cdot \\ \cdot \\ D_{1N} \end{bmatrix} \quad (C.15)$$

with

$$\sigma = \frac{\Delta t}{2\Delta r^2} \quad (C.16)$$

$$D''_{amj} = \Delta t D'_{am} \exp \left[ E_c \left( 1 - \frac{1}{T_{cj}} \right) \right] \quad (C.17)$$

$$a_{11} = \frac{-1}{T_{g1}} - 4\sigma(1 + \Delta r S_h) + \frac{\Delta t S_h}{r_d} - .8 D''_{am1} y_{c1}^{0.2} \quad (C.18)$$

$$c_1 = b_N = 4\sigma \quad (C.19)$$

$$a_{1N} = \frac{-1}{T_{g1}} - 4\sigma - .8 D''_{amN} y_{cN}^{0.2} \quad (C.20)$$

$$D_{11} = \frac{-y_{c1}}{T_{g1}} - (4\sigma \Delta r - \frac{\Delta t}{r_d}) S_h y_{g1} + D''_{am1} y_{c1}^{0.8} \left[ .2 - \frac{E_c}{T_{c1}} (1 - \frac{T_{c1}^{n+1}}{T_{c1}}) \right] \quad (C.21)$$

$$D_{1N} = \frac{-y_{cN}}{T_{g1}} + D''_{amN} y_{cN}^{0.8} \left[ .2 - \frac{E_c}{T_{cN}} (1 - \frac{T_{cN}^{n+1}}{T_{cN}}) \right] \quad (C.22)$$

when  $j = 2, 3, \dots, N-1$

$$a_{1j} = \frac{-1}{T_{g1}} - 2\sigma - .8 D''_{amj} y_{cj}^{0.2} \quad (C.23)$$

$$r_j = r_d + (j-1)\Delta r \quad ; \quad r_s \leq r_j \leq r_c \quad (C.24)$$

$$b_j = \sigma - \frac{1}{r_j} (\frac{\Delta t}{4\Delta r}) \quad (C.25)$$

$$c_j = \sigma + \frac{1}{r_j} (\frac{\Delta t}{4\Delta r}) \quad (C.26)$$

$$D_{1j} = -b_j y_{j-1} + \left[ 2\sigma - \frac{1}{T_{g1}} + D''_{amj} (.2 - \frac{E_c}{T_{cj}}) y_{cj}^{0.2} \right] y_{cj} - c_j y_{cj+1} \quad (C.27)$$

$$+ D''_{amj} T_{cj}^{n+1} \frac{y_{cj}^{0.8} E_c}{T_{cj}^2}$$

energy in catalytic layer

Applying the same technique on the energy equation in the catalytic layer, the following N simultaneous algebraic equations can be obtained.

$$\begin{bmatrix} A_2 \end{bmatrix} \begin{bmatrix} T_c^{n+1} \end{bmatrix} = \begin{bmatrix} D_2 \end{bmatrix} \quad (C.28)$$

$$\begin{bmatrix} A_2 \end{bmatrix} = \begin{bmatrix} a_{21} & c_1 & 0 & . & . \\ b_2 & a_{22} & c_2 & . & . \\ 0 & b_3 & a_{23} & . & . \\ . & . & . & . & c_{N-1} \\ . & . & . & b_N & a_{2N} \end{bmatrix} \quad (C.29)$$

$$\begin{bmatrix} T_c^{n+1} \end{bmatrix} = \begin{bmatrix} T_{c1}^{n+1} \\ T_{c2}^{n+1} \\ . \\ . \\ T_{cN}^{n+1} \end{bmatrix} \quad \text{and} \quad \begin{bmatrix} D_2 \end{bmatrix} = \begin{bmatrix} D_{21} \\ D_{22} \\ . \\ . \\ D_{2N} \end{bmatrix} \quad (C.30)$$

with

$$D''_{atj} = \Delta t D'_{at} \exp \left[ E_c \left( 1 - \frac{1}{T_{cj}} \right) \right] \quad (C.31)$$

$$a_{21} = -\delta_c - 4\sigma (1 + \Delta r B_c) + \frac{\Delta t B_c}{r_d} + D''_{at1} \frac{y_{c1}^8 E_c}{T_{c1}^2} \quad (C.32)$$

$$a_{2N} = -\delta_c - 4\sigma - \lambda (4\sigma \frac{\Delta r}{\Delta r_1} + \frac{\Delta t}{\Delta r_1 r_c}) + D''_{atN} \frac{y_{cN}^8 E_c}{T_{cN}^2} \quad (C.33)$$

$$D_{21} = -\delta_c T_{c1} - (4\sigma \Delta r + \frac{\Delta t}{r_d}) B_c T_{g1} - D''_{at1} y_{c1}^8 \left[ 2 - \frac{E_c}{T_{c1}} + \frac{.8 y_{c1}^{n+1}}{y_{c1}} \right] \quad (C.34)$$

$$D_{2N} = -\delta_c T_{cN} - (4\sigma \Delta r + \frac{\Delta t}{r_c}) \lambda \frac{T_{s2}^{n+1}}{\Delta r_1} - D''_{atN} y_{cN}^8 \left[ 2 - \frac{E_c}{T_{cN}} + \frac{.8 y_{cN}^{n+1}}{y_{cN}} \right] \quad (C.35)$$

when  $j = 2, 3, \dots, N-1$

$$a_{2j} = -\delta_c - 2\sigma + D''_{atj} \frac{y_{cj}^8 E_c}{T_{cj}^2} \quad (C.36)$$

$$D_{2j} = -b_j T_{cj-1} + [2\sigma - \delta_c] T_j - C_j T_{cj+1} - D''_{atj} y_{cj}^8 \left[ 2 - \frac{E_c}{T_{cj}} + \frac{.8 y_{cj}^{n+1}}{y_{cj}} \right] \quad (C.37)$$

where  $\Delta r_1$  and  $\Delta r_2$  are the radial space steps used in the catalytic and the substrate layers, respectively.

energy in substrate layer

$$\begin{bmatrix} A_3 \end{bmatrix} \begin{bmatrix} T_s^{n+1} \end{bmatrix} = \begin{bmatrix} D_3 \end{bmatrix} \quad (C.38)$$

$$\begin{bmatrix} A_3 \end{bmatrix} = \begin{bmatrix} a_{31} & c'_1 & 0 & \cdot & \cdot & \cdot \\ b'_2 & a_{32} & c'_2 & \cdot & \cdot & \cdot \\ 0 & b'_3 & a_{33} & \cdot & \cdot & \cdot \\ \cdot & \cdot & \cdot & \cdot & c'_{N-1} & \cdot \\ \cdot & \cdot & \cdot & b'_N & a_{3N} & \cdot \end{bmatrix} \quad (C.39)$$

$$\begin{bmatrix} T_s^{n+1} \end{bmatrix} = \begin{bmatrix} T_{s1}^{n+1} \\ T_{s2}^{n+1} \\ \cdot \\ \cdot \\ T_{sN}^{n+1} \end{bmatrix} \quad \text{and} \quad \begin{bmatrix} D_3 \end{bmatrix} = \begin{bmatrix} D_{31} \\ D_{32} \\ \cdot \\ \cdot \\ D_{3N} \end{bmatrix} \quad (C.40)$$

with

$$\sigma_1 = \frac{\Delta t}{2\Delta r_1^2} \quad (C.41)$$

$$a_{31} = -\delta_s - 4\sigma_1 - \frac{1}{\lambda} (4\sigma_1 \frac{\Delta r_1}{\Delta r} + \frac{\Delta t}{\Delta r r_c}) \quad (C.42)$$

$$a_{3N} = -\delta_s - 4\sigma_1 \quad (C.43)$$

$$D_{31} = -\delta_s T_{s1} - \left( 4\sigma \Delta r_1 - \frac{\Delta t}{r_c} \right) \frac{1}{\lambda} \frac{T_{cN-1}^{n+1}}{\Delta r} \quad (C.44)$$

$$D_{3N} = -\delta_s T_{cN} \quad (C.45)$$

$$c'_1 = b'_N = 4\sigma_1 \quad (C.46)$$

when  $j = 2, 3, \dots, N-1$

$$r_j = r_c + (j-1)\Delta r \quad ; \quad r_c \leq r_j \leq r_s \quad (C.47)$$

$$b'_j = \sigma_1 - \frac{1}{r_j} \left( \frac{\Delta t}{4\Delta r_1} \right) \quad (C.48)$$

$$c'_j = \sigma_1 + \frac{1}{r_j} \left( \frac{\Delta t}{4\Delta r_1} \right) \quad (C.49)$$

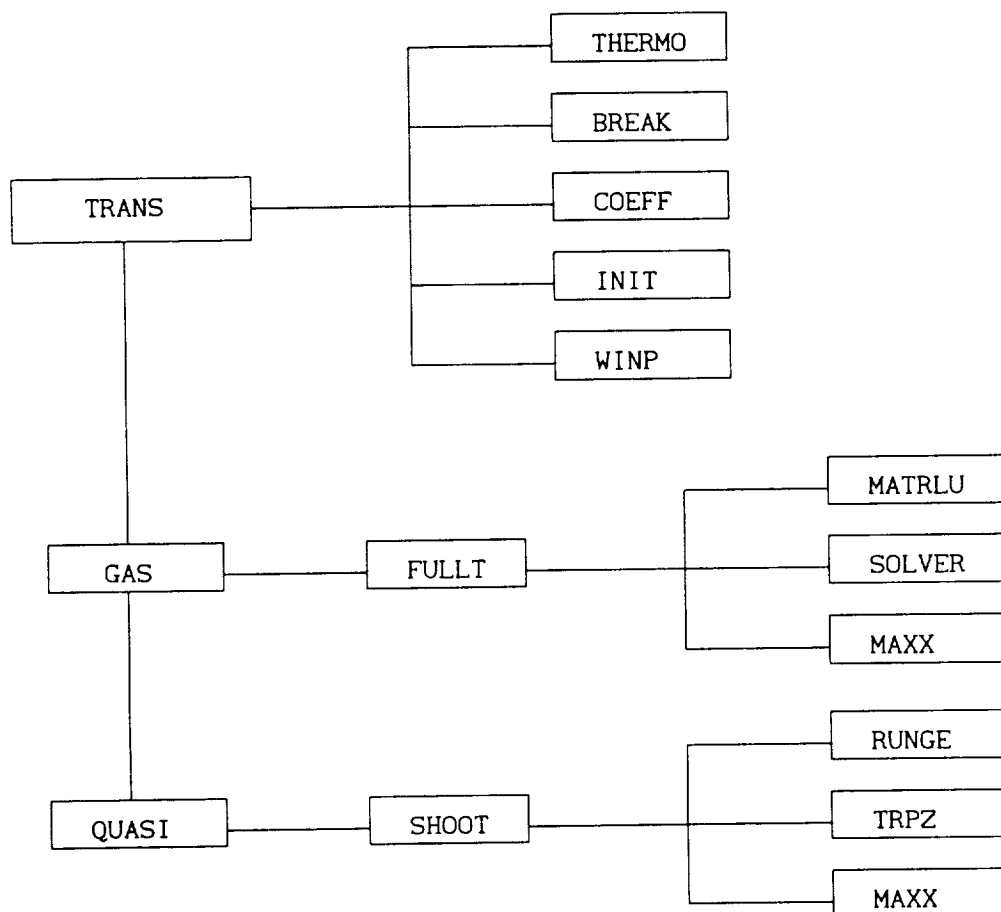
$$a_{3j} = -\delta_s - 2\sigma_1 \quad (C.50)$$

$$D_{3j} = -b'_j T_{sj-1} + \left[ 2\sigma_1 - \delta_s \right] T_j - c'_j T_{sj+1} \quad (C.51)$$

## APPENDIX D

### COMPUTER PROGRAMS

#### D.1 Flow Chart



## D. 2 PROGRAMS

## PROGRAM TRANS

```

C -----
C ***** CATALYTIC COMBUSTOR START-UP TRANSIENT
C -----
REAL LF,MMIX,MOL0
COMMON/THER1/ YHO(31),YO(31),YH(31),YOS(31),YHOV(31),YHOSV(31),
  + YIC(31),YLI(31),XH(31),RNK(31),WG(31),ROI(31),TS(31),T(31),
  + XX(31),DX(31),DY,DT,ROI,YHI,YO1,T1,CP,DS,XLS,XLDS,RT(31)
COMMON/THER2/B(21),C(21),BI(21),CI(21),B3(21),C3(21),RR(21),RS(21)
COMMON/THER3/SI(31),BC(31),YRR(31,21),TSI(31,21),DAM,DAT
  + ,YOS(31,21),TS2(31,21),WS(31,21),DEL(31)
COMMON/THER4/ TgNEW(31),YONEW(31),RONEW(31),UNEW(31),U(31)
common/ther5/wsmax(31),tsrm(31)

C -----
OPEN(UNIT=9,FILE='OU1',STATUS='UNKNOWN')
OPEN(UNIT=10,FILE='OU2',STATUS='UNKNOWN')
OPEN(UNIT=11,FILE='OU3',STATUS='UNKNOWN')
OPEN(UNIT=12,FILE='OU4',STATUS='UNKNOWN')
OPEN(UNIT=13,FILE='OU5',STATUS='UNKNOWN')
OPEN(UNIT=14,FILE='OU6',STATUS='UNKNOWN')
OPEN(UNIT=15,FILE='OU7',STATUS='UNKNOWN')
OPEN(UNIT=16,FILE='OU8',STATUS='UNKNOWN')
OPEN(UNIT=17,FILE='OU9',STATUS='UNKNOWN')
OPEN(UNIT=18,FILE='O10',STATUS='UNKNOWN')
OPEN(UNIT=19,FILE='O11',STATUS='UNKNOWN')
OPEN(UNIT=30,FILE='dat1')

C -----
DATA PF,LF,BS,N ,NY / 209.6 , 1100. , 1E-8, 31, 21/
DATA XLEW1,W0,WH,GC / L , 32 . 2 , .08205 /
DATA XPR,AOAS,xki / .719 . 2 . .04 /
DATA CL,AL,BL,EL,DHRO / 4.E18 . -L5 . 0.1 . 79480., 57800. /
DATA CH,AH,BH,EH,DELT / 9.E5 . L . L , 19870., .99/
DATA ROOT1,ROOT2,KOUNT/ 0. , L , L /
DATA ALPHI,CC2,ES / 1.E-5 , 2.5 . 5320. /
DATA VOID,FRA / .5 . .67/

C -----
C *** INPUT PARAMETERS
C REACTION 1. A H2 + O2 = 2 H2O + ( A-2 ) H2 (GAS PHASE)
C REACTION 2. 2H2 + O2 = 2H2O (SOLID PHASE)
C EL,EH,ES = ACTIV. ENERGY FOR GAS (LOW, HIGH T), SOLID (CAL/MOL)
C XLS , DS = BED LENGTH (M), CHANNEL HYDRAUL DIA. (M)
C DEF = EFFECTIVE DIFFUSIVITY OF O2 IN CATALYST (M2/S)
C SCC , SC = HEAT CAPACITY OF CATALYST, SUBSTRATE (CAL/KG/K)
C SRC , SR = DENSITY OF CATALYST, SUBSTRATE (KG/M3)
C BVI = LOADING FACTOR
C DY, FRA = RADIAL GRID LENGTH, RATIO OF CATALYTIC LAYER
C THICKNESS / HALF WALL THICKNESS
C DT, DTS = TIME STEP IN FULL TRANSIENT, ENERGY INTEGRAL MODEL
C KMAX, KST = MAX COMPUTATION TIME, TIME TO SWITCH MODEL
C -----

READ (30, 9) SKC, SRC, SCC, SK, SR, SC, DEF
READ (30, 9) DS, XLS, RM, XPI, TI, UTUS, BVI

```

```

      READ (30,10) DT, DTS, FRA, DY, KST, KMAX
10  FORMAT(7E10.3)
10  DORMAT(4E10.3,2I10)
C -----
C **** OPERATING PARAMETERS AT INITIAL UPSTREAM (I.U.)
C TI , UI   = I.U. TEMP.(K)           . VEL. (M/S)
C XPI , ROI  = I.U. PRESSURE (ATM.)   , DENSITY (KG/M3)
C CP , GC   = I.U. SPECI. HEAT (CAL/KG/K) , GAS CONST.(M3-ATM/KG/S)
C YHI , YOI  = I.U. MASS FRACTION OF H2 , O2
C XKI , XPHI = I.U. CONDUCT. (CAL/M/S/K) , H2/O2 EQUIV. RATIO
C ALPHI    = O2 IN CATALYST
C XLEWI,    = LEW. NO OF O2
C -----
C UI = UIUS*(1.0+AOAS)/AOAS
C -----
C **** THERMO. DATA
C -----
C CALL THERMO (RM,DHRO,MOLO,MMIX,TAB,DHR,AA,XPHI,GC,XPI)
C -----
C **** BREAK TEMP FOR GAS PHASE TWO-EQ MODEL
C -----
C CALL BREAK (CL,AL,BL,EL,CH,AH,BH,EH,TCR,MOLO,DHR,XPI)
C -----
C **** GAS PHASE REACTION CONSTANTS
C -----
C CL = CL/XPI**(-AL)*(ROI*YOI)**BL
C EL = EL/TI/1.987
C EH = EH/TI/1.987
C QV = DHR/CP/TI
C GRI= XLS/ROI/UI
C XLEI23= XLEWI**.667
C XMU = 1.05E-5+(TI-373.)*1.5E-8
C REY = UIUS*DS*ROI/XMU
C ALPHA = XKI/ROI/CP
C AD2UL = (ALPHA/DS/DS)/(UI/XLS)
C -----
C **** SOLID PHASE CONSTANTS
C -----
C E2 = ES/TI/1.987
C QV2 = DHR/SCC/TI
C THIC=.433*DS/AOAS/2.
C RLI =THIC*FRA
C RL2 =THIC*(1.-FRA)
C RII =DS/2./RLI
C RI2 =RII+I.
C RI3 =RI2+RL2/RLI
C DAT =BV*QV2*RLI**2.*SCC/SKC
C DAM =BV*RLI**2./DEF/YOI/ROI
C -----
C **** MATRIX COEFF TO SOLVE TS & YOS EQ
C -----
C CALL COEFF (N,NY,NR,NT,RII,RI2,RI3,DYZ,DTY,X2,X4,DZ,DTZ,Z2,Z4,SKC,
C +SK,RK)
C -----
C **** ENERGY INTEGRAL EQ. CONSTANTS

```

```

C -----
AP =DAT/DAM
H2 =DTS*DAT*SKC*2./XKL/3.66
RC =(SR*SC*(RI3**2.-RI2**2.)*SRC*SCC*(RI2**2.-RI1**2.))/2.
ROC1=SRC*SCC/RC
ROC2=SR*SC*(RI3**2.-RI2**2.)/2./RC
C -----
C **** TIME SCALES
C -----
tres=xls/ui
TMC =VOID*RL1**2./DEF
TTC =RL1**2.*SRC*SCC/SKC
TTS =RL2**2.*SR*SC/SK
tts2=r11**2.*sr*sc/sk
XLE2=TTS2/TMC
DIFF=2.*VOID*RL1**2./XLE123/3.66/ALPHA
TOTAL=2.*RC*RL1**2./3.66/XKI
C -----
C **** INITAL CONDITIONS (GAS & SOLID PHASE)
C -----
CALL INIT (N,NY,NR,GC,MMIX,UI,TMC,GCC,DTX,DLT,GR3,DMASS,TIME)
C -----
C-- INPUT PRINTOUT
C -----
CALL WINP (RM,XPI,UIUS,KMAX,SKC,SRC,SCC,DEF,BVCC,KP,SK,SR,SC,RL1,
+RL2,TCR,XPHI,MOLO,TAB,REY,TMC,TTC,TTS,XLE,XLE2,TOTAL,N,NY,NR,
+DIFF,NT)
C -----
C **** TIME INTEGRATION
C -----
XNU0=.885*SQRT(AOAS*XPR*REY)
555 CONTINUE
ROOT=.5*(ROOT1+ROOT2)
IF(ROOT.LE.0.1)YNU=.0444/ROOT+3.46-1.34*ROOT
IF(ROOT.GT.0.1)YNU=.011/ROOT+3.66
YROOT=YNU-XNU0
IF(ABS(YROOT).LT.0.01) GO TO 666
IF(YROOT.GT.0.0) ROOT1=ROOT
IF(YROOT.LE.0.0) ROOT2=ROOT
GO TO 555
666 CONTINUE
KOUNT=KOUNT+1
KOU=KOUNT-1
if (kou .lt. kst) then
  TIME=TIME+DT*TMC
else
  time=time+dts*total
endif
C -----
C **** GAS PHASE EQ. (FULL TRANSIENT EQ. AND EXPLICIT METHOD )
C -----
if (kou .lt. kst) then
  CALL GAS (N,QV,GR1,CL,BL,EL,CH,BH,EH,TCR,XLE123,GCC,XPI,DTX,DLT,
+ ROOT,AD2UL,XKI)
C -----

```

```

tts2=r11**2.*sr*sc/sk
XLE2=TT52/TMC
DIFF=2.*VOID*RL1**2./XLE123/3.66/ALPHA
TOTAL=2.*RC*RL1**2./3.66/XKI
C -----
C **** INITIAL CONDITIONS (GAS & SOLID PHASE)
C -----
CALL INIT (N,NY,NR,GC,MMIX,UI,TMC,GCC,DTX,DLT,CR3,DMASS,TIME)
C-----
C-- INPUT PRINTOUT
C-----
CALL WINP (RM,XPI,UIUS,KMAX,SKC,SRC,SCC,DEF,BVCC,KP,SK,SR,SC,RL1,
+RL2,TCR,XPHI,MOLO,TAB,REY,TMC,TTC,TT5,XLE,XLE2,TOTAL,N,NY,NR,
+DIFF,NT)
C -----
C *** TIME INTEGRATION
C -----
XNUO=.885*SQRT(AOAS*XPR*REY)
555 CONTINUE
ROOT=.5*(ROOT1+ROOT2)
IF(ROOT.LE.0.1)YNU=.0444/ROOT+3.46-1.34*ROOT
IF(ROOT.GT.0.1)YNU=0.011/ROOT+3.66
YROOT=YNU-XNUO
IF(ABS(YROOT).LT.0.01) GO TO 666
IF(YROOT.GT.0.0) ROOT1=ROOT
IF(YROOT.LE.0.0) ROOT2=ROOT
GO TO 555
666 CONTINUE
KOUNT=KOUNT+1
KOU=KOUNT-1
if (kou .lt. kst) then
  TIME=TIME+DT*TMC
else
  time=time+dts*total
endif
C -----
C *** GAS PHASE EQ. (FULL TRANSIENT EQ. AND EXPLICIT METHOD )
C -----
if (kou .lt. kst) then
  CALL GAS (N,QV,GRI,CL,BL,EL,CH,BH,EH,TCR,XLE123,GCC,XPI,DTX,DLT,
+ ROOT,AD2UL,XKI)
C -----
C *** GAS PHASE EQ. (QUASI-STEADY EQ. AND RUNGE -KUTTA METHOD)
C -----
else
  CALL QUASI (N,QV,DMASS,GRI,CL,BL,EL,CH,BH,EH,TCR,XPHI,XLE123,
+ KOU,XPI,ROOT,AD2UL,XKI)
endif
C -----
C *** GAS PHASE REACTION RATE
C -----
DO 700 I=1,N
ELL=EL/T(I)
EHH=EH/T(I)
IF ((T(I).LE.TCR).AND.(ELL.LT.100.)) THEN
  WC(I)=CL*(RO(I)*YO(I))**BL/EXP(EL/T(I))
ELSEIF ((T(I).LE.TCR).AND.(ELL.GE.100.)) THEN
  WC(I)=0.
ENDIF
IF ((T(I).GT.TCR).AND.(EHH.LT.100.)) THEN

```

```

SUBROUTINE THERMO (RM,DHRO,MOLO,MMIX,TAB,DHR,AA,XPHI,CC,XPI)
C-----
C-- THERMO DATA
C-----
      REAL MMIX,MOLO
      COMMON/THERM/ YHO(31),YO(31),YH(31),YOS(31),YHOV(31),YHOSV(31),
     + YIC(31),YLI(31),XJH(31),RNK(31),WC(31),RO(31),TS(31),T(31),
     + XX(31),DX(31),DY,DT,ROI,YHI,YOI,TT,CP,DS,XLS,XLDS,RT(31)
C -----
C *** DHR    = HEAT OF REACTION (CAL/KG-02)
C   CP     = SPECIFIC HEAT OF MIXTURE (CAL/KG-K)
C   TAB    = ADABATIC TEMP (K)
C   AA     = NO. OF MOLES FOR H2
C   XPHI   = EQUIVALENCE RATIO
C   A1,B1,C1 = COEFF. OF CP FOR H2
C   A2,B2,C2 = COEFF. OF CP FOR H2O
C   A3,B3,C3 = COEFF. OF CP FOR O2
C -----
      DATA A1,B1,C1,A2,B2,C2,T0/ 6.947, 1.E-4, 1.6E-7, 7.256, 1.149E-3,
     + 9.43E-8, 298./
      DATA A3,B3,C3/ 6.148, 1.551E-3, 3.07E-7/
C
      F(X)=(AA-2.)*(A1*(X-T0)-B1*(X*X-T0*T0)+C1*(X**3.-T0**3.))+2.*(
     +(X-T0)+B2*(X*X-T0*T0)+C2*(X**3.-T0**3.))-CC
C
      AA=16.*RM
      MOLO=1./(AA+1.)
      MMIX=MOLO*32.+1.-MOLO)*2.
      YHI=2./MMIX*(1.-MOLO)
      YOI=YHI/RM
      XPHI=RM*3.
      ROI=XPI*MMIX/CC/TT
      XLDS=XLS/DS
C -----
C   CP AND DHR
C -----
      CPO1 = 6.148+3.1E-3*T0-9.23E-7*T0*T0
      CPH1 = 6.947-2.0E-4*T0+4.81E-7*T0*T0
      CPH01 = 7.256+2.3E-3*T0+2.83E-7*T0*T0
      CPO2 = 6.148+3.1E-3*TT-9.23E-7*TT*TT
      CPH2 = 6.947-2.0E-4*TT+4.81E-7*TT*TT
      CPH02 = 7.256+2.3E-3*TT+2.83E-7*TT*TT
      DHH = A1*(TT-T0)-B1*(TT*TT-T0*T0)+C1*(TT**3.-T0**3.)
      DHHO = A2*(TT-T0)+B2*(TT*TT-T0*T0)+C2*(TT**3.-T0**3.)
      DHO = A3*(TT-T0)+B3*(TT*TT-T0*T0)-C3*(TT**3.-T0**3.)
      DHR = (DHRO+DHH+.5*DHO-DHHO)*1.E3*2./32.
      CP = (MOLO*CPO2+(1.-MOLO)*CPH2)*1000./MMIX
C -----
C   ADIABATIC FLAME TEMP CALCULATION
C -----
      CC=2.*DHRO+AA*DHH+DHO
      XI=100.
      XF=10000.
      A=F(XI)
      9  B=F(XF)
      IF (A*B) 99,99,40
      99  WW=.5*(XF+XI)
      IF (ABS(WW-XI)-1.E-3) 40,40,41
      41  YI=F(WW)
      IF (YI*A) 30,30,31

```

```

30  XF=WW
    GO TO 99
31  XI=WW
    GO TO 99
40  TCR=WW/TI
    RETURN
    END

```

```

SUBROUTINE BREAK (CL,AL,BL,EL,CH,AH,BH,EH,TCR,MOLO,DHR,XPI)
C-----
C **** THE BREAK POINT FOR THE GAS PHASE REACTION RATE
C-----
REAL MOLO
COMMON/THER1/ YHO(31),YO(31),YH(31),YOS(31),YHOV(31),YHOSV(31),
+ YIC(31),YLI(31),XJH(31),RNK(31),WC(31),RO(31),TS(31),T(31),
+ XX(31),DX(31),DY,DT,ROI,YHI,YOI,PI,CP,DS,XLS,XLDS,RT(31)
C
F(X)=C1+C2* ALOG(C3*X)+C4/X
C
C1=A LOG(CL*EL/CH/EH*XPI**(AL-AH)**(MOLO**2.)**(BL-BH))
C2=8H-8L
C3=.08205/XPI
C4=(EH-EL)/1.987
XI=100.
XF=1.E6
A=F(XI)
9  B=F(XF)
IF (A*B) 99,99,40
99  WW=.5*(XF+XI)
IF (ABS(WW-XI)-1.E-3) 40,40,41
41  YI=F(WW)
IF (YI*A) 30,30,31
30  XF=WW
GO TO 99
31  XI=WW
GO TO 99
40  TCR=WW/TI
RETURN
END

```

```

SUBROUTINE COEFF (N,NY,NR,NT,R11,R12,R13,DYZ,DTY,X2,X4,DZ,DTZ,Z2,
+ Z4,SKC,SK,RK)
C -----
C ***** CONSTANTS FOR THE SOLID PHASE
C -----
COMMON//THER1// YHO(31),YO(31),YH(31),YOS(31),YHOV(31),YHOSV(31),
+ YIC(31),YL1(31),XJH(31),RNC(31),WC(31),RO(31),TS(31),T(31),
+ XX(31),DX(31),DY,DT,ROI,YHI,YOL,TI,CP,DS,XLS,XLDS,RT(31)
COMMON//THER2//B(21),C(21),BI(21),CI(21),B3(21),C3(21),RR(21),RS(21)
XLLN=DT/2./DY/DY
BETT=DT/4./DY
DTY=DT/DY
X2 =2.*XLLN
X4 =4.*XLLN
DO 100 J=1,NY
  RT(J)=FLOAT(J-1)*DY
100 RR(J)=RT(J)*DY+R11
  DO 200 J=2,NY-1
    B(J) =XLLN-BETT/RR(J)
    C(J) =XLLN+BETT/RR(J)
    BI(J) =B(J)
200 CI(J) =C(J)
    C(1) =-X4
    CI(1) =-X4
    B(NY) =-X4
    BI(NY)=-X4
C -----
C ***** SUBSTRATE LAYER CONSTANTS
C -----
DZ=2.*DY
NR=(R13-R12)/DZ+1
IF (NR .EQ. 1) THEN
  DZ=R13-R12
  NR=2
ENDIF
XLLN2=DT/2./DZ/DZ
BETT2=DT/4./DZ
DTZ=DT/DZ
DYZ=DY/DZ
Z2 =2.*XLLN2
Z4 =4.*XLLN2
NT=NY+NR-1
DO 300 J=1,NR
300 RS(J)=FLOAT(J-1)*DZ+R12
  DO 400 K=2,NR-1
    B3(K) =XLLN2-BETT2/RS(K)
400 CI(K) =XLLN2+BETT2/RS(K)
  DO 500 J=1,NR-1
500 RT(NY+J)=FLOAT(J)*DZ+1.
    CI(1) =-Z4
    B3(NR)=-Z4
    RK=SKC/SK
    RETURN
END

```

```

SUBROUTINE INIT (N,NY,NR,CC,MMIX,UI,TMC,GCC,DTX,DLT,GR3,DMASS,TIME)
COMMON/THER1/ YHO(31),YO(31),YH(31),YOS(31),YHOV(31),YHOSV(31),
+ YIC(31),YLI(31),XJH(31),RNK(31),WG(31),RO(31),TS(31),T(31),
+ XX(31),DX(31),DY,DT,ROI,YHI,YOI,TI,CP,DS,XLS,XLDS,RT(31)
COMMON/THER3/SH(31),BC(31),YRR(31,21),TS(31,21),DAM,DAT
+ ,YOS(31,21),TS2(31,21),WS(31,21),DEL(31)
COMMON/THER4/ TgNEW(31),YONEW(31),RONEW(31),UNEW(31),U(31)
REAL MMIX
C-----
C INITIAL CONDITIONS FOR QUASI-STEADY GAS PHASE EQUATION
C-----
DO 100 I=1,N
T (I)=1.
u (I)=1.
100 RO(I)=1.
YO(1) =1.
YH(1) =1.
YHO(1)=0.
ROI(1) =1.
DMASS=RO(1)*U(1)
C-----
C INITIAL CONDITION FOR FULL TRANSIENT GAS PHASE EQUATION
C-----
TIME = 0.
YONEW(1)=1.
TgNEW(1) =1.
RONEW(1)=1.
UNEW (1)=1.
GCC=CC/MMIX
DLT=XLS/UI/TMC
DTX=DT/DDX
GR3=DTX/DLT
C-----
C INITIAL CONDITIONS OF THE CATALYTIC AND SUBSTRATE LAYER
C-----
DO 200 I=1,N
TS(I) =1.
YOS(I)=0.
DEL(I)=.95
DO 300 J=1,NY
TS1 (I,J)=1.
300 YOS1(I,J)=0.
DO 400 K=1,NR
400 TS2 (I,K)=1.
200 CONTINUE
RETURN
END

```

```

SUBROUTINE WINP (RM,XPI,UIUS,KMAX,SKC,SRC,SCC,DEF,BVCC,KP,SK,SR,SC
+ ,RL1,RL2,TCR,TIGN,XPHI,MOLO,TAB,REY,TMC,TTC,TTS,XLE,XLE2,TOTAL,N,
+ NY,NR,DIFF,NT)
C-----
C** INPUT PRINTOUT
C-----
COMMON/THER1/ YHO(31),YO(31),YH(31),YOS(31),YHOV(31),YHOSV(31),
+ YIC(31),YL1(31),XJH(31),RNK(31),WG(31),RO(31),TS(31),T(31),
+ XX(31),DX(31),DY,DT,ROI,YHI,YOI,PI,CP,DS,XLS,XLDS,RT(31)
COMMON/THER3/SH(31),BC(31),YRR(31,21),TS1(31,21),DAM,DAT
+ ,YOS1(31,21),TS2(31,21),WS(31,21),del(31)
WRITE(19,12)
WRITE(19,22)RM,XPHI,XPI,UIUS,ROI,KP,KMAX
WRITE(19,13)
13 FORMAT(/3X,'TI',8X,'TAB',7X,'TIGN',6X,'TCR')
WRITE(19,33)TI,TAB,TIGN,TCR
WRITE(19,23)
23 FORMAT(/3X,'TMC',7X,'TTC',7X,'TTS',7X,'DIFF',6X,'TOTAL')
WRITE(19,33)TMC,TTC,TTS,DIFF,TOTAL
WRITE(19,15)
15 FORMAT(/3X,'K-S',7X,'RO-S',6X,'CP-S',6X,'DAM',7X,'DAT',7X,'XLE'
+ ,7X,'XLE2')
WRITE(19,33)SK,SR,SC,DAM,DAT,XLE,XLE2
WRITE(19,17)
17 FORMAT(/3X,'REY',7X,'MOLO',6X,'CP',9X,'DT',8X,'DS',8X,'XLS')
WRITE(19,33)REY,MOLO,CP,DT,DS,XLS
WRITE(19,14)
14 FORMAT(/3X,'K-C',7X,'RO-C',6X,'CP-C',6X,'DEF',7X,'RL1',7X,'RL2')
WRITE(19,33)SKC,SRC,SCC,DEF,RL1,RL2
WRITE(19,18)
18 FORMAT(/3X,'N',9X,'NY',8X,'NR',8X,'NT')
WRITE(19,19)N,NY,NR,NT
19 FORMAT(4I10/)
22 FORMAT (5E10.3,4X,I6,4X,I6)
33 FORMAT (7E10.3)
      RETURN

```

```

SUBROUTINE GAS (N,QV,CRI,CL,BL,EL,CH,BH,EH,TCR,XLE123,GCC,XPI,
+ DTX,DLT,ROOT,AD2UL,XXI)
C-----
C-- FULL TRANSIENT GAS-PHASE EQUATION SOLVED BY EULER UPWIND EXPLICIT
C   METHOD
C-----
COMMON/THER1/ YHO(31),YO(31),YH(31),YOS(31),YHOV(31),YHOSV(31),
+ YIC(31),YLI(31),XJH(31),RNK(31),WG(31),RO(31),TS(31),T(31),
+ XX(31),DX(31),DY,DT,ROI,YHI,YOI,TI,CP,DS,XLS,XLDS,RT(31)
COMMON/THER4/ TgNEW(31),YONEW(31),RONEW(31),UNEW(31),U(31)
C-----
C -- CORRELATION OF HEAT & MASS TRANSFER
C-----
DO 100 I=1,N
XK=(.04*(T(I)*TI/273.)**.94)/XXI
XST=XX(I)**2.*AD2UL*XK+ROOT
IF (XST .LE. .1) XNU=.0444/XST+3.46-1.34*XST
IF (XST .GT. .1) XNU=.01/XST +3.66
RNK(I)=XNU*XK/3.66
XJH(I)=4.*XNU*AD2UL*XK
IF (I .EQ. 1) GO TO 999
C-----
C** GAS PHASE EQ -- T (X), YO (X), RO (X), U (X)
C-----
CR2=DLT*RO(I)
ELL=EL/T(I)
EHH=EH/T(I)
IF ((T(I) .LE. TCR ).AND.(ELL.LT.100)) THEN
    W1=CL*GRI*(RO(I)*YO(I))**BL/EXP(EL/T(I))
ELSEIF ((T(I) .LE. TCR ).AND.(ELL.GE.100)) THEN
    W1=0.
ENDIF
IF ((T(I) .GT. TCR ).AND.(EHH.LT.100)) THEN
    W1=CH*GRI*(RO(I)*YO(I))**BH/EXP(EH/T(I))
ELSEIF ((T(I) .GT. TCR ).AND.(EHH.GE.100)) THEN
    W1=0.
ENDIF
TCNEW(I)=T(I)+U(I)*DTX/DLT*(T(I-1)-T(I))+(XJH(I)*(TS(I)-T(I))-
+QV*W1)*DT/CR2
XJD=XJH(I)*XLE123
YONEW(I)=YO(I)+U(I)*DTX/DLT*(YO(I-1)-YO(I))+(XJD*(YOS(I)-YO(I))-
+W1/YOI)*DT/CR2
IF (YONEW(I) .LT. 0.) YONEW(I)=0.
RONEW(I)=XPL/GCC/ROL/TI/TCNEW(I)
UNEW(I)=(DLT*(RO(I)-RONEW(I))+DTX*UNEW(I-1)*RONEW(I))/DTX/(2.*
+RONEW(I)-RONEW(I-1))
999 CONTINUE
100 CONTINUE
do 200 i=1,n
t(i)=tGnew(i)
yo(i)=yonew(i)
ro(i)=ronew(i)
200 u(i) =unew(i)
RETURN
END

```

```

SUBROUTINE FULLT (NX,NY,NR,NT,E,RII,RI2,KOU,DTY,X2,X4,KMAX,Z2,Z4,
+ DTZ,DYZ,DZ,XLE,XLE2,KP,RK,SKC,DEF,SK,TIME,TOTAL,BV,tab)
C-----  

C      FULL TRANSIENT EQUATION OF SPECIES AND ENERGY EQ. -  

C      UNIFORM GRID SYSTEM ( CATALYTIC & SUBSTRATE LAYER )  

C-----  

C-----  

DIMENSION A(21),AI(21),YS8(21),YS2(21),DE(21),EM(21),EMI(21),TNEW  

+ (21),YNEW(21),YX(21),YX1(21),A3(21),EM0(21),TNEW2(21),YX3(21),  

+ XL(21),D(21),U(21),TSMAX(31)  

COMMON/THER1/ YHO(31),YO(31),YH(31),YOS(31),YHOV(31),YHOSV(31),  

+ YIC(31),YLI(31),XJH(31),RNK(31),WG(31),R0(31),TS(31),TI(31),  

+ XX(31),DX(31),DY,DT,ROI,YHI,YO,I,CP,DS,XLS,XLDS,RT(31)  

COMMON/THER2/B(21),C(21),B1(21),C1(21),B3(21),C3(21),RR(21),RS(21)  

COMMON/THER3/SN(31),BC(31),YRR(31,21),TS1(31,21),DAM,DAT  

+ ,YOS1(31,21),TS2(31,21),WS(31,21),DEL(31)  

common/ther5/wsmax(31),tsrm(31)  

DO 1000 I=1,NX  

DO 100 J=1,NY  

TNEW(J)=TS1 (I,J)  

YNEW(J)=YOS1(I,J)  

IF (YOS1(I,J) .LE. 0.) THEN  

YS2(J)=0.  

YS8(J)=0.  

ELSE  

YS2(J)=1./YOS1(I,J)**.2  

YS8(J)=YOS1(I,J)**.3  

ENDIF  

100 DE (J)=DT/EXP(E/TS1(I,J))  

DO 200 J = 1,NR  

200 TNEW2 (J)= TS2 (I,J)
C-----  

C **** CONSTANTS FOR CATALYTIC LAYER  

C-----  

DO 300 J=2,NY-1  

A(J) =-1./T(I)-X2-.8*DAM*YS2(J)*DE(J)  

300 AI(J)=-XLE-X2+DAT*YS8(J)*DE(J)*E/TS1(I,J)**2.  

A (1)=1./T(I)+X4*(1.+DY*SH(I))-DT*SH(I)/RII+DAM*DE(I)**.8*YS2(1)  

A(NY)=X4+DAM*DE(NY)**.8*YS2(NY)+1./T(I)  

AI(1)=XLE-X4*(1.-BC(I)**DY)-DAT*DE(I)**YS8(I)**E/TS1(I,J)**2.-BC(I)/  

+ RII**DT  

AI(NY)=-DAT*DE(NY)**YS8(NY)**E/TS1(I,NY)**2.-XLE-DTZ/RK/RI2+X4*(  

+ 1.+DYZ/RK)
C-----  

C **** CONSTANTS FOR SUBSTRATE LAYER  

C-----  

DO 400 J=2,NR-1  

400 A3(J) =-XLE2-Z2  

A3(1) =XLE2+Z4*(1.+RK/DYZ)-RK*DTY/RI2  

A3(NR)=Z4+XLE2
C-----  

C **** FINITE DIFF. METHOD FOR CATALYTIC LAYER (SPECIES EQ.)  

C-----  

ITER=0  

ITER1=0  

666 CONTINUE  

IF ((ITER .EQ. 20) .OR. (ITER1 .EQ. 20)) THEN  

WRITE(*,*)' KOU',KOU,' I (CAT) ** ',I  

ENDIF  

DO 500 J=2,NY-1  

EM(J)=-B(J)*YOS1(I,J-1)+YOS1(I,J)*(X2-1./T(I)+DAM*YS2(J)*DE(J)**.2

```

```

      +-E/TSI(I,J))-YOSI(I,J+1)*C(J)+DE(J)*DAM*E*YS8(J)/TSI(I,J)**2. *
500 +TNEW(J)
      EM(I)=YOSI(I,I)/T(I)+(X4*DY-DT/R11)*SH(I)*YO(I)-DAM*DE(I)*YS8(I)*
      + (.2-E/TSI(I,I)*(1.-TNEW(I)/TSI(I,I)))
      EM(NY)=-DAM*DE(NY)*YS8(NY)*(.2-E/TSI(I,NY)*(1.-TNEW(NY)/TSI(I,NY))
      +))+YOSI(I,NY)/T(I)
      CALL MATRLU ( A , B , C , XL , D , U , NY)
      CALL SOLVER (XL , D , U , EM , YX , NY)
C-----
C **** FINITE DIFF. METHOD FOR CATALYTIC LAYER (ENERGY EQ.)
C-----
      DO 600 J=2,NY-1
      EMI(J)=-BI(J)*TSI(I,J-1)+TSI(I,J)*(X2-XLE)-TSI(I,J+1)*C1(J)-DE(J)*
600 +DAT*(YS8(J)*(1.2-E/TSI(I,J))+.8*YX(J)*YS2(J))
      EMI(I)=TSI(I,I)*XLE+(X4*DY-DT/R11)*BC(I)*T(I)+DAT*DE(I)*(YS8(I)*
      +(.2-E/TSI(I,I))+.8*YX(I)*YS2(I))
      EMI(NY)=DAT*DE(NY)*(YS8(NY)*(1.2-E/TSI(I,NY))+.8*YX(NY)*YS2(NY))
      +XLE*TSI(I,NY)+TNEW2(2)*(X4*DY+DT/R12)/RK/DZ
      CALL MATRLU (A1 , BI , CI , XL , D , U , NY)
      CALL SOLVER (XL , D , U , EMI , YX1 , NY)
C-----
      ERR1=0.
      ERR2=0.
      DO 700 K=1,NY
      ER1 =ABS( YX(K)-YNEW(K))
      ER2 =ABS(YXI(K)-TNEW(K))
      ERR1=AMAX1(ER1,ERR1)
      ERR2=AMAX1(ER2,ERR2)
      YNEW(K)=YX (K)
700 TNEW(K)=YXI(K)
      IF ((ERR1.GT. 1.E-3).OR.(ERR2.GT. 1.E-3)) THEN
      ITER=ITER+1
      GO TO 666
      ENDIF
C-----
C **** FINITE DIFF. METHOD FOR SUBSTRATE LAYER (ENERGY EQ.)
C-----
      DO 800 J=2,NR-1
800 EM3(J)=-B3(J)*TS2(I,J-1)+TS2(I,J)*(Z2-XLE2)-TS2(I,J+1)*C3(J)
      EM3(I)=TS2(I,I)*XLE2+(Z4*DZ-DT/R12)*RK/DY*TNEW(NY-1)
      EM3(NR)=XLE2*TS2(I,NR)
      CALL MATRLU (A3 , B3 , C3 , XL , D , U , NR)
      CALL SOLVER (XL , D , U , EM3 , YX3 , NR)
      DO 900 K=1,NR
900 TNEW2(K)=YX3(K)
C-----
C **** CHECK TEMP. GRADIENTS AT THE INTERFACE
C-----
      ERI=ABS(TNEW(NY)-TNEW2(1))
      IF (ERI.GT. 5.E-2) THEN
      ITER1=ITER1+1
      ITER =0
      GO TO 666
      ENDIF
      999 CONTINUE
C-----
C--- MAX SOLID REACTION RATE
C-----
      wmax=0.
      DO 910 J=1,NY

```

```

WS(I,J)= BV*YNEW(J)**.8/EXP(E/TNEW(J))
REF2= WS (I,J)
WMAX= AMAX1 (REF2,WMAX)
TS1 (I,J)= TNEW(J)
910 YOS1(I,J)= YNEW(J)
wsmax(i)=wmax
C-----
C--- MAX SOLID TEMP IN RADIAL POSITION
C-----
call maxx (ny,tnew,km)
TSRM(I)=RT(KM)
tsmax(i)=tnew(km)
C
DO 920 J=1,NR
920 TS2 (I,J)= TNEW2(J)
TS (I)=TS1 (I,1)
YOS(I)=YOS1(I,1)
1000 CONTINUE
C-----
C--- END OF FINITE DIFFERENCE
C-----
C--- MAX GAS and solid TEMP IN AXIAL POSITION
C-----
call maxx (nx,t,L)
call maxx (nx,tsmax,L1)
C-----
C--- MAX SOLID and gas reaction rate IN AXIAL POSITION
C-----
call maxx (nx,wsmax,m)
call maxx (nx,wg,m1)
RETURN
END

```

```

subroutine maxx (n,yy,LL)
C-----
C*** to find the max. value
C-----
dimension yy(31)
gre=yy(1)
LL=1
do 100 i=1,n-1
if (yy(i+1) .gt. gre) then
gre=yy(i+1)
ll=i+1
endif
100 continue
return
end

```

```

SUBROUTINE MATRLU (A,B,C,XL,D,U,N)
C-----
C-- MATRIX SOLVER FOR LU-METHOD
C-----
DIMENSION A(21),B(21),C(21),XL(21),D(21),U(21)
D(1)=A(1)
U(1)=C(1)
DO 20 I=2,N-1
XL(I)=B(I)/D(I-1)
D(I)=A(I)-XL(I)*U(I-1)
U(I)=C(I)
20 CONTINUE
XL(N)=B(N)/D(N-1)
D(N)=A(N)-XL(N)*U(N-1)
RETURN
END

```

```

SUBROUTINE SOLVER (XL,D,U,Q,X,N)
DIMENSION XL(21),Q(21),D(21),U(21),X(21),Y(21)
Y(1)=Q(1)
DO 20 I=2,N
20 Y(I)=Q(I)-XL(I)*Y(I-1)
X(N)=Y(N)/D(N)
IF (X(N) .LT. 1.E-5) X(N)=0.
DO 30 J=N-1,1,-1
X(J)=(Y(J)-U(J)*X(J+1))/D(J)
IF (X(J) .LT. 1.E-5) X(J)=0.
30 CONTINUE
RETURN
END

```

```

SUBROUTINE QUASI (N,Q,DMASS,GRI,CL,BL,EL,CH,BH,EH,TCR,XPHI,XLE123,
+ KOU,XPI,ROOT,AD2UL,XKI)
C -----
C-- QUASI-STEADY GAS-PHASE EQUATION
C -----
C      DIMENSION XKY(4),XKZ(4),XKT(4)
COMMON/THERL/ YHO(31),YO(31),YH(31),YOS(31),YHOV(31),YHOSV(31),
+ YIC(31),YLI(31),XJH(31),RNK(31),WG(31),RO(31),TS(31),T(31),
+ XX(31),DX(31),DY,DT,ROI,YHI,YOI,TI,CP,DS,XLS,XLDS,RT(31)
C -----
C -- CORRELATION OF HEAT & MASS TRANSFER
C -----
      DO 100 I=1,N
      XK=(.04*(T(I)*TI/273.)**.94)/XKI
      XST=XX(I)*2.*AD2UL*XK*ROOT
      IF (XST .LE. .1) XNU=.0444/XST+3.46-1.34*XST
      IF (XST .GT. .1) XNU=.011/XST +3.66
      RNK(I)=XNU*XK/3.66
      XJH(I)=4.*XNU*AD2UL*XK
C
      IF (I .EQ. N) GO TO 999
      M=1
      DO 120 L=1,4
      ELL=EL/TT
      EHH=EH/TT
      IF (TT .LE. TCR ) THEN
      W1=CL*GRI*(ROI(I)*Y02)**BL/EXP(EL/TT)
      ENDIF
      IF (TT .GT. TCR ) THEN
      W1=CH*GRI*(ROI(I)*Y02)**BH/EXP(EH/TT)
      ENDIF
      XKY(L)=(-XJH(I)*XLE123*(Y02-YOS(I))-W1/Y01)/DMASS
      XKZ(L)=(-XJH(I)*XLE223*(YHO2-YHOSV(I))+W1/YHI**36./32.)/DMASS
      XKT(L)=(-XJH(I)*(TT-TS(I))+Q*W1)/DMASS
120   CONTINUE
      YO(I+1) =YO(I) +DX(I)*(XKY(1)+2.*XKY(2)+2.*XKY(3)+XKY(4))/6.
      IF (YO(I+1) .LT. 0.) YO(I+1)=0.
      YHO(I+1)=YHO(I)+DX(I)*(XKZ(1)+2.*XKZ(2)+2.*XKZ(3)+XKZ(4))/6.
      IF (YHO(I+1) .LT. 0.) YHO(I+1)=0.
      T (I+1) =T(I) +DX(I)*(XKT(1)+2.*XKT(2)+2.*XKT(3)+XKT(4))/6.
      IF (T(I+1) .LT. 1.) T(I+1)=1.
      YH(I+1)=1.-(1.-YO(I+1))/XPHI
100   ROI(I+1)=1./T(I+1)
999   CONTINUE
      RETURN
END
C
SUBROUTINE ROUTIN (I,M,YHO2,Y02,TT,XKY,XKZ,XKT)
DIMENSION XKY(4),XKZ(4),XKT(4)
COMMON/THERL/ YHO(31),YO(31),YH(31),YOS(31),YHOV(31),YHOSV(31),
+ YIC(31),YLI(31),XJH(31),RNK(31),WG(31),RO(31),TS(31),T(31),
+ XX(31),DX(31),DY,DT,ROI,YHI,YOI,TI,CP,DS,XLS,XLDS,RT(31)
      IF (M .NE. 1) GO TO 102
      YHO2=YHO(I)
      Y02 =YO(I)
      TT =T(I)
      M =M+1
      GO TO 119
102   CONTINUE
      IF (M .NE. 2) GO TO 103

```

```
YHO2=YHO(I)+DX(I)*XKZ(1)/2.  
YO2 =YO(I) +DX(I)*XKY(1)/2.  
TT =T(I) +DX(I)*XKT(1)/2.  
M =M+1  
GO TO 119  
103 CONTINUE  
IF (M .NE. 3) GO TO 104  
YHO2=YHO(I)+DX(I)*XKZ(2)/2.  
YO2 =YO(I) +DX(I)*XKY(2)/2.  
TT =T(I) +DX(I)*XKT(2)/2.  
M =M+1  
GO TO 119  
104 CONTINUE  
YHO2=YHO(I)+DX(I)*XKZ(3)  
YO2 =YO(I) +DX(I)*XKY(3)  
TT =T(I) +DX(I)*XKT(3)  
119 CONTINUE  
IF (YHO2 .LE. 0.) YHO2=0.  
IF (YO2 .LE. 0.) YO2 =0.  
IF (TT .LE. 0.) TT =0.  
RETURN  
END
```

```

SUBROUTINE SHOOT(NX,NY,NR,NT,E,H2,RII,RI2,KOU,ROC1,ROC2,KMAX,KP,
+ BV,AP,KST,DTS,total,time)
C-----
C      TO SOLVE ENERGY INTEGRAL EQ. BY SHOOTING METHOD
C      NONUNIFORM YOS ,TS ,NON-UNIFORM GRID
C -----
C      DIMENSION TTSUM(31),TSR(21),YSR(21),YT(21),GJ(21),tsmax(31)
COMMON/THERL/YHO(31),YO(31),YH(31),YOS(31),YHOV(31),YHOSV(31),
+ YIC(31),YLI(31),XJH(31),RNK(31),WG(31),RO(31),TS(31),T(31),
+ XX(31),DX(31),DY,DT,ROI,YHI,YOI,TI,CF,DS,XLS,XLDS,RT(31)
COMMON/THER3/SH(31),BC(31),YRR(31,21),TSI(31,21),DAM,DAT
+ ,YOSI(31,21),TS2(31,21),WS(31,21),DEL(31)
common/ther5/wsmax(31),tsrm(31)
DO 1000 I=1,NX
ITER=0
C -----
C      TRANSFORMATION OF COORDINATE
C -----
IF (KOU .EQ.KST) THEN
DO 100 J=1,NY
YRR(I,J)=RT(J)
GJ(J)=I.
YT(J)=YOSI(I,J)**.8/EXP(E/TSI(I,J))
100 TSR(J)=TSI(I,J)
CALL TRPZ (I,SUMY,DY, YT,NY,RII,GJ)
CALL TRPZ (I,SUMT,DY,TSR,NY,RII,GJ)
TTSUM(I)=DTS*RNK(I)*(T(I)-TSR(I))+H2*SUMY+ROC1*SUMT+ROC2*TSR(NY)
ENDIF
BB=L./SQRT(1.-DEL(I))
BB2=BB*BB
BBC=(BB+L.)/(BB-L.)
DO 500 J=2,NY
IF (YOSI(I,J) .EQ. 0.) THEN
CHEC=DY
ELSE
CHEC=YOSI(I,J)/YOSI(I,I)
ENDIF
IF (CHEC .LE. .1)THEN
DELT=(BB+L.-(BB-L.)*BBC***(1.-RT(J)))/(1.+BBC***(1.-RT(J)))
GO TO 555
ELSE
DELT=L.
ENDIF
500 CONTINUE
555 CONTINUE
IF ((DELT .LT. DEL(I)).AND.(DELT .GE. DY)) DEL(I)=DELT
IF ( DELT .LT. DY) DEL(I)=DY
BB=L./SQRT(1.-DEL(I))
BB2=BB*BB
BBC=(BB+L.)/(BB-L.)
DO 200 J=1,NY
YC=BBC***(1.-RT(J))
YRR(I,J)=(BB+L.-(BB-L.)*YC)/(1.+YC)
200 GJ(J)=2.*BB/(BB2-(1.-YRR(I,J))**2.)/ALOG(BBC)
TSS=TSI (I,I)**L1
YSS=YO(I)**.95
TSGT=0.
TSLT=0.
C -----
C      ITERATION ON ENERGY INTEGRAL EQUATION

```

```

C-----
666 CONTINUE
  IF (ITER.EQ.30) GO TO 999
  YSGT=0.
  YSLT=0.
  ITER=ITER+1
  ITER1=0
C-----
C   ITERATION ON SPECIES EQ. (SHOOTING METHOD)
C-----
777 CONTINUE
  ITER1=ITER1+1
  IF (ITER1 .GT. 30) GO TO 888
  BP=TSS-AP*YSS
  YOP=SH(I)*(YSS-YO(I))/GJ(I)
  CALL RUNGE (I,E,YSR,AP,BP,YSS,YOP,YP,NY,DY,BB,BB2,BB3,RII,GJ,KOU)
  IF (ABS(YP).LT. .01) GO TO 888
  IF ((YP.LT. 0.).AND.(ITER1 .EQ.1)) THEN
    YSS=YO(I)*.99
    GO TO 777
  ENDIF
  IF (YP.GT.0.) THEN
    YSGT=YSS
    ELSE
    YSLT=YSS
  ENDIF
  YSS=(YSGT+YSLT)/2.
  GO TO 777
888 CONTINUE
C-----
C   END OF SPECIES EQUATION
C-----
DO 300 J=1,NY
300 TSR(J)=TSS-AP*(YSR(I)-YSR(J))
  CALL TRPZ (I,SUMT,DY,TSR,NY,RII,GJ)
  TNSUM=ROC1*SUMT+ROC2*TSR(NY)
  IF (ABS(TNSUM-TTsum(I)).LE. 1.E-2) GO TO 999
  CORR=ABS(TNSUM-TTsum(I))
  IF (CORR .LT. FIN) THEN
    FIN=CORR
    YFIN=YSS
    TFTN=TSS
  ENDIF
  IF ((ITER.EQ.1) .AND. (TNSUM .LT. TTsum(I))) THEN
    TSS=TSS*2
    GO TO 666
  ENDIF
  IF (TNSUM .GT. TTsum(I)) THEN
    TSGT=TSS
    ELSE
    TSLT=TSS
  ENDIF
  IF ((TSLT.EQ.0.).OR.(TSGT.EQ.0.)) THEN
    TNEW=TSS*.95
    TNEW=(TSLT+TSGT)/2.
  ENDIF
  IF (ABS(TNEW-TSS) .LE. 1.E-3) GO TO 999
  IF (TNEW .GT. TSS) YSS=YSR(I)
  IF (TNEW .LT. TSS) YSS=YOS(I,I)*.9
  TSS=TNEW

```

```

      GO TO 666
999 CONTINUE
      wmax=0.
      DO 400 J=1,NY
      WS(I,J)= BV*YSR(J)**.8/EXP(E/TSR(J))
      REF2= WS (I,J)
      WMAX= AMAX1 (REF2,WMAX)
      TSI (I,J)=TSR(J)
      YOS(I,J)=YSR(J)
400   YT(J) =YOS(I,J)**.8/EXP(E/TSI(I,J))
      do 410 j=1,nr
410   ts2(i,j)=tsr(ny)
      CALL TRPZ (I,SUMY,DY, YT,NY,RII,GJ)
      TTSUM(I)=DTS*RNK(I)*(T(I)-TSR(I))+H2*SUMY+TTSUM(I)
      TS (I)=TSI(I,I)
      YOS(I)=YOS(I,I)
      wsmax(i)=wmax
C-----
C MAX SOLID TEMP IN RADIAL POSITION
C-----
      call maxx (ny,tsr,km)
      TSRM(I)=RT(KM)
      tsmax(i)=tsr(km)
1000 CONTINUE
C-----
C END OF ENERGY INTEGRAL EQUATION
C-----
C MAX GAS and solid TEMP IN AXIAL POSITION
C-----
      call maxx (nx,tsmax,L1)
      call maxx (nx,tsmax,L1)
C-----
C MAX SOLID and gas reaction rate IN AXIAL POSITION
C-----
      call maxx (nx,wsmax,m)
      call maxx (nx,wg,m)
      RETURN
      END
C-----
C INTEGRATION
C-----
      SUBROUTINE TRPZ (I,SUM,DY,FUN,N,RII,GJ)
      DIMENSION FUN(21),GJ(21)
      COMMON/THER1/SH(31),BC(31),YRR(31,21),TSI(31,21),DAM,DAT
      + ,YOS(31,21),TS2(31,21),WS(31,21),DEL(31)
      SUM=FUN(1)*RII/2./GJ(1)
      DO 100 J=2,N-1
      R=(RII+YRR(I,J))/GJ(J)
100   SUM=SUM+FUN(J)*R
      SUM=(SUM+FUN(N)*(RII+YRR(I,N))/2./GJ(N))*DY
      RETURN
      END
C-----
C RUNGE - KUTTA METHOD FOR SPECIES EQ.
C-----
      SUBROUTINE RUNGE(I,E,YSR,AP,BP,YSS,YOP,YP,NY,DR,BB,BB2,BB3,RII,GJ
      +,KOU)
      DIMENSION YSR(21),GJ(21)
      COMMON/THER1/ YHO(31),YO(31),YH(31),YOS(31),YHOV(31),YHOSV(31),
      + YIC(31),YLJ(31),XJH(31),RNK(31),WG(31),RO(31),TS(31),T(31),

```

```

+ XX(31),DX(31),DY,DT,ROI,YHI,YOI,TI,CP,DS,XLS,XLDS,RT(31)
COMMON/THER3/SH(31),BC(31),YRR(31,21),TS1(31,21),DAM,DAT
+ ,YOSI(31,21),TS2(31,21),WS(31,21),DEL(31)
F(Z)=Z
G(A,B,Y,Z,TT)=(DAM*Y**.8/EXP(E/TT)-B*Z)/A/A
C-----
YP=YOP
YOSS=YSS
YSR(1)=YSS
DO 1000 J=1,NY-1
RB=DR*FLOAT(J-1)
C1=G(J,J)
C2=C1*(1.-(YRR(I,J)+RI1))-2.*((1.-YRR(I,J))/(BB2-(1.-YRR(I,J))**2.))
TT=AP*YOSS+BP
IF (YOSS.LT.0.) GO TO 999
Y1=F(YP)*DR
Z1=G(C1,C2,YOSS,YP,TT)*DR
RB1=RB-DR/2.
YC1=BB3**((1.-RB1)
RT1=(BB+1.-(BB-1.)*YC1)/(1.+YC1)
C3=2.*BB/(BB2-(1.-RT1)**2.1./ ALOG(BB3)
C4=C3*(1.-(RT1+RI1))-2.*((1.-RT1)/(BB2-(1.-RT1))**2.))
CH1=YOSS+Y1/2.
TT=AP*CH1+BP
IF (CH1.LT.0.) GO TO 999
YZ=YP+Z1/2.
Y2=F(YZ)*DR
Z2=G(C3,C4,CH1,YZ,TT)*DR
CH2=YOSS+Y2/2.
TT=AP*CH2+BP
IF (CH2.LT. 0.) GO TO 999
YZ=YP+Z2/2.
Y3=F(YZ)*DR
Z3=G(C3,C4,CH2,YZ,TT)*DR
CH3=YOSS+Y3
TT=AP*CH3+BP
IF (CH3 .LT. 0.) GO TO 999
YZ=YP+Z3
Y4=F(YZ)*DR
Z4=G(C3,C4,CH3,YZ,TT)*DR
YOLD=YOSS
YOSS=YOSS+(Y1+2.*Y2+2.*Y3+Y4)/6.
IF (YOSS .LT. 0.) GO TO 999
IF (YOSS.GT.YOLD) THEN
YP=1.
GO TO 999
ENDIF
YP= YP+(Z1+2.*Z2+2.*Z3+Z4)/6.
YSR(J+1)=YOSS
1000 CONTINUE
GO TO 777
999 CONTINUE
DO 888 K=J+1,NY
888 YSR(K)=0.
777 CONTINUE
RETURN
END

```

TABLE 1

## Estimate of Transient Time Scales in a Monolithic Reactor

Time	Definition	Estimated Magnitude
Gas residence time in reactor	$(\frac{L^*}{u_{ref}^*})(\frac{A^*_T}{A_T})$	1 - 15 msec
Heat/mass transfer time between gas and solid surface in channel	$\frac{d^{*2}}{Nu_\infty^* \pi 4 \alpha_g^*(0,0)}$	0.5- 7.5 msec $d^* \leq 3.6$ mm
Mass diffusion time in porous catalytic layer	$\frac{\epsilon h_c^{*2}}{D_e^*(0,0)}$	0.03-0.3 msec $d_s^* \leq 0.2$ mm
Heat conduction time in porous catalytic layer	$\frac{h_c^{*2}}{\alpha_c^*}$	0.1- 4 msec
Heat conduction time in substrate layer	$\frac{h_s^{*2}}{\alpha_s^*}$	0.4- 21 msec
Homogeneous chemical reaction time		Same order as gas residence time

(continued on next page)

TABLE 1 (continued)

Time	Definition	Estimated Magnitude
Heterogeneous chemical reaction time		Same order as solid heat-up time
Solid heat-up time	$\frac{2 \int_{r_d}^{r_s} \rho^* C^* r^* dr^*}{N_u_\infty \lambda_g^*(0,0)}$	0.5- 20 sec

TABLE 2

**List of Time Scales and Nondimensional  
Parameters in Case 1**

Name	Symbol	Value	Unit
Mass diffusion time in catalytic layer	$\tau_m^*$	$4.3 \times 10^{-5}$	sec
Heat conduction time in catalytic layer	$\tau_t^*$	$4.3 \times 10^{-5}$	sec
Heat conduction time in substrate layer	$\tau_s^*$	$2. \times 10^{-4}$	sec
Gas residence time	$\tau_r^*$	$3. \times 10^{-3}$	sec
Solid heat-up time	$\tau_{HT}^*$	$2. \times 10^{-2}$	sec
Damkohler number of gas	$D_{am}$	0.04	
Damkohler number of solid	$D_{at}$	0.04	
Sherwood number	$Sh$	2.36 ~ 0.27	
Biot number	$B_c$	0.97 ~ 0.11	

TABLE 3

## Parametric Studies

Parameter	Case 1	Case 2	Case 3	Case 4	Case 5
$\beta^*$ (kg-Pt/m <sup>3</sup> )	1.8	0.18	18.	1.8	1.8
$C_p^*$ (cal/kg/°K)	1850.	1850.	1850.	1310.	1850.
$T_{ab}^*$ (°K)	1372.	1372.	1372.	2200.	1372
$\tau_{HT}^*$ (sec)	0.02	0.02	0.02	0.02	2.
$\phi$	8.	8.	8.	4.	8.
D <sub>am</sub>	0.04	0.004	0.4	0.04	0.04
D <sub>at</sub>	0.04	0.004	0.4	0.08	0.04
q <sub>c</sub>	5.	5.	5.	7.	5.
Y <sub>g</sub> (0,0)	0.5	0.5	0.5	0.66	0.5
D <sub>am</sub> '	0.08	0.008	0.8	0.06	0.08
D <sub>at</sub> '	0.2	0.02	2.	0.56	0.2
Max. Sh	2.36	2.36	2.36	2.8	2.36
Min. Sh	0.27	0.27	0.27	0.27	0.27
Max. B <sub>c</sub>	0.97	0.97	0.97	1.15	0.97
Min. B <sub>c</sub>	0.11	0.11	0.11	0.11	0.11

TABLE 4

## List of Property Values in Case 1

Name	Symbol	Value	Unit
Diameter of cell	$d^*$	$10^{-3}$	m
Length of cell	$L^*$	$5 \times 10^{-2}$	m
Porosity of catalytic layer	$\epsilon$	0.5	
Thickness of catalytic layer	$h_c^*$	$3.3 \times 10^{-3}$	m
Thickness of substrate layer	$h_s^*$	$6.7 \times 10^{-3}$	m
Open area ratio	$A^*/A_s^*$	2.	
Density of catalytic layer	$\rho_c^*$	13.	$\text{kg}/\text{m}^3$
Density of substrate layer	$\rho_s^*$	183.	$\text{kg}/\text{m}^3$
Specific heat of catalytic layer	$C_c^*$	180.	$\text{cal}/\text{kg}/{}^\circ\text{K}$
Specific heat of substrate layer	$C_s^*$	180.	$\text{cal}/\text{kg}/{}^\circ\text{K}$
Heat conductivity of catalytic layer	$\lambda_c^*$	0.069	$\text{cal}/\text{m}/\text{s}/{}^\circ\text{K}$
Heat conductivity of substrate layer	$\lambda_s^*$	0.69	$\text{cal}/\text{m}/\text{s}/{}^\circ\text{K}$
Effective diffusivity of oxygen in catalytic layer	$D_e^*(0,0)$	$1.66 \times 10^{-5}$	$\text{m}^2/\text{sec}$

TABLE 5

## List of Operating Parameters in Case 1

Name	Symbol	Value	Unit
Catalyst loading	$\beta^*$	1.8	$\text{kg/m}^3$
Inlet pressure	$P^*(0,0)$	9.	atm
Inlet Temperature	$T^*(0,0)$	400.	$^{\circ}\text{K}$
Inlet velocity	$u^*(0,0)$	10.	m/sec
Inlet mass ratio		1.	
Hydrogen/Oxygen equivalence ratio	$\phi$	8.	
Adiabatic flame temperature	$T_{ab}^*$	1376	$^{\circ}\text{K}$

TABLE A.1

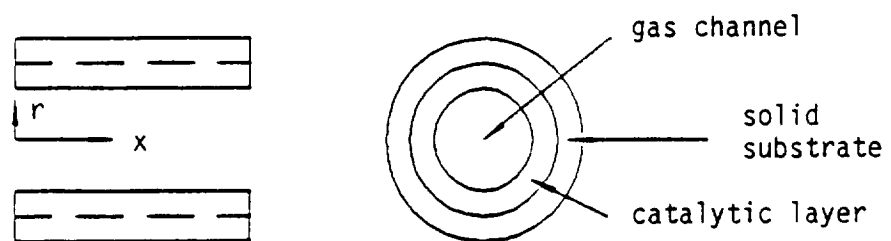
## Parameters for Two Sets of Gas-Phase Reaction Rates

Parameter	Symbol	Value	Unit
Rate Constant	$K_L^*$	$4 \times 10^8$	$\text{atm}^{1.5} (\text{kg/m}^3)/\text{sec}$
	$K_H^*$	$9 \times 10^6$	$1/\text{atm/sec}$
Exponent of P	$a_L$	-1.5	
	$a_H$	1	
Exponent of $\rho_o^*$	$b_L$	0.1	
	$b_H$	1.	
Activation Energy	$E_L^*$	$7.9 \times 10^4$	cal/mole
	$E_H^*$	$1.9 \times 10^4$	cal/mole

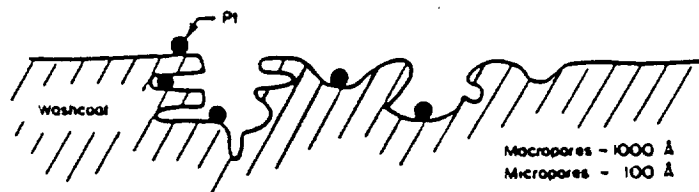
Note :

Subscript L and H denote the parameter used for the gas-phase reaction rate at  $T^* \leq T_{cr}^*$  and  $T^* \geq T_{cr}^*$ , respectively. The critical temperature in this study is  $T_{cr}^* = 1200^\circ\text{K}$ . The general expression for the gas-phase reaction rate is :

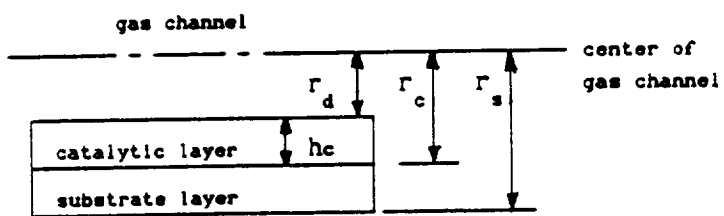
$$W^* = K^* P^{*a} \rho_o^{*b} \exp(-E^*/RT^*) \quad [\text{kg-O}_2/\text{m}^3/\text{sec}]$$



(a) Physical model for a tubular reactor



(b) Illustration of catalytic layer structure



(c) Definition of dimensions

Figure 1 : Monolithic reactor model description

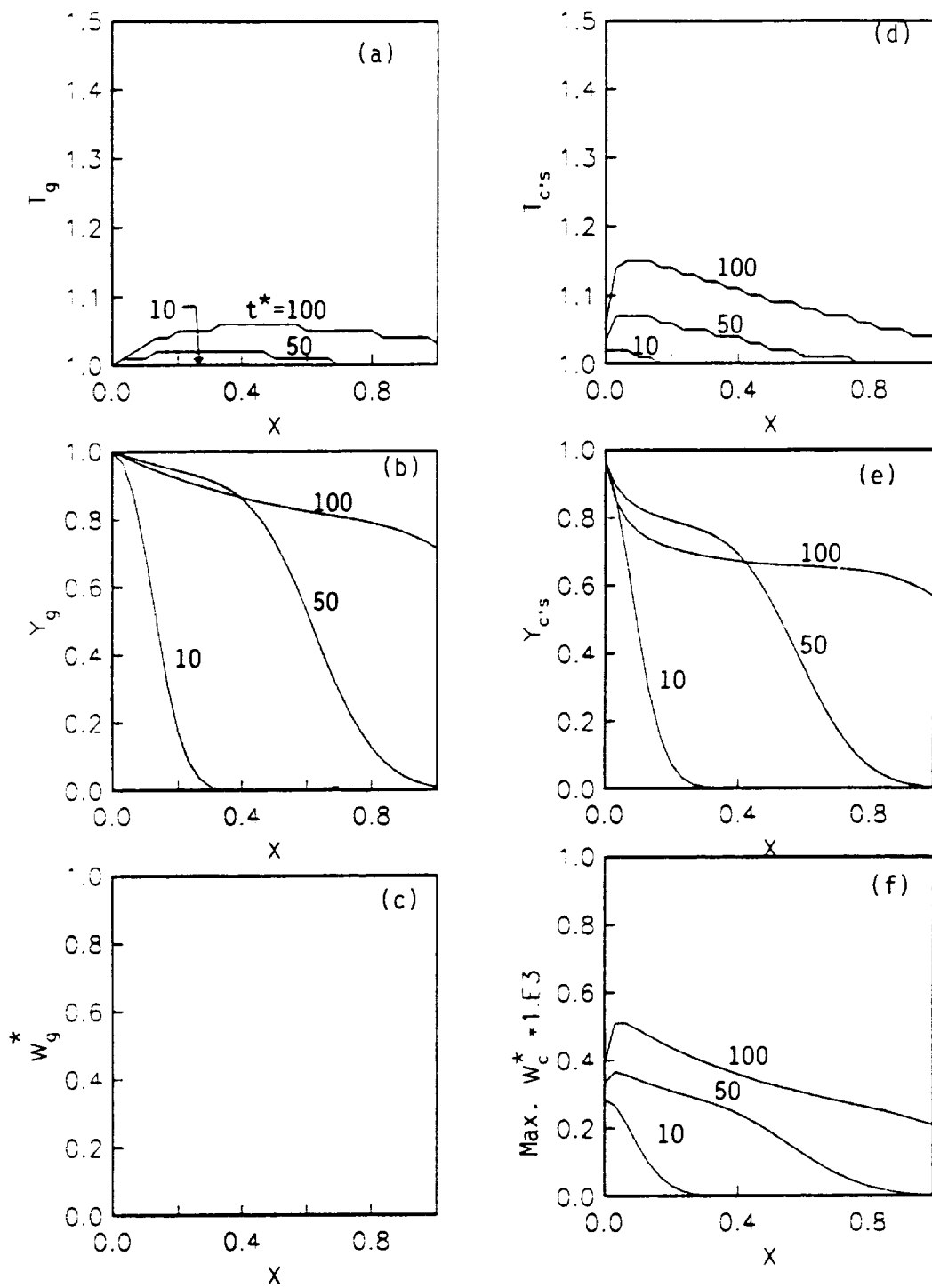


Figure 2 : Transient profiles for Case 1 at  $t^* = 10, 50, 100$   $\tau_m^*$   
 $(\beta^* = 1.8 \text{ kg-pt/m}^3, L^* = 5 \text{ cm}, \phi = 8)$

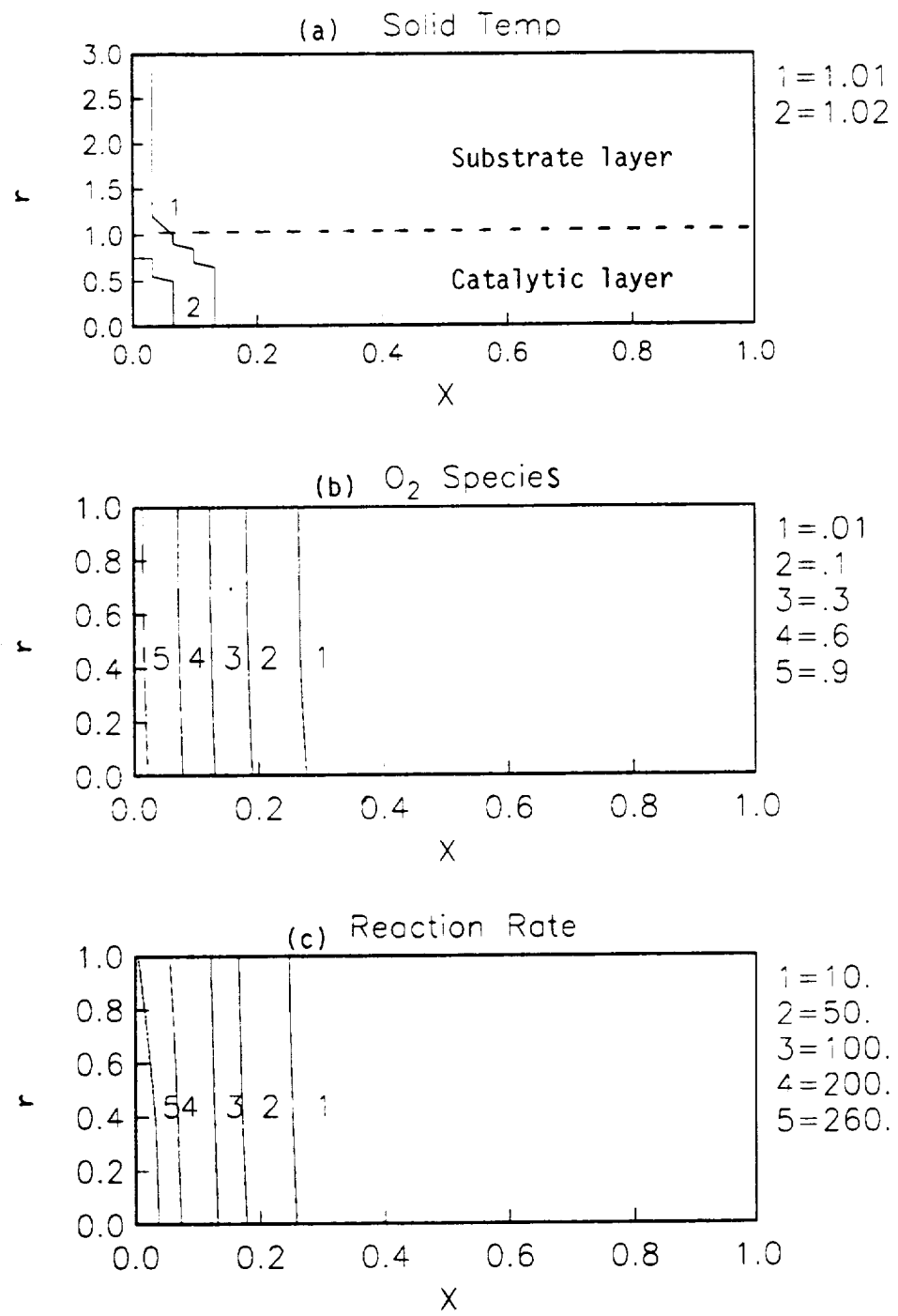


Figure 3 : Solid contours for Case 1 at  $t^* = 10 \tau_m^*$

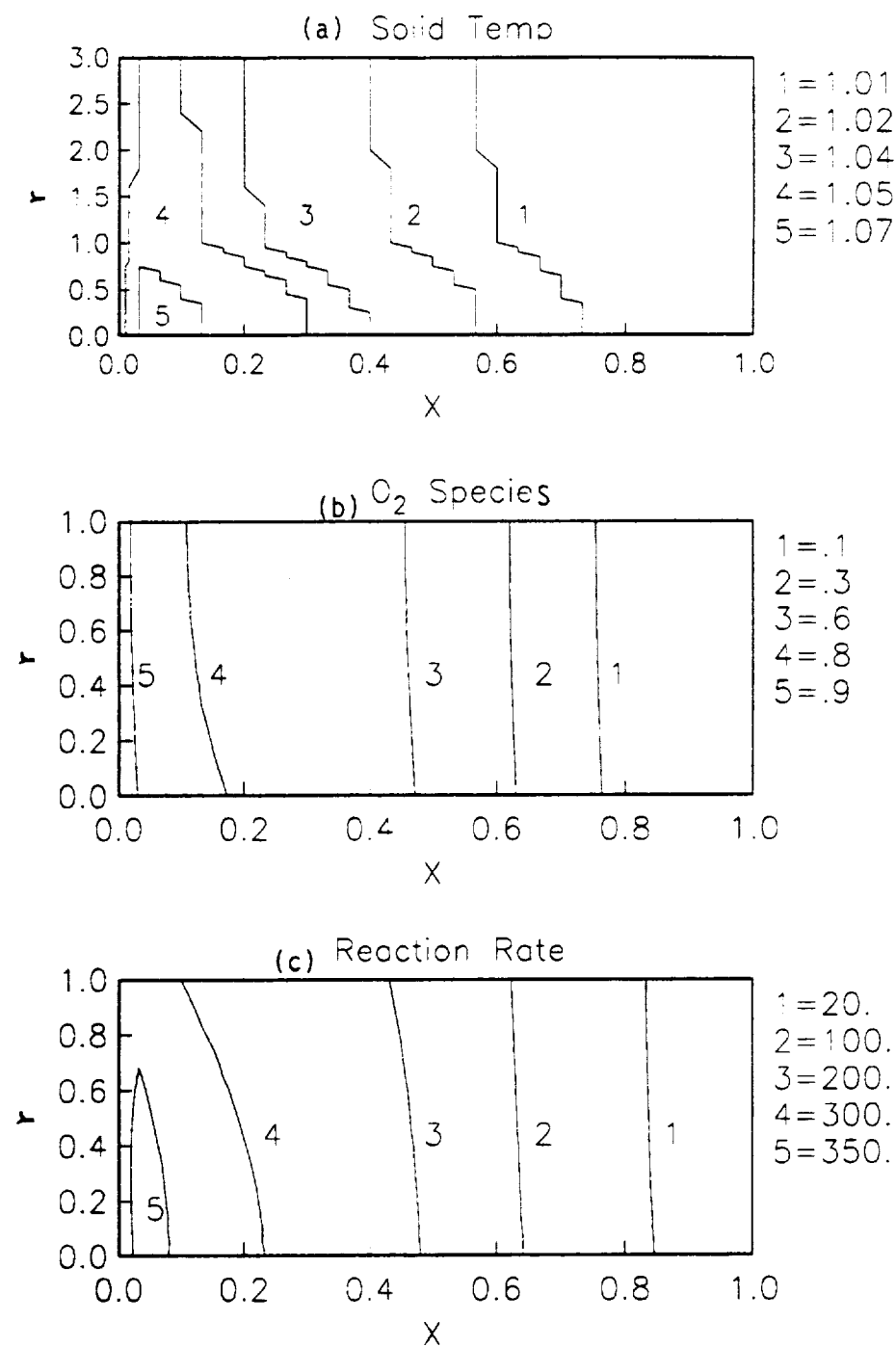


Figure 4 : Solid contours for Case 1 at  $t^* = 50 \tau_m^*$

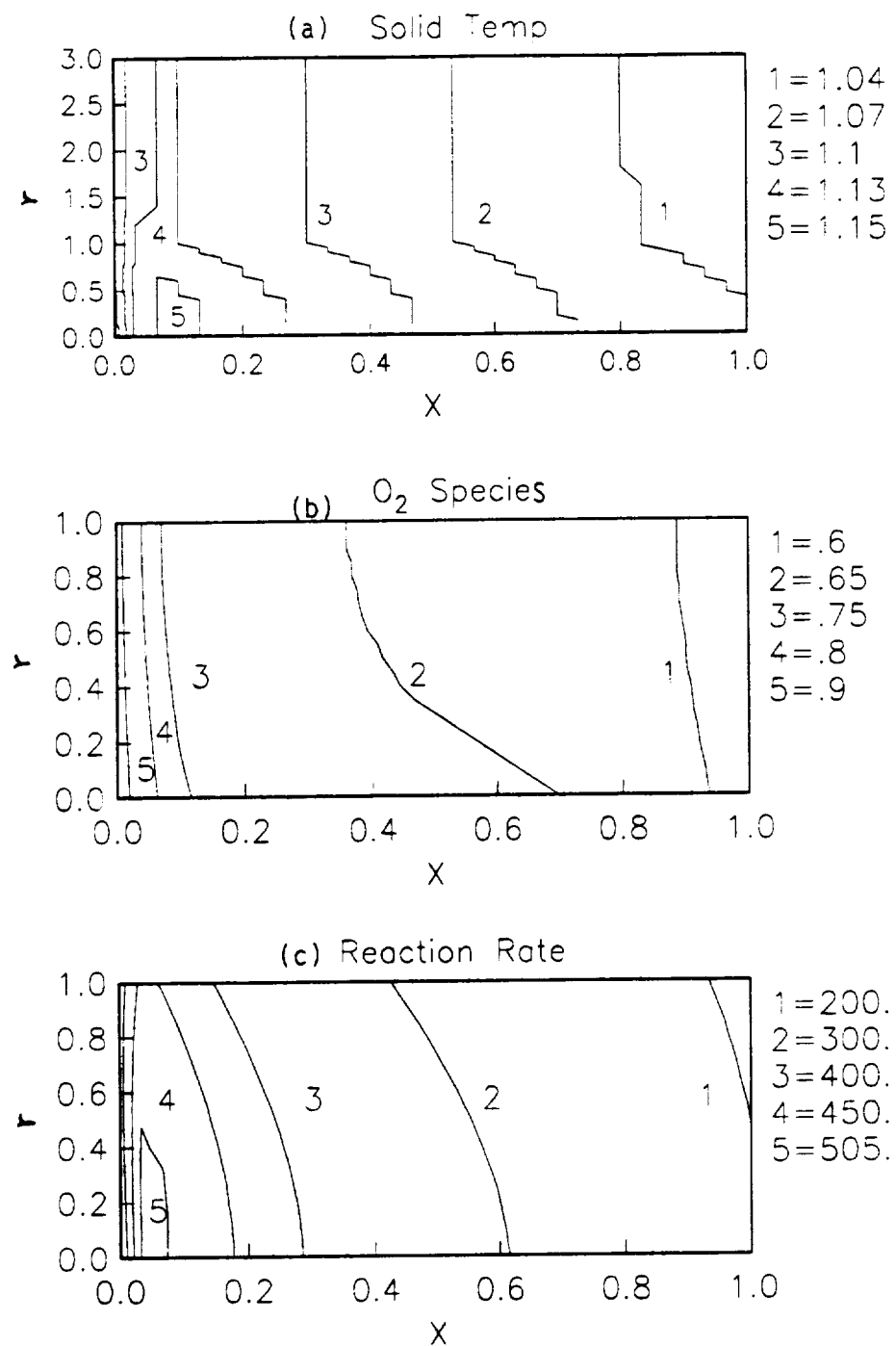


Figure 5 : Solid contours for Case 1 at  $t^* = 100 \tau_m^*$

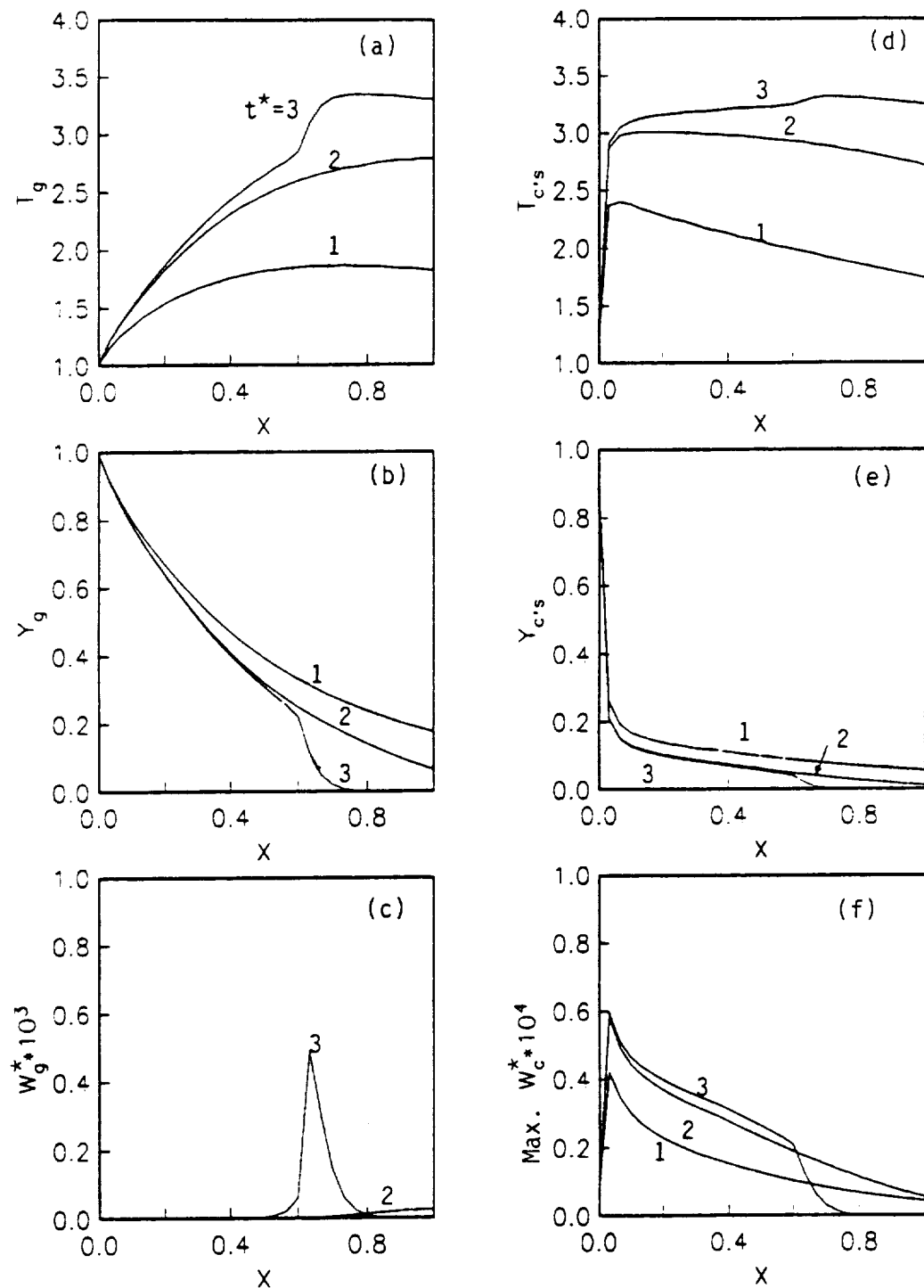


Figure 6 : Transient profiles for Case 1 at  $t^* = 1, 2, 3 \tau_m^{\text{HT}}$   
 $(1 \tau_m^{\text{HT}} = 500 \tau_m^{\text{HT}})$

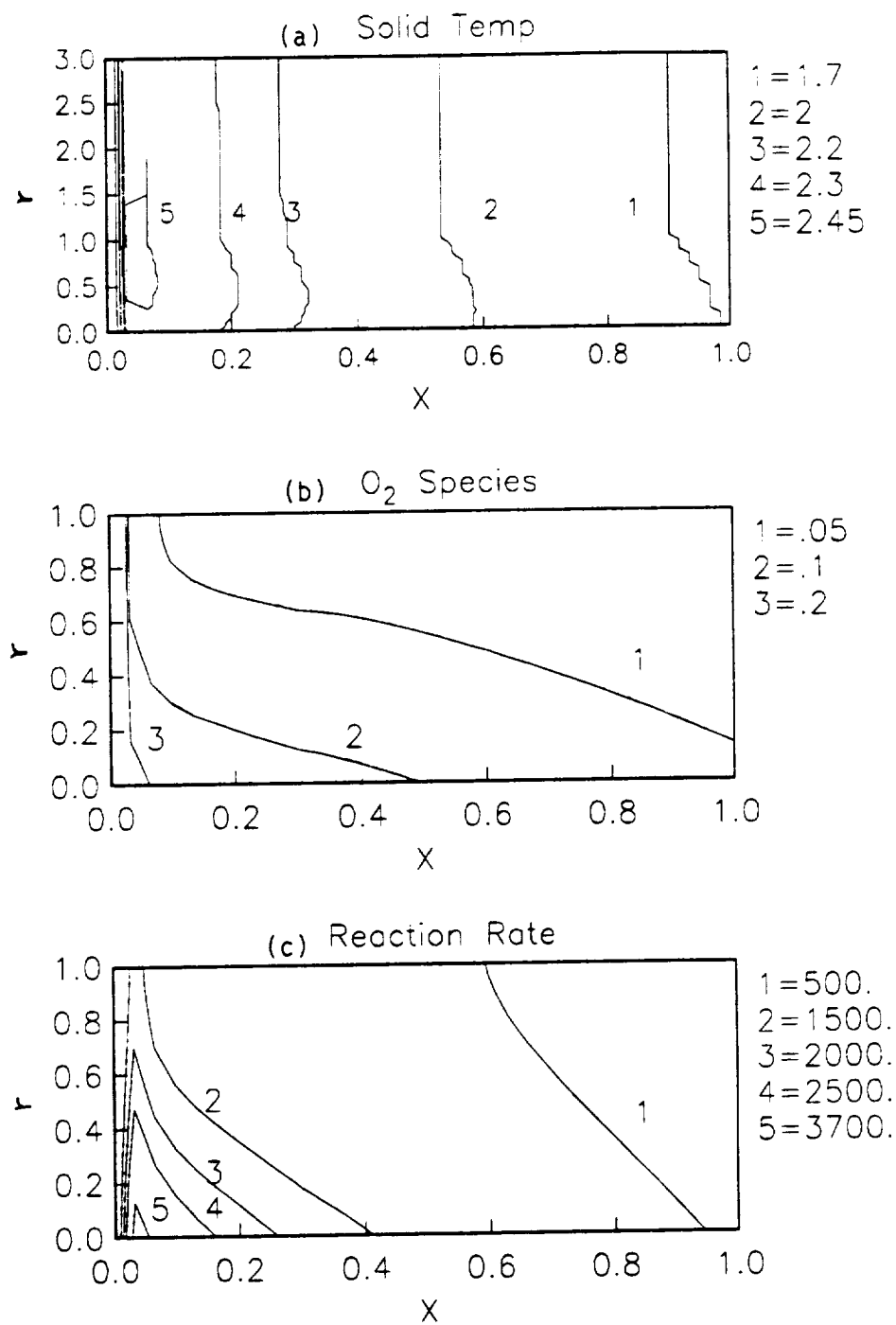


Figure 7 : Solid contours for Case 1 at  $t^* = 1 \tau_{HT}^*$

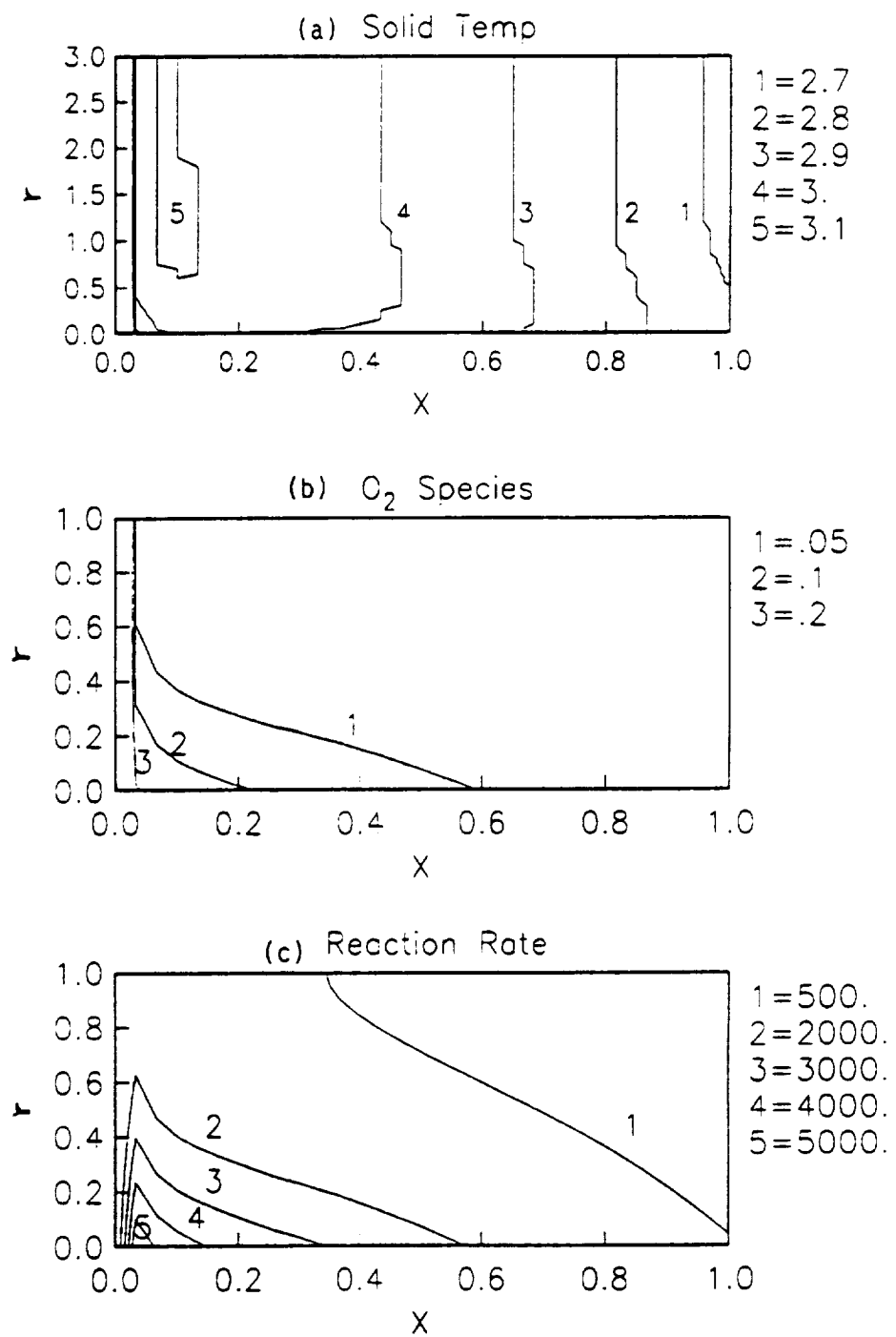


Figure 8 : Solid contours for Case 1 at  $t^* = 2 \tau_{HT}^*$

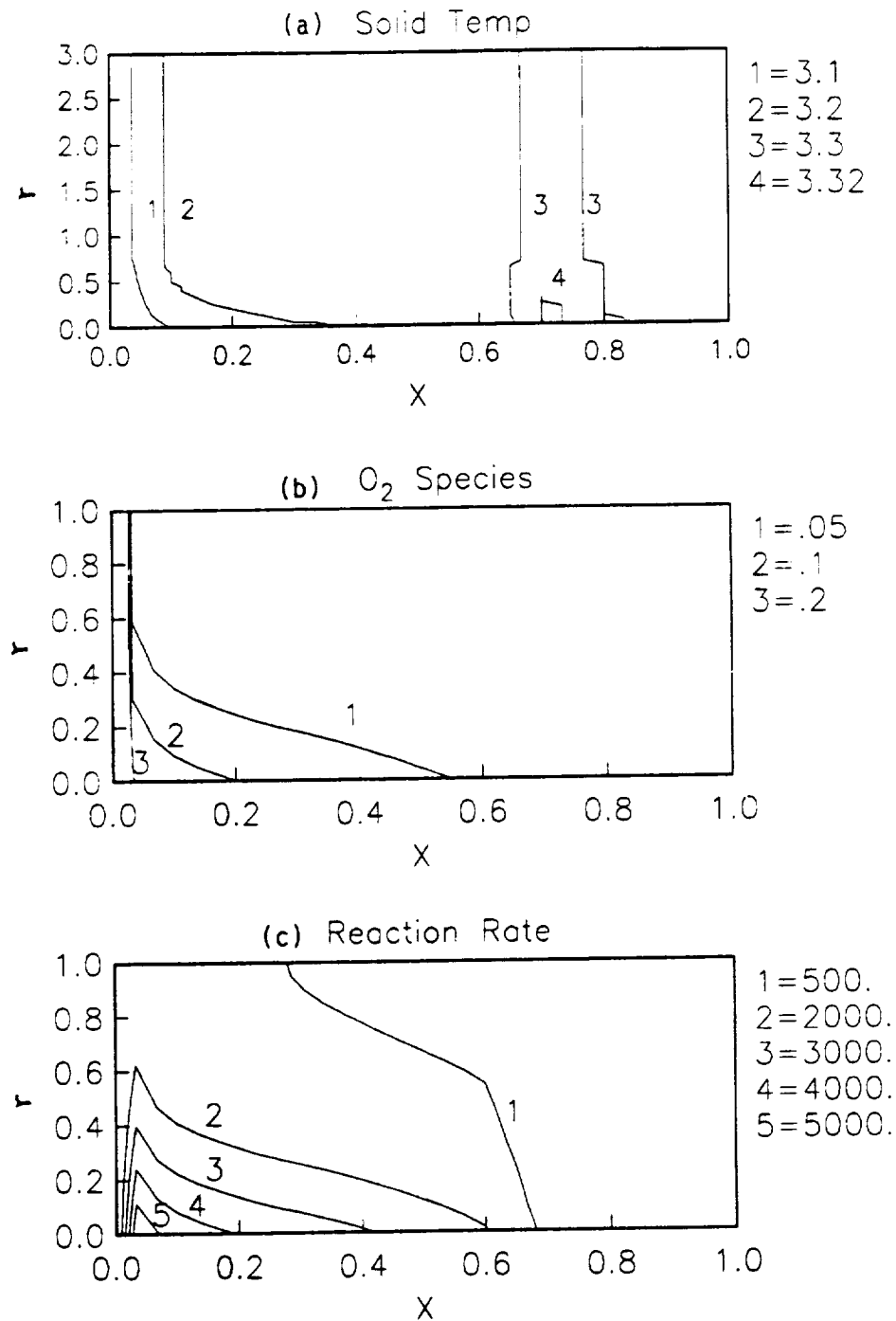


Figure 9 : Solid contours for Case 1 at  $t^* = 3 \tau_{HT}^*$

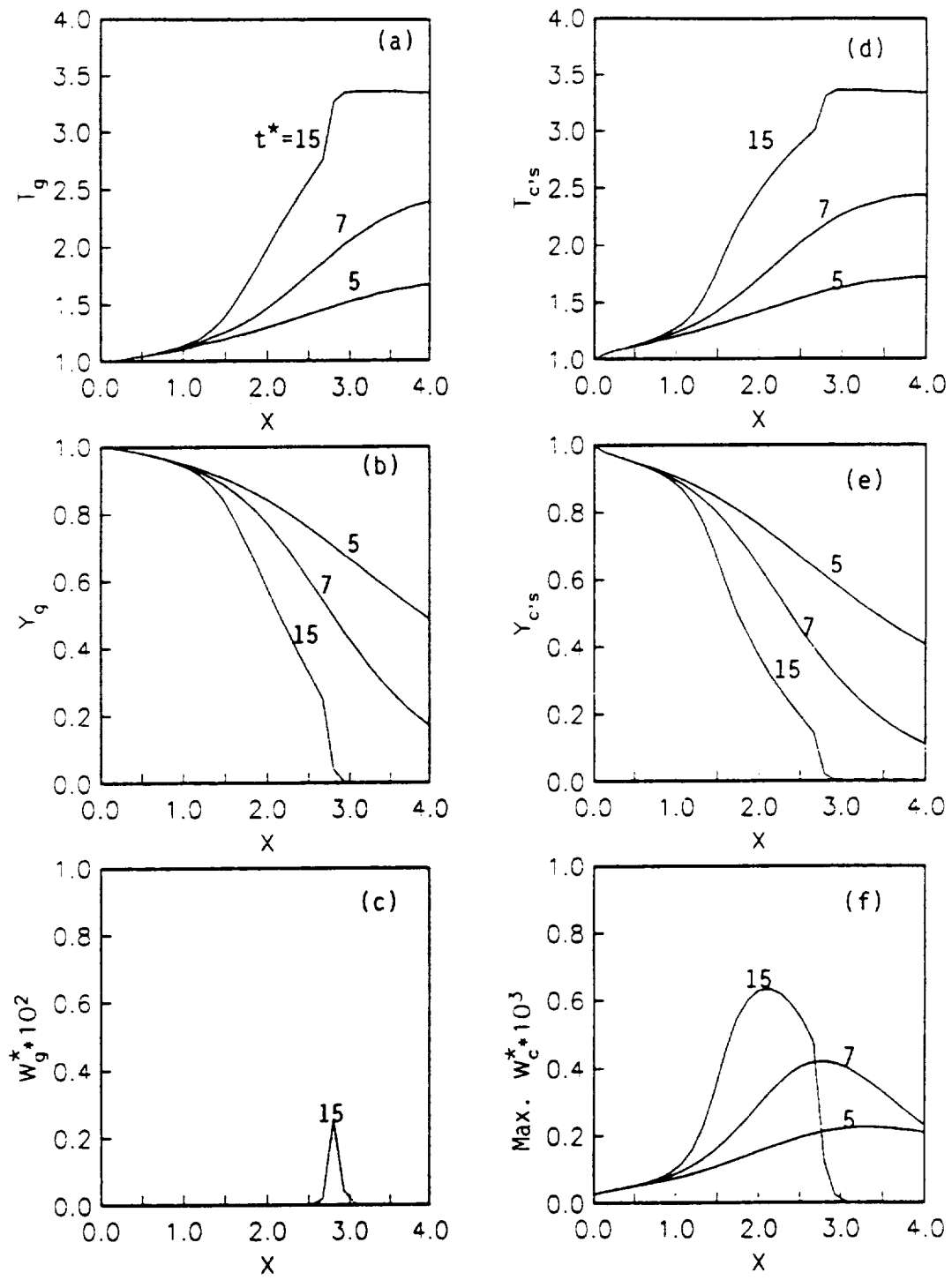


Figure 10 : Transient profiles for Case 2 at  $t^* = 5, 7, 15 \tau_{HT}^*$   
 $(\beta^* = 0.18 \text{ kg-pt/m}^3, L^* = 20 \text{ cm}, \phi = 8)$

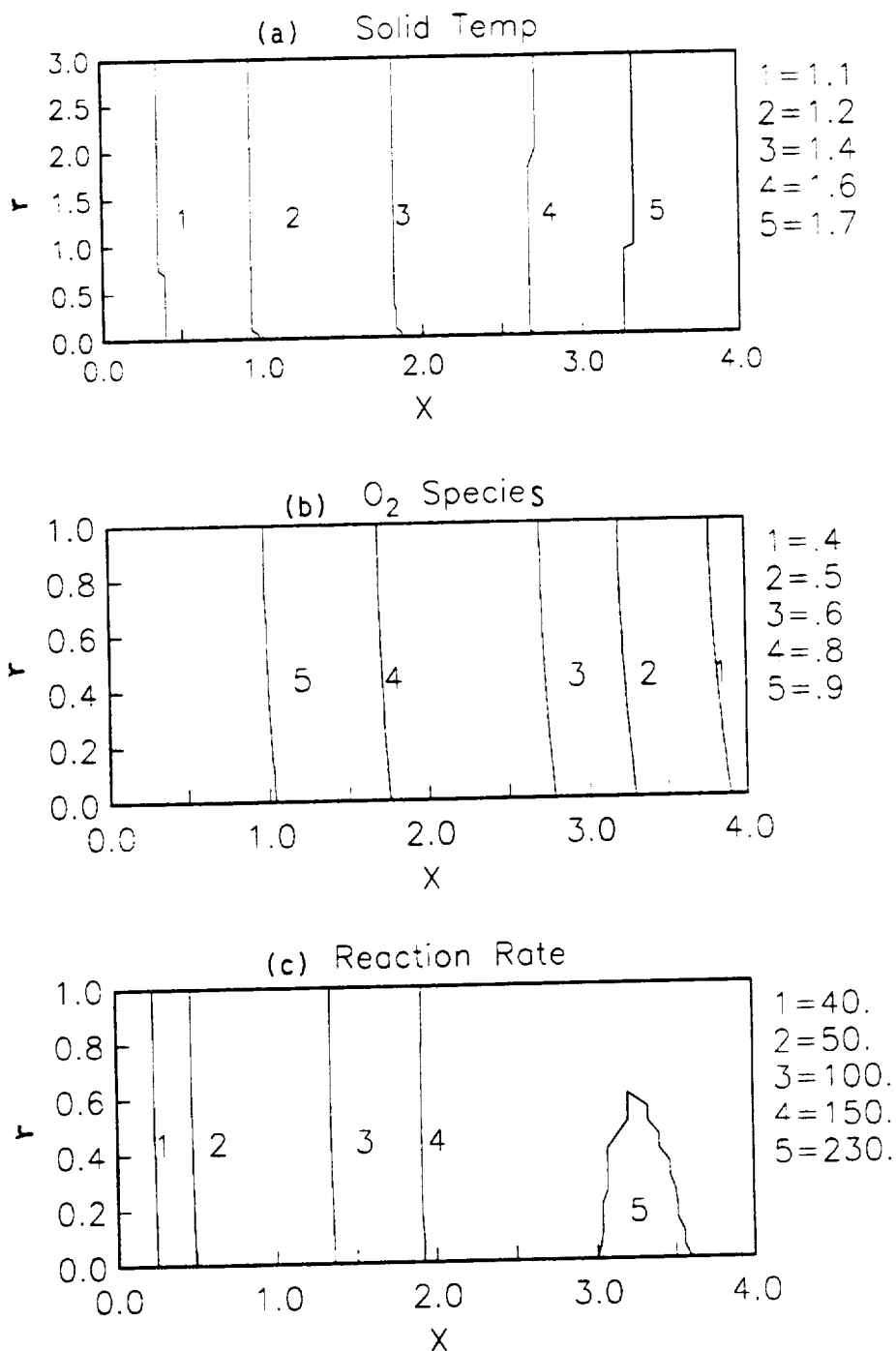


Figure 11 : Solid contours for Case 2 at  $t^* = 5 \tau_{HT}^*$

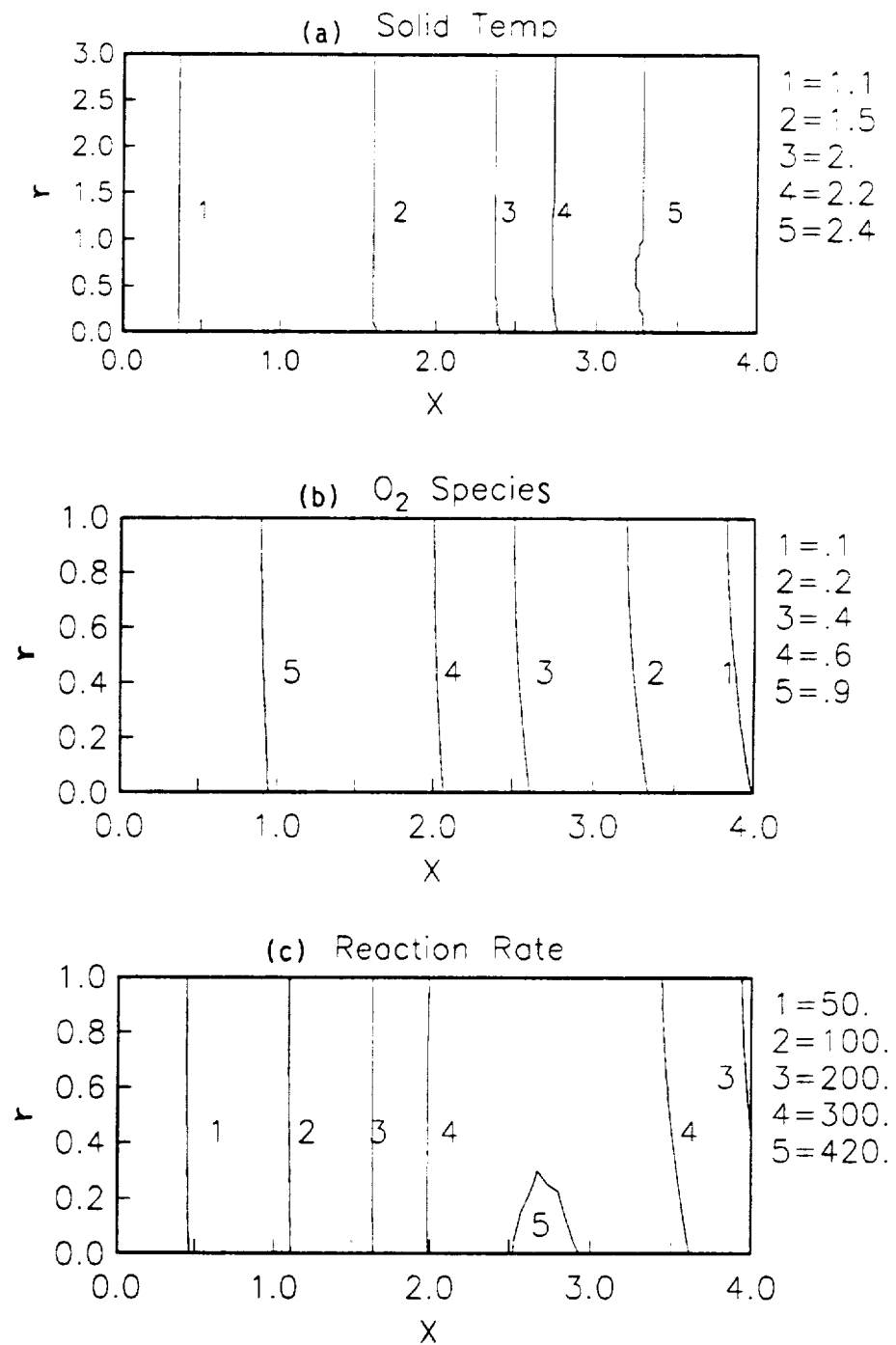


Figure 12 : Solid contours for Case 2 at  $t^* = 7 \tau_{HT}^*$

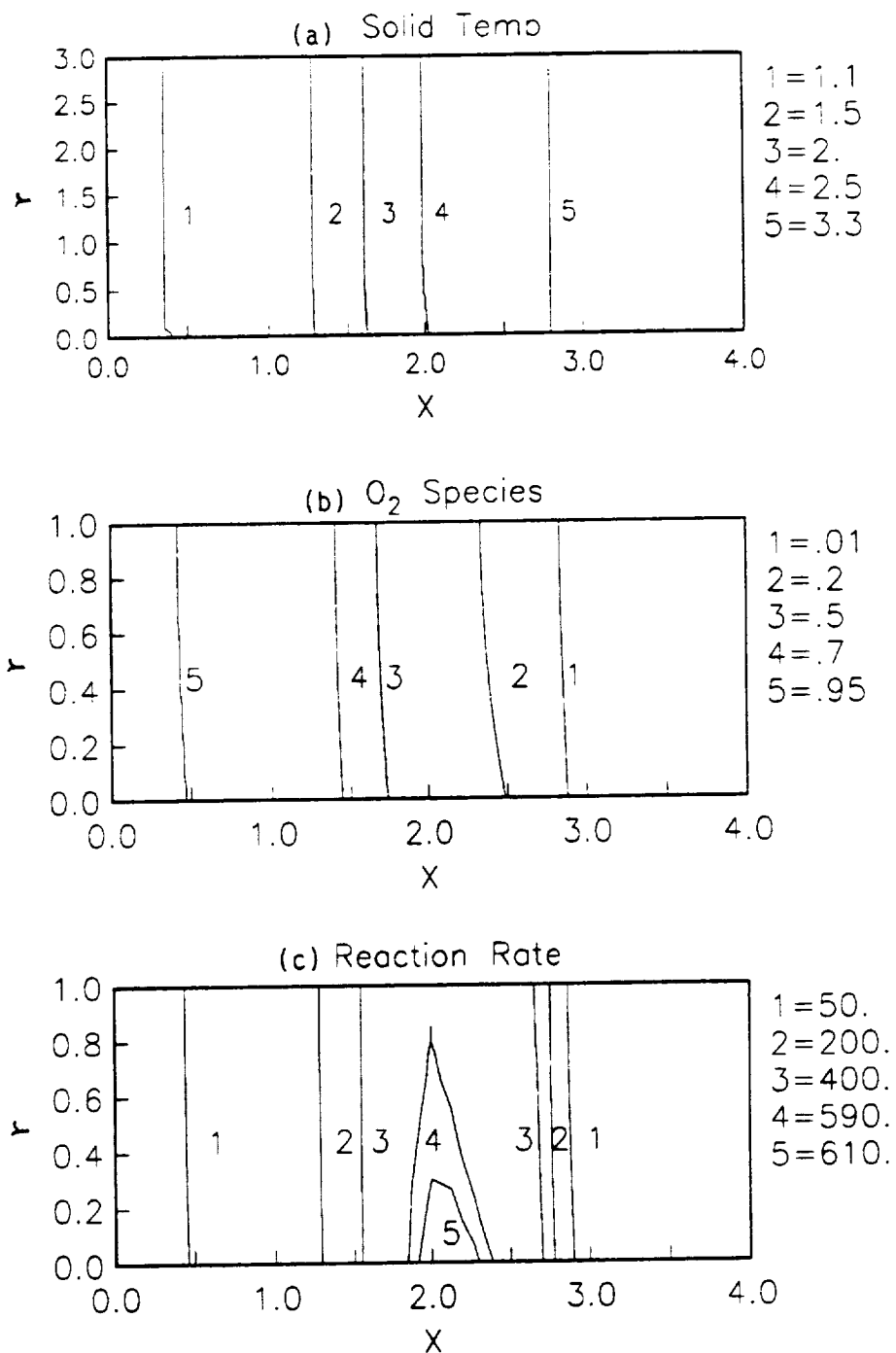


Figure 13 : Solid contours for Case 2 at  $t^* = 15 \tau_{HT}^*$

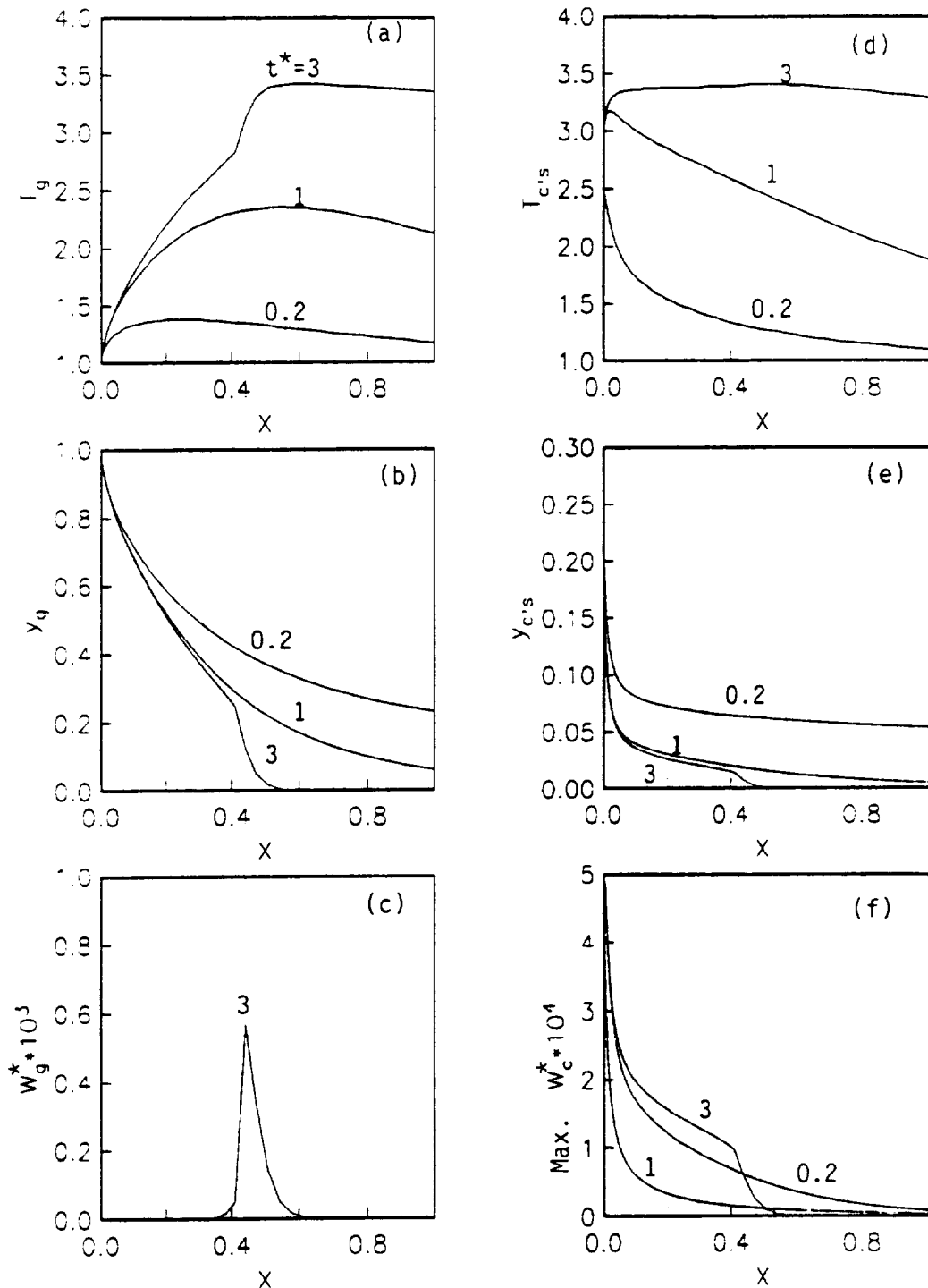


Figure 14 : Transient profiles for Case 3 at  $t^* = 0.2, 1, 3 \tau_{HT}^*$   
 $(\beta^* = 18. \text{ kg-pt/m}^3, L^* = 5 \text{ cm}, \phi = 8)$

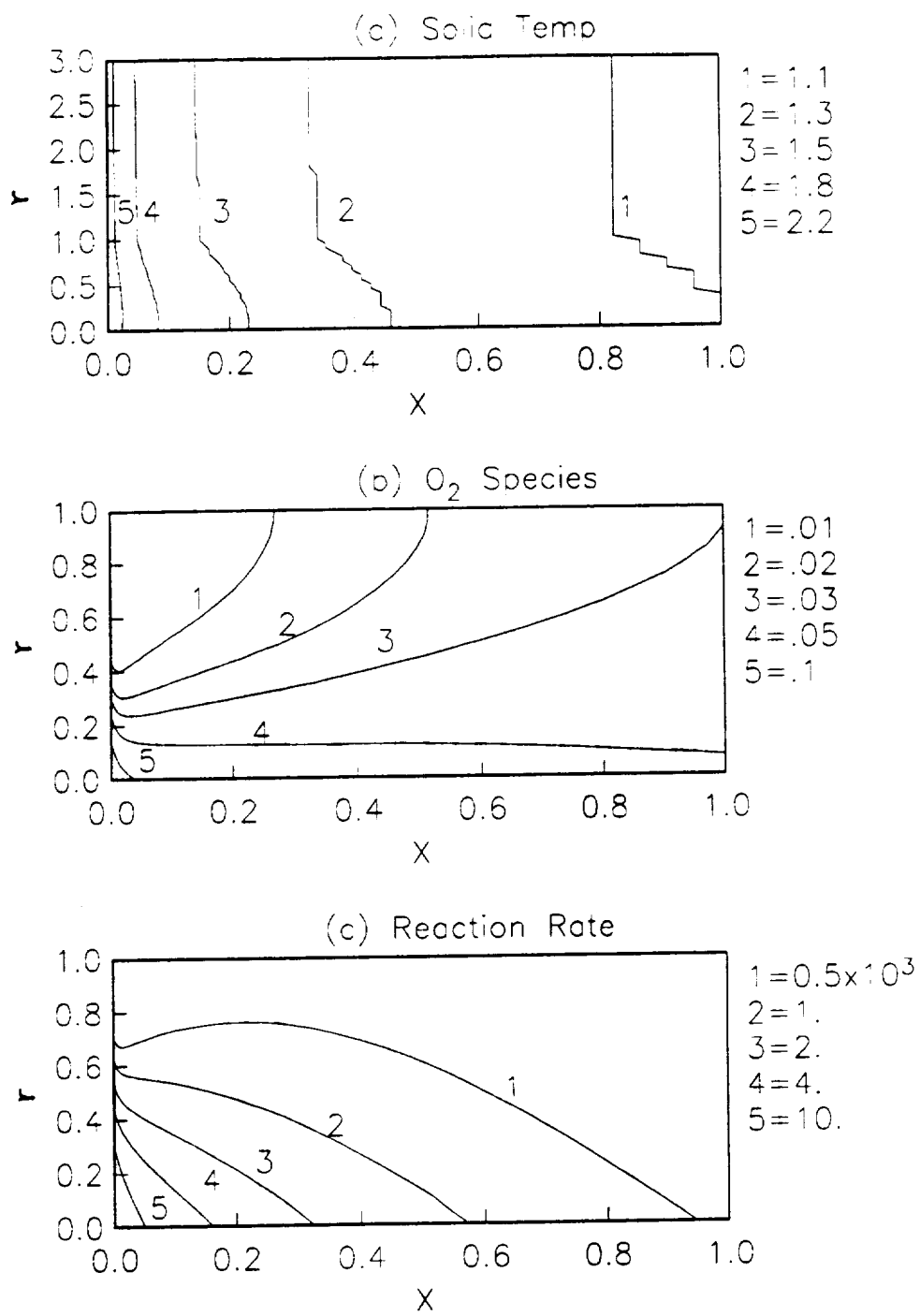


Figure 15 : Solid contours for Case 3 at  $t^* = 0.2 \tau_{HT}^*$

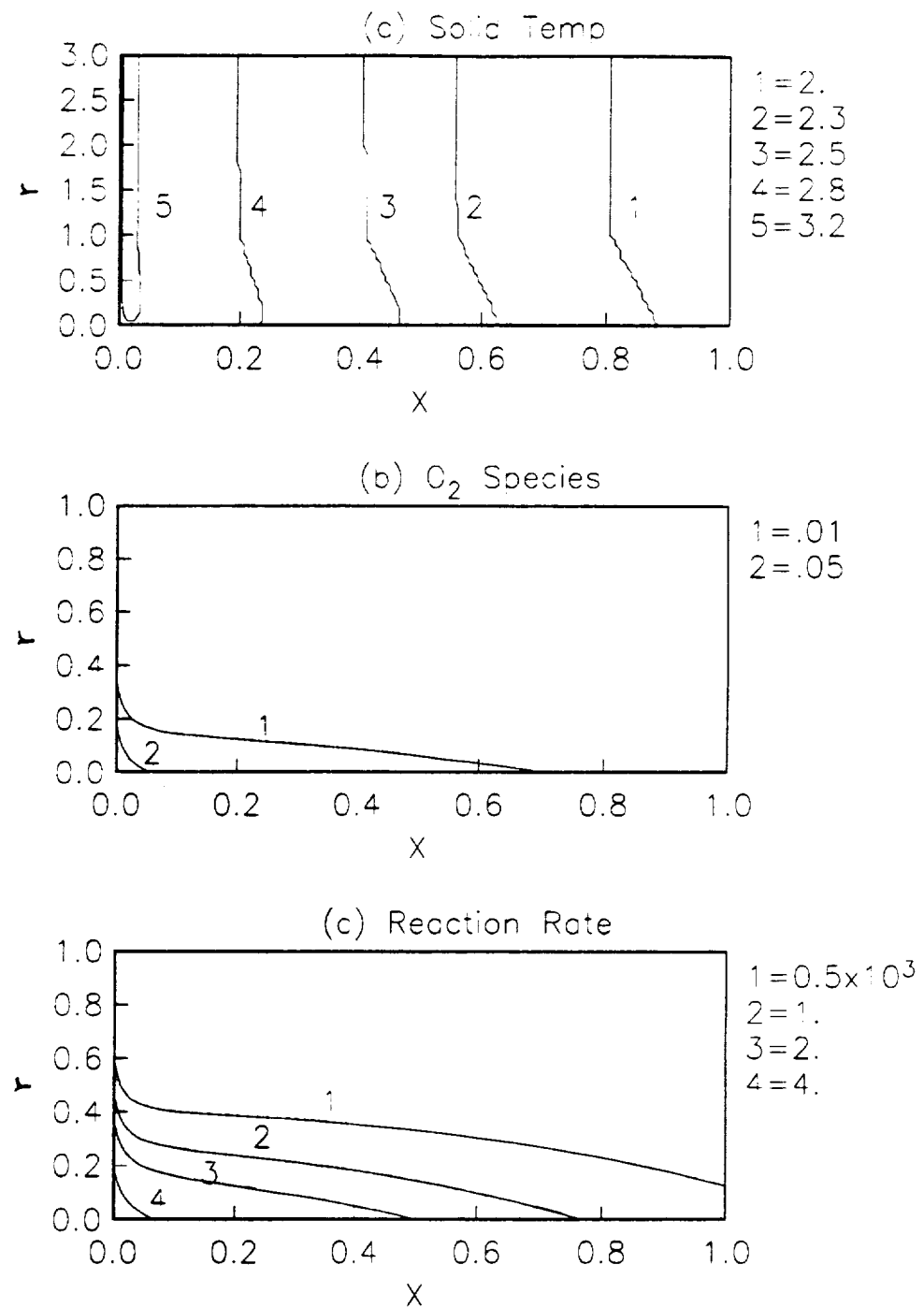


Figure 16 : Solid contours for Case 3 at  $t^* = 1 \tau_{HT}^*$

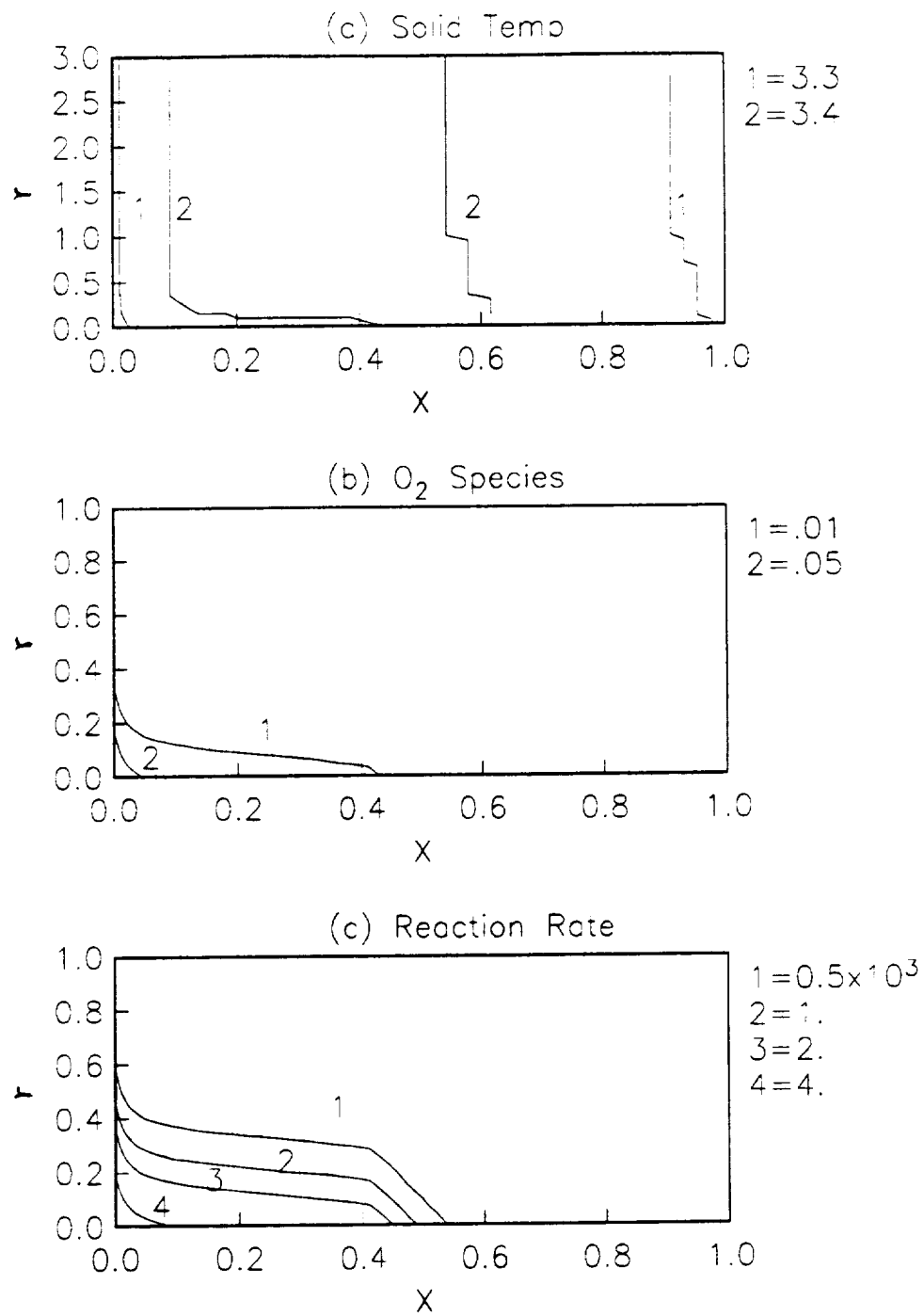


Figure 17 : Solid contours for Case 3 at  $t^* = 3 \tau^*_{HT}$

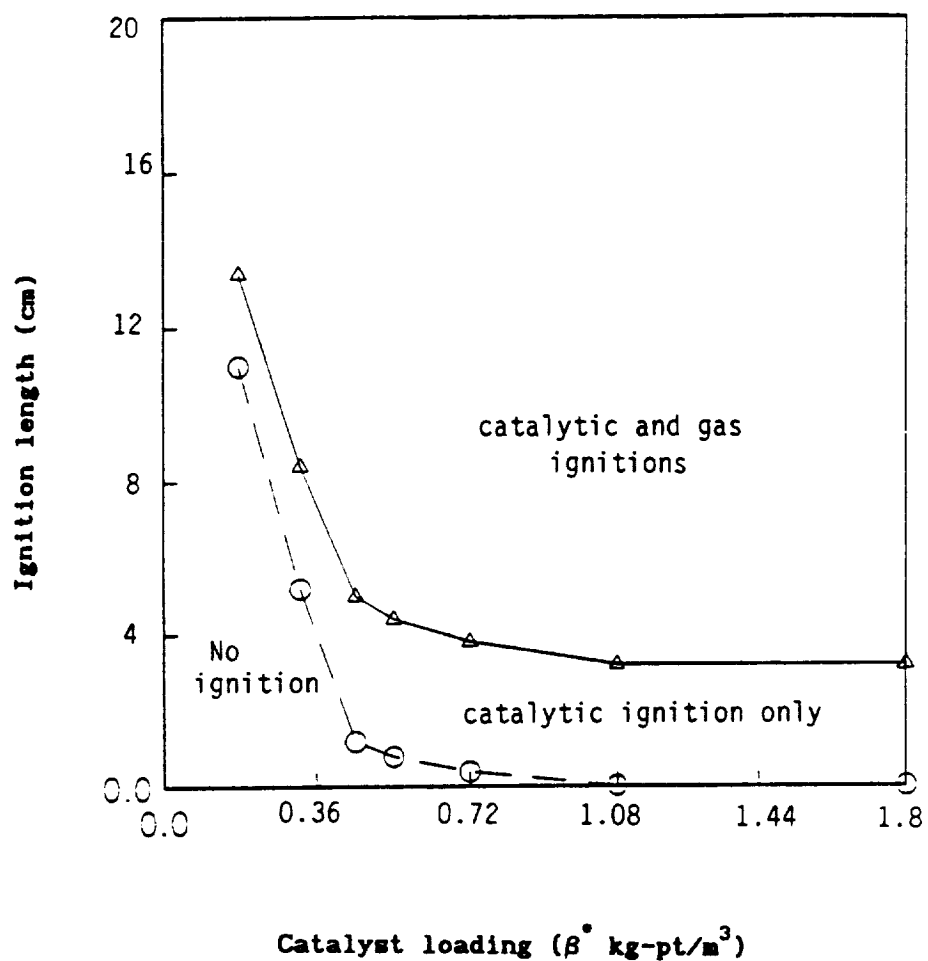


Figure 18 : Ignition boundary map  
 $(u_\infty = 10 \text{ m/sec})$

$\Delta$  : Gas-chcse ignition

$\circ$  : Catalytic ignition

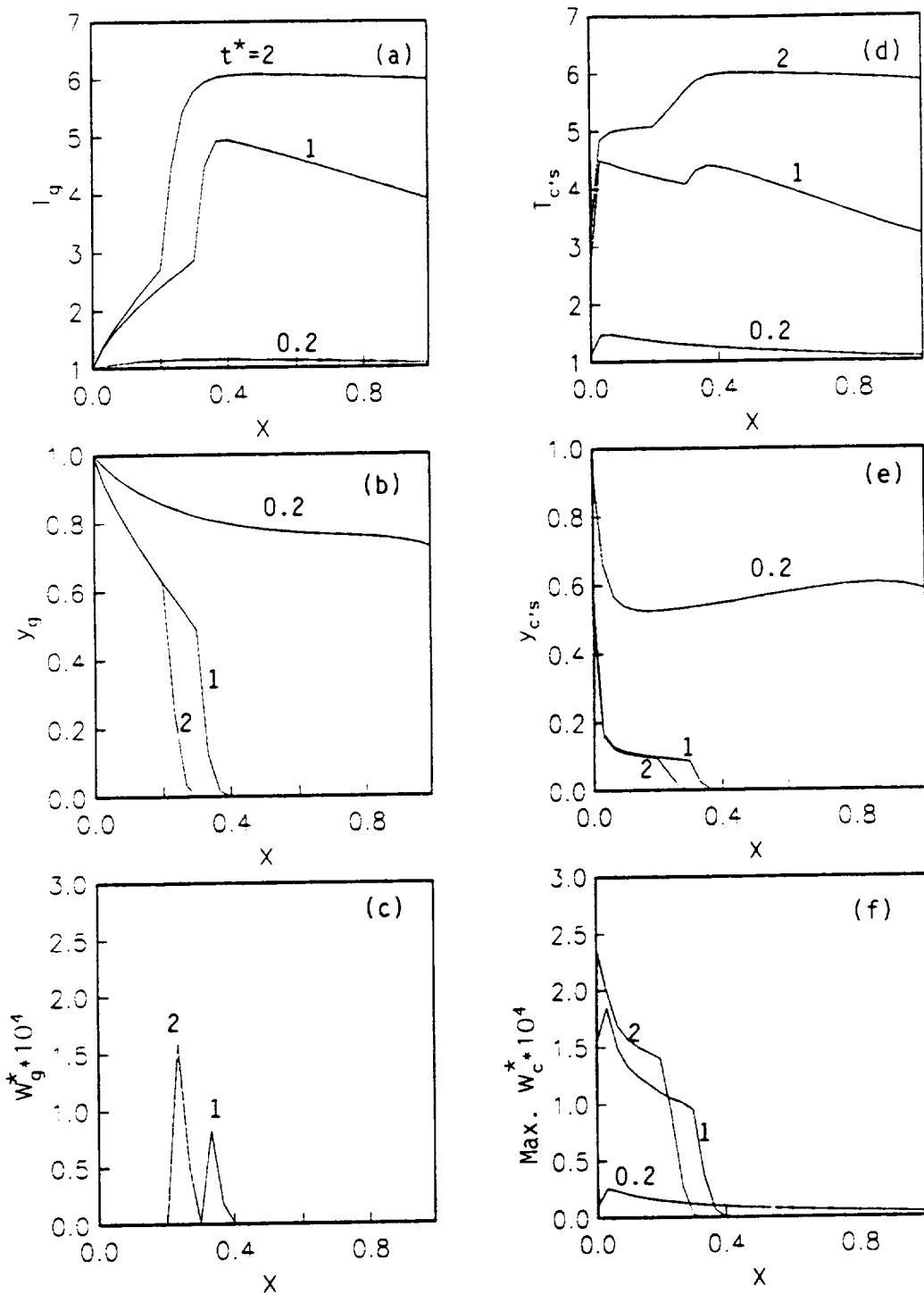


Figure 19 : Transient profiles for Case 4 at  $t^* = 0.2, 1, 2 \tau_{HT}^*$   
 $(\beta^* = 1.8 \text{ kg-pt/m}^3, L^* = 5 \text{ cm}, \phi = 4)$

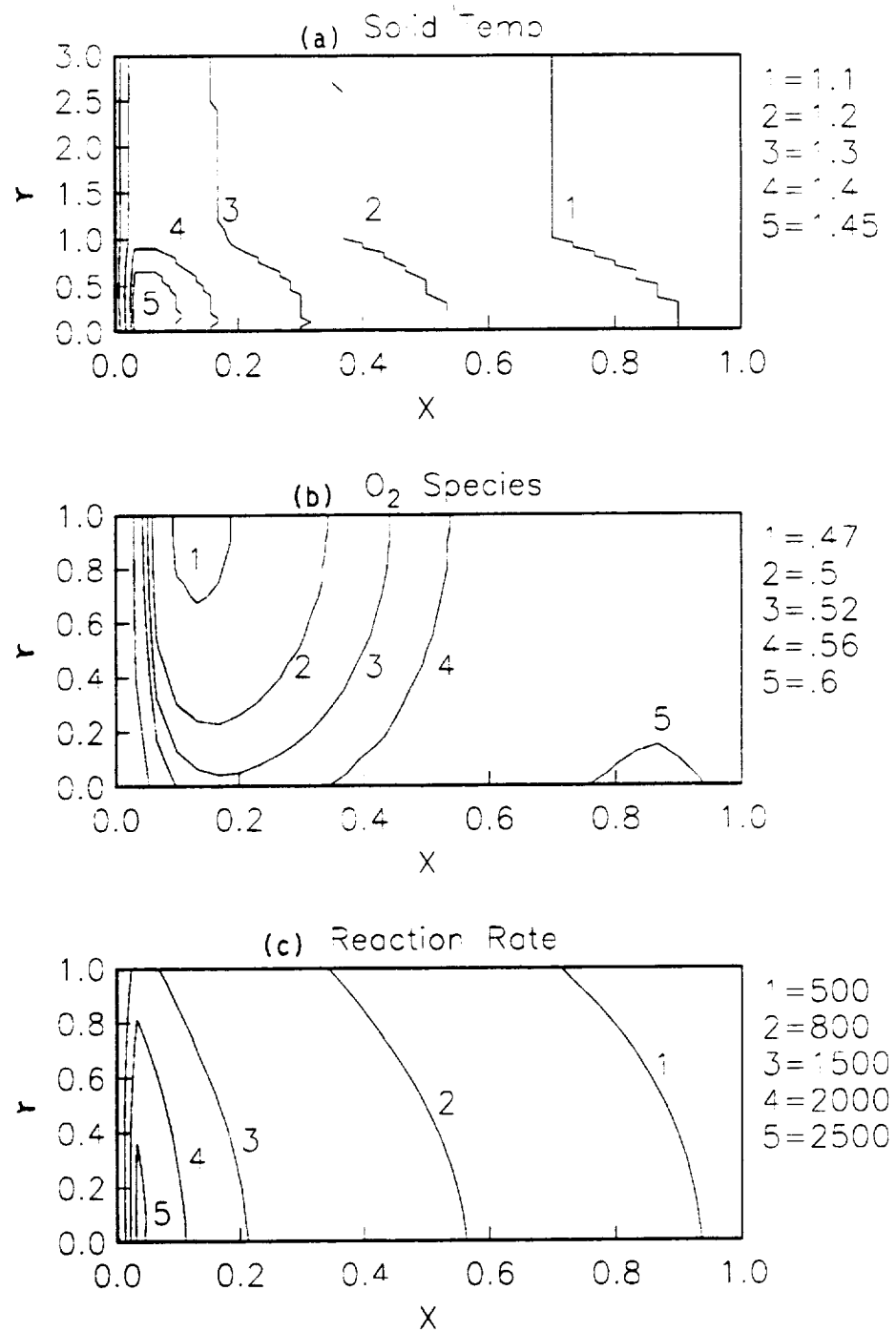


Figure 20 : Solid contours for Case 4 at  $t^* = 0.2 \tau^*_{HT}$

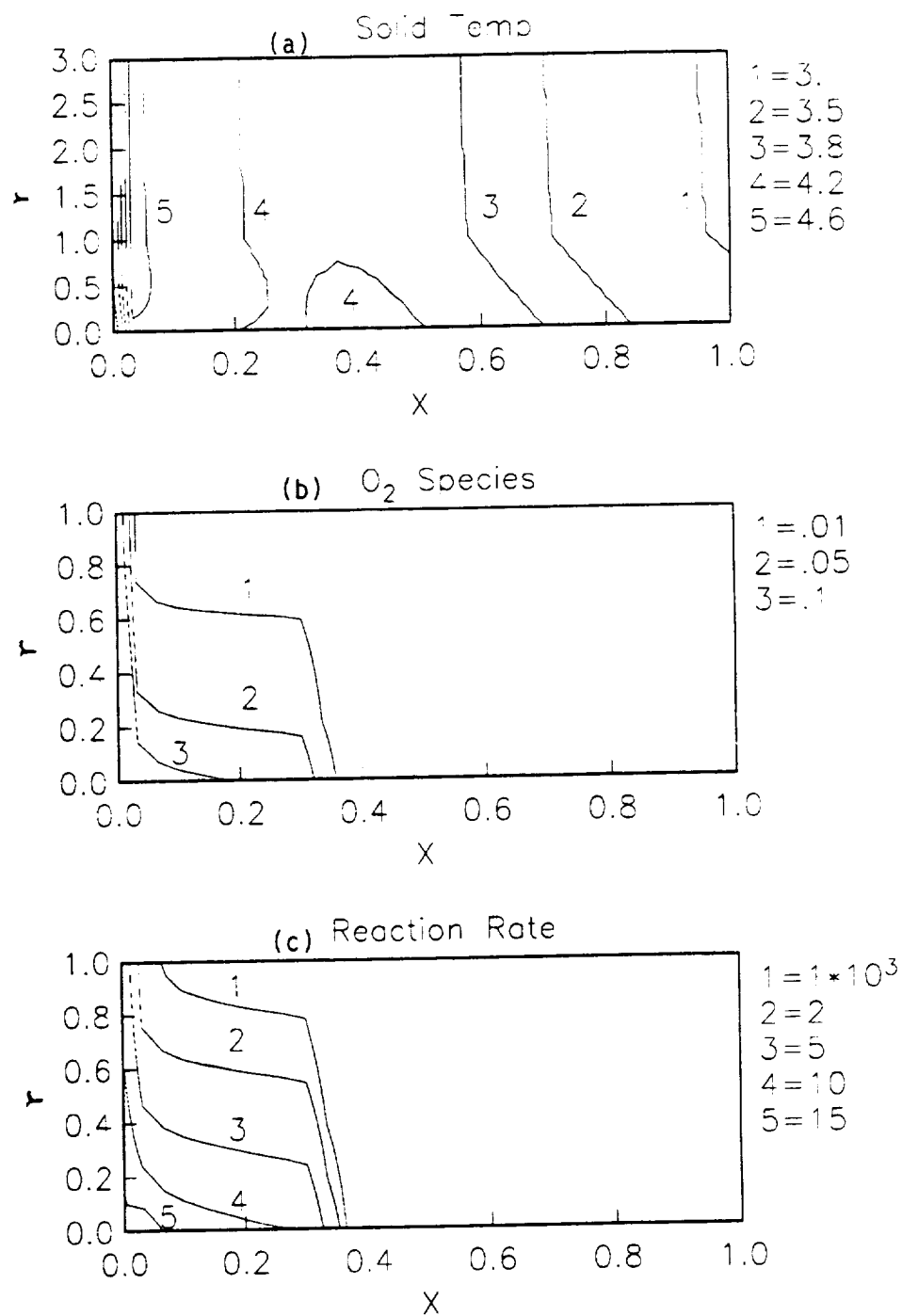


Figure 21 : Solid contours for Case 4 at  $t^* = 1 \tau_{HT}^*$

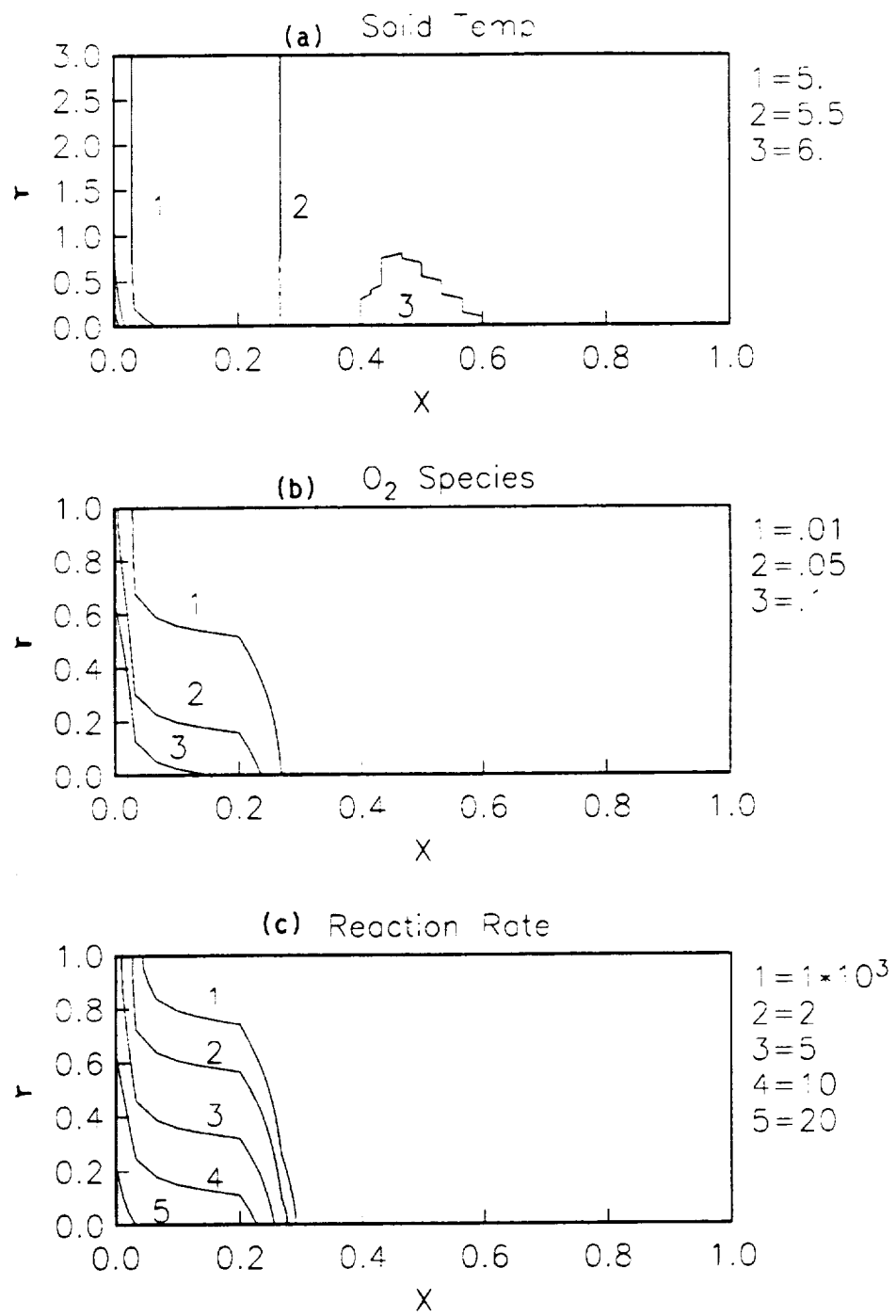


Figure 22 : Solid contours for Case 4 at  $t^* = 2 \tau^*_{HT}$

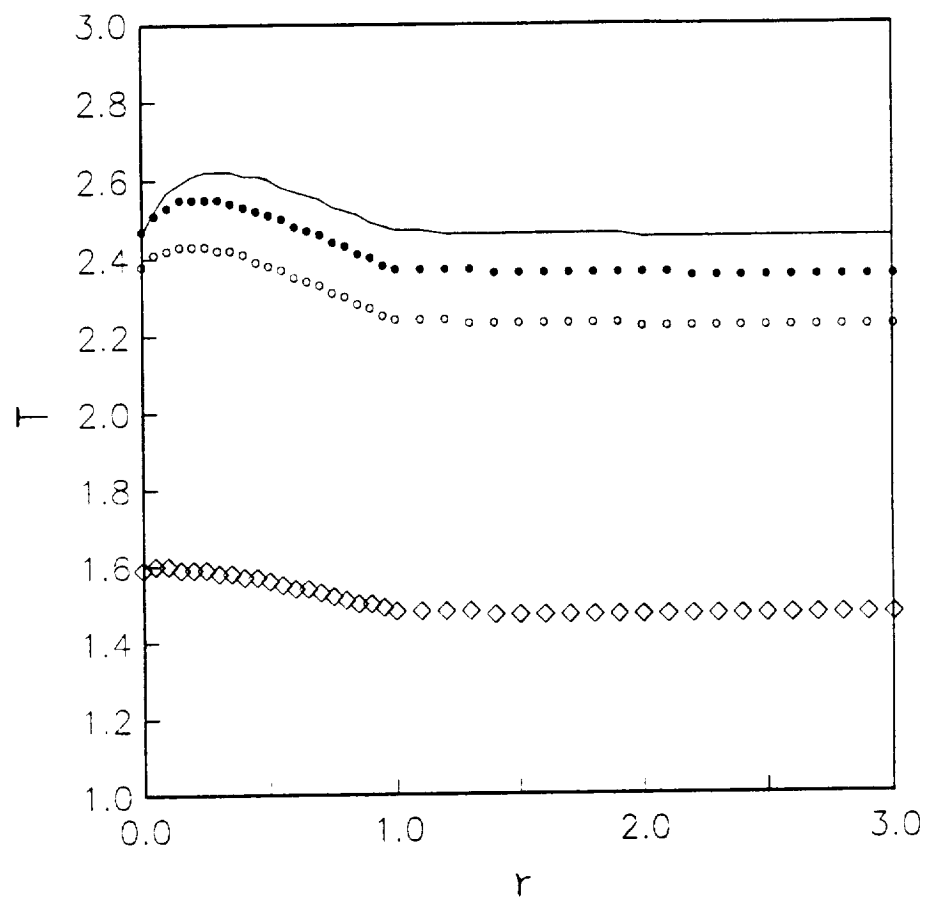


Figure 23 : Solid in-depth temperature profiles for Case 3  
at  $t = 0.2 \tau_{HT}$   
Solid line ( $x=0$ ), ● ( $x=0.005$ ), ○ ( $x=0.01$ ), ◇ ( $x=0.5$ )

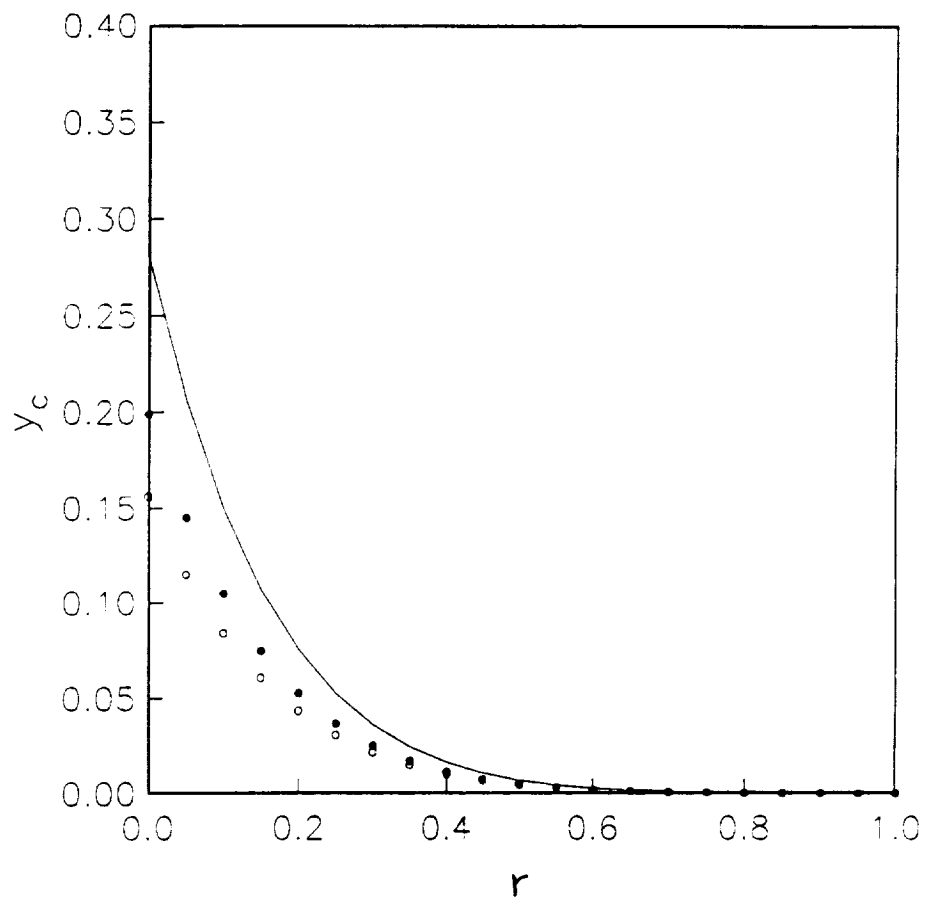


Figure 24 : Solid in-depth species profiles for Case 3  
at  $t = 0.2 \tau_{HT}$   
Solid line ( $x=0$ ), ● ( $x=0.005$ ), ○ ( $x=0.01$ )

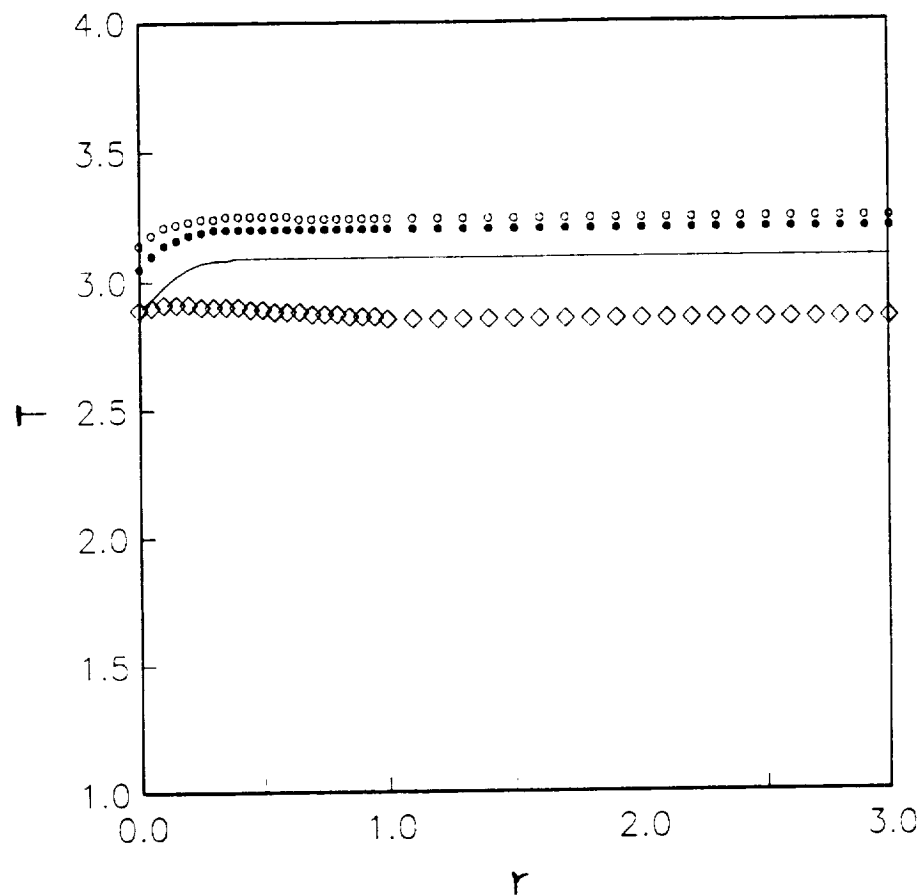


Figure 25 : Solid in-depth temperature profiles for Case 3  
at  $t = 1 \tau_{HT}$   
Solid line ( $x=0$ ), ● ( $x=0.005$ ), ○ ( $x=0.01$ ), ◇ ( $x=0.5$ )

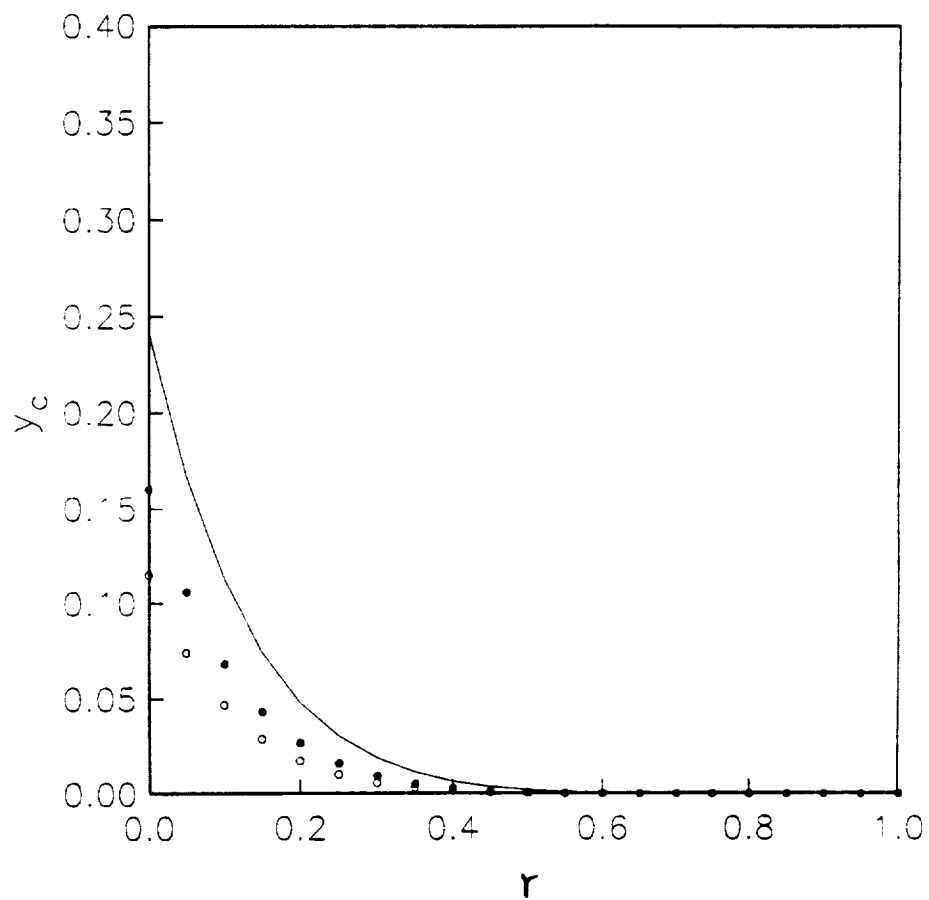


Figure 26 : Solid in-depth species profiles for Case 3

at  $t = 1 \tau_{HT}$

Solid line ( $x=0$ ), ● ( $x=0.005$ ), ○ ( $x=0.01$ )

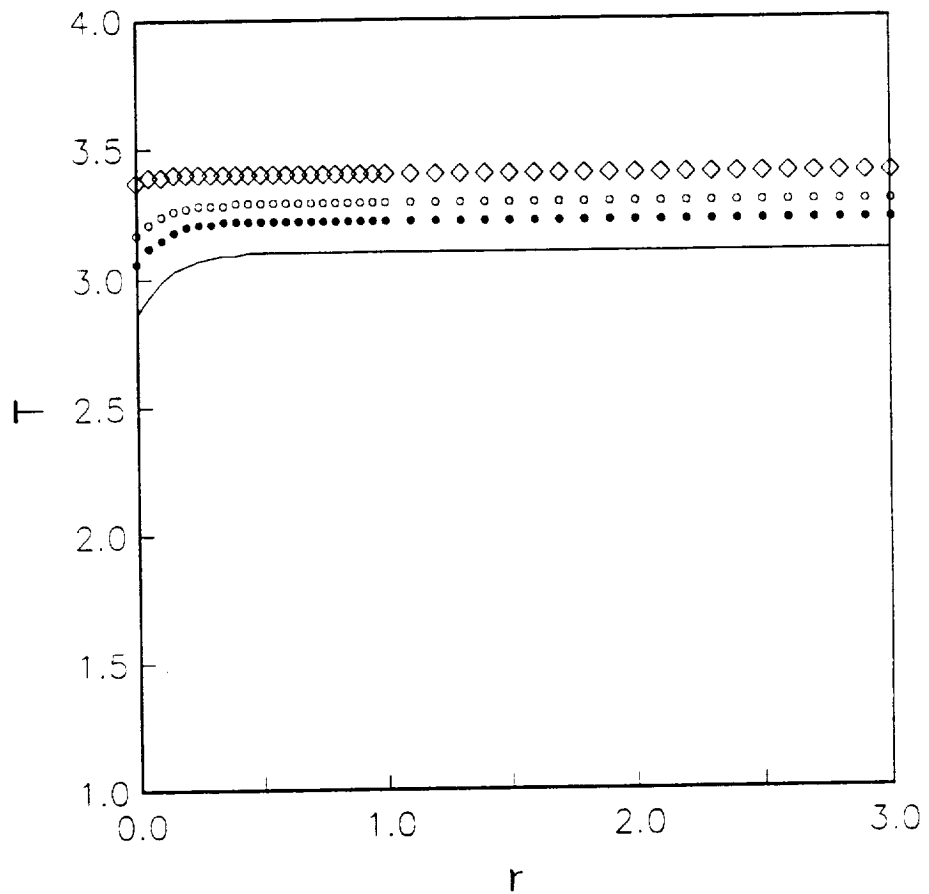


Figure 27 : Solid in-depth temperature profiles for Case 3  
at  $t = 3 \tau_{HT}$   
Solid line ( $x=0$ ),  $\bullet$  ( $x=0.005$ ),  $\circ$  ( $x=0.01$ ),  $\diamond$  ( $x=0.5$ )

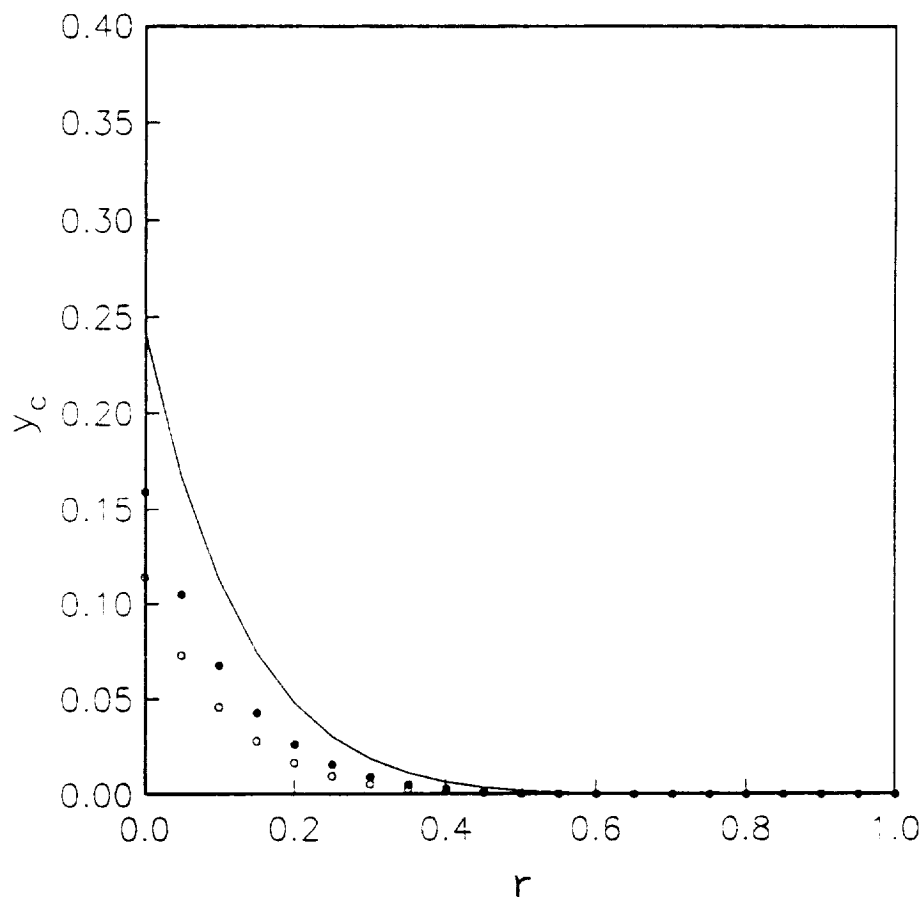


Figure 28 : Solid in-depth species profiles for Case 3  
at  $t = 3 \tau_{HT}$   
Solid line ( $x=0$ ), ● ( $x=0.005$ ), ○ ( $x=0.01$ )

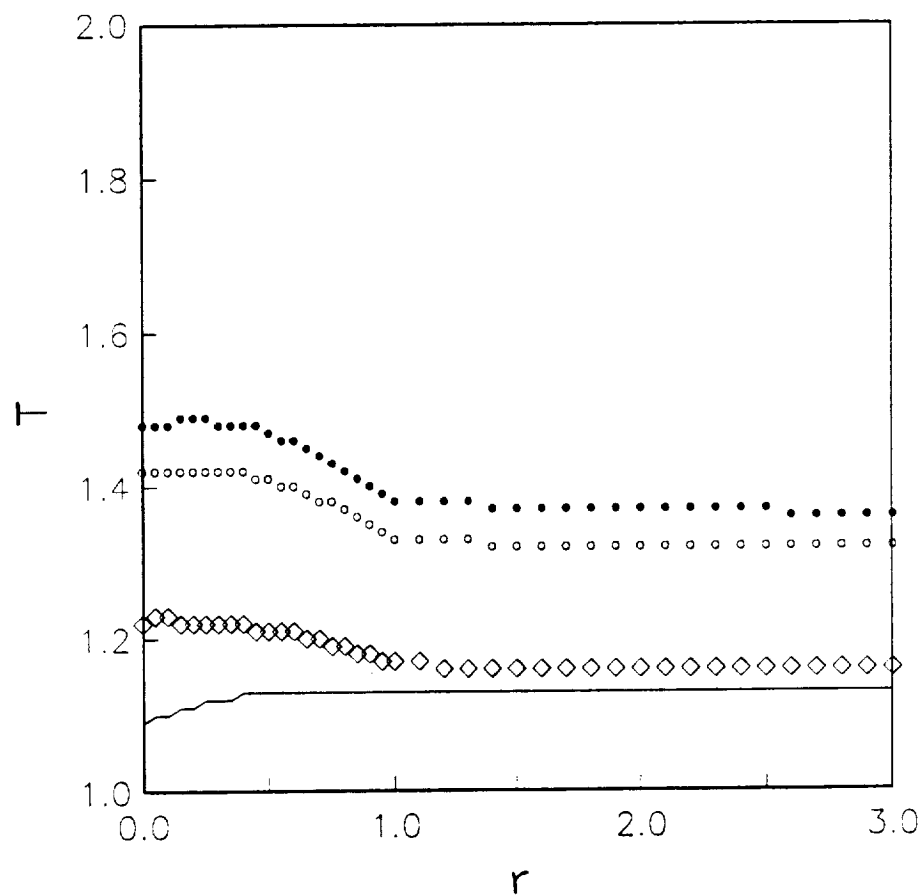


Figure 29 : Solid in-depth temperature profiles for Case 4  
at  $t = 0.2 \tau_{HT}$   
Solid line ( $x=0$ ), ● ( $x=0.06$ ), ○ ( $x=0.12$ ), ◇ ( $x=0.5$ )

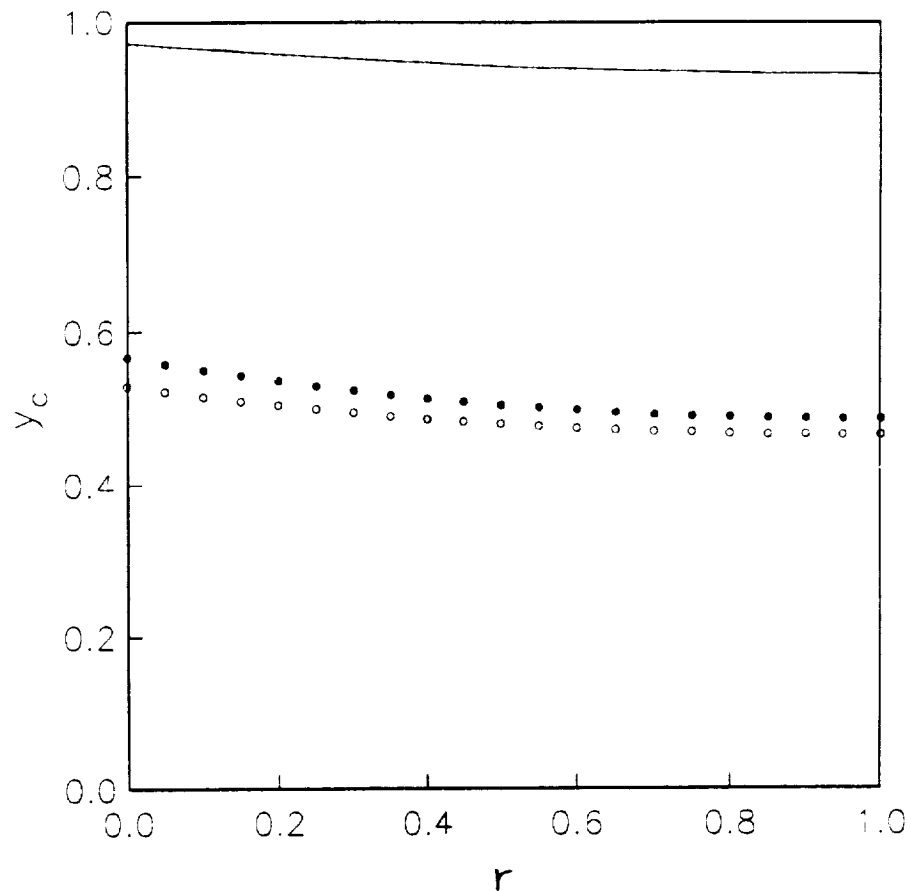


Figure 30 : Solid in-depth species profiles for Case 4  
at  $t = 0.2 \tau_{HT}$   
Solid line ( $x=0$ ), ● ( $x=0.06$ ), ○ ( $x=0.12$ )

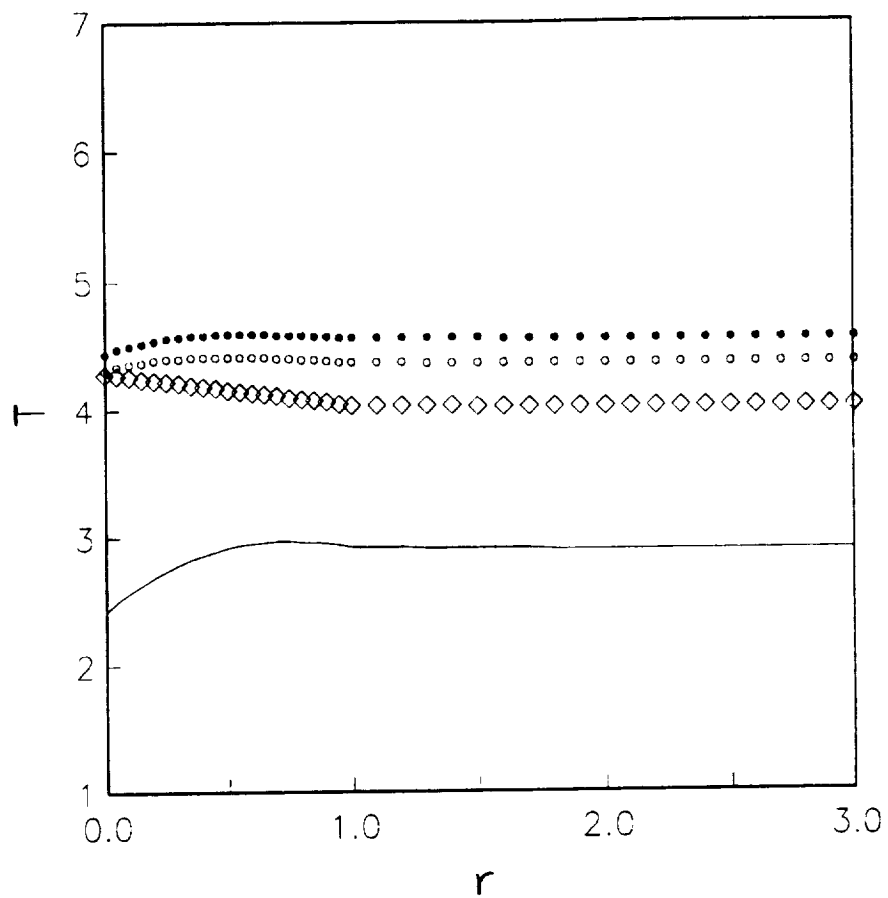


Figure 31 : Solid in-depth temperature profiles for Case 4  
at  $t = 1 \tau_{HT}$   
Solid line ( $x=0$ ), ● ( $x=0.06$ ), ○ ( $x=0.12$ ), ◇ ( $x=0.5$ )

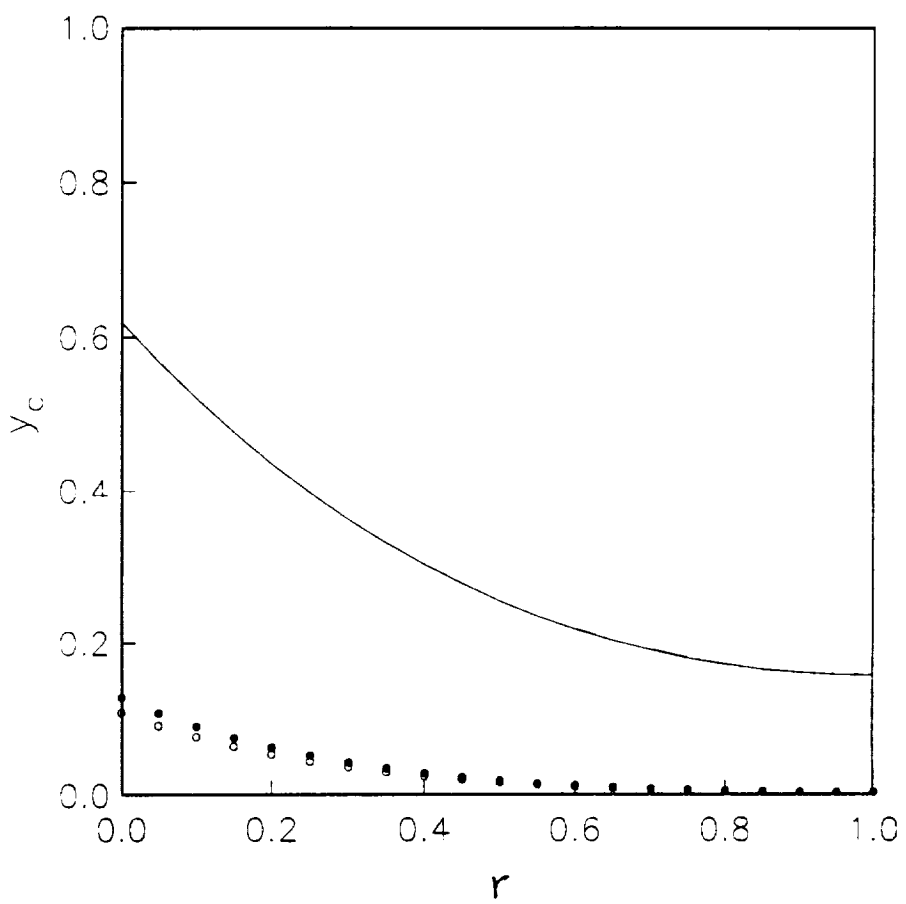


Figure 32 : Solid in-depth species profiles for Case 4  
at  $t = 1 \tau_{HT}$   
Solid line ( $x=0$ ), ● ( $x=0.06$ ), ○ ( $x=0.12$ )

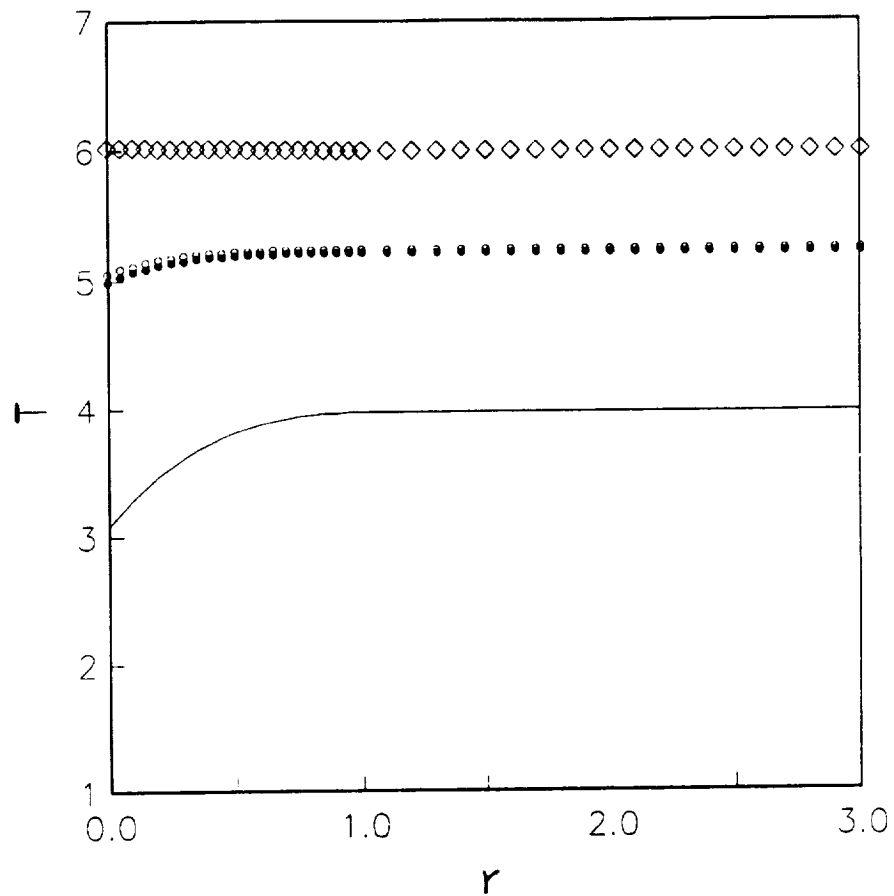


Figure 33 : Solid in-depth temperature profiles for Case 4  
at  $t = 2 \tau_{HT}$   
Solid line ( $x=0$ ),  $\bullet$  ( $x=0.06$ ),  $\circ$  ( $x=0.12$ ),  $\diamond$  ( $x=0.5$ )

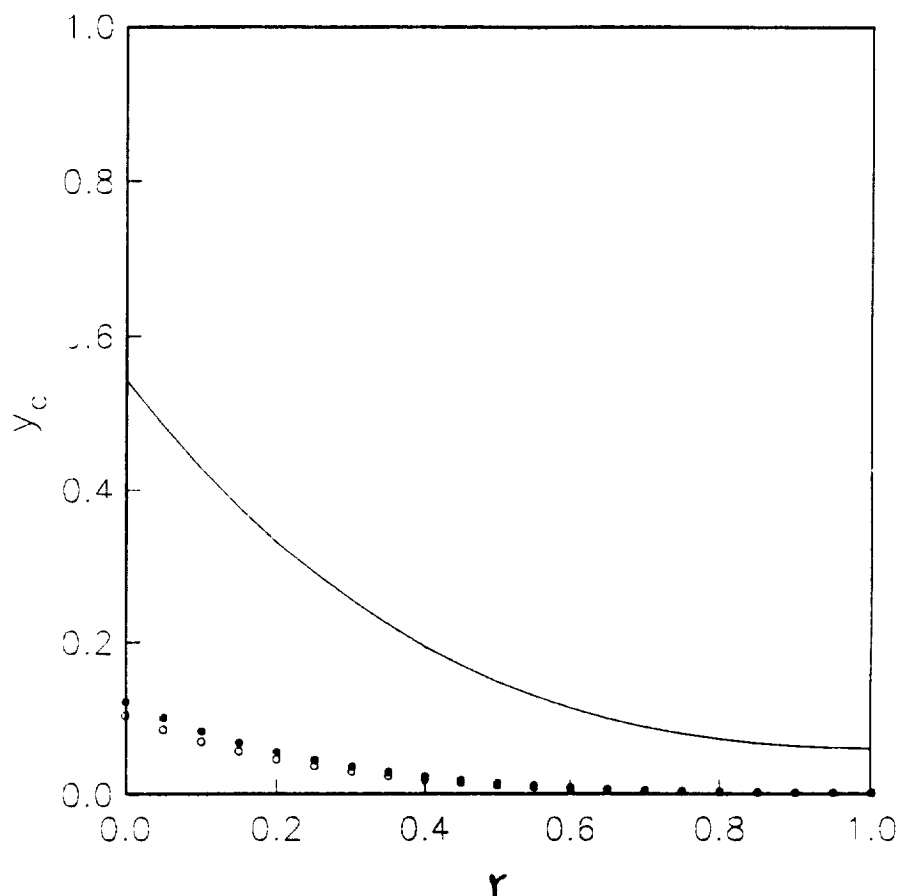


Figure 34 : Solid in-depth species profiles for Case 4  
at  $t = 2 \tau_{HT}$   
Solid line ( $x=0$ ), ● ( $x=0.06$ ), ○ ( $x=0.5$ )

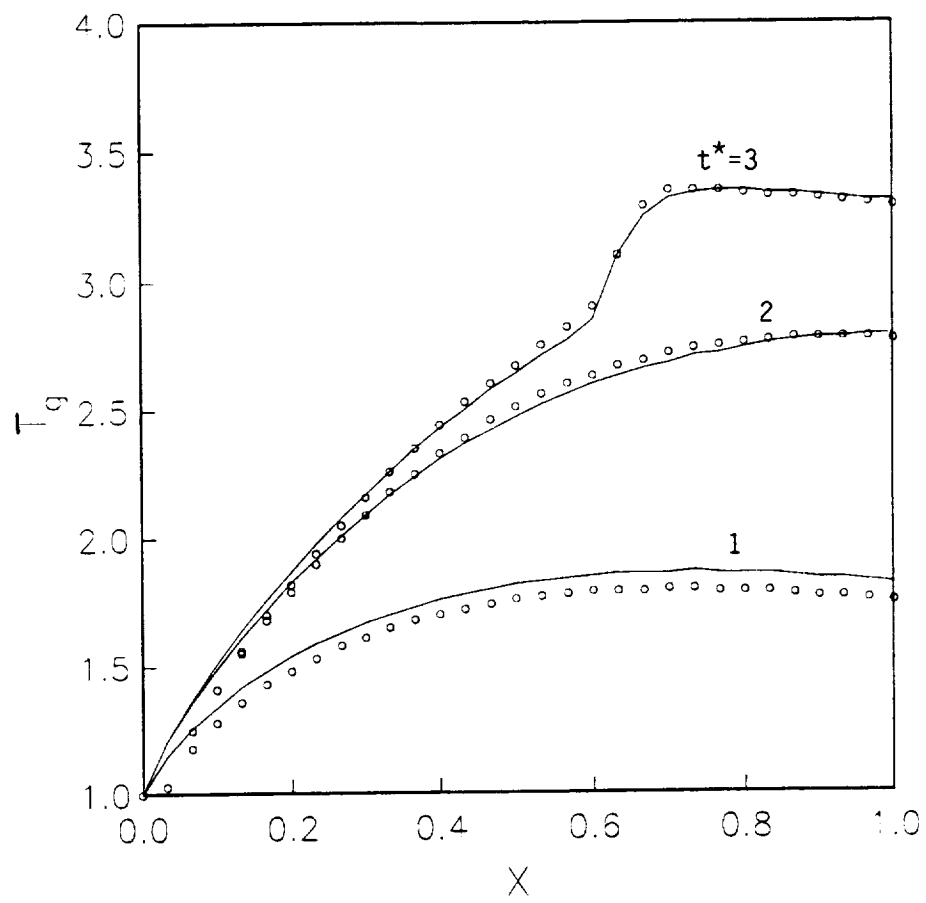
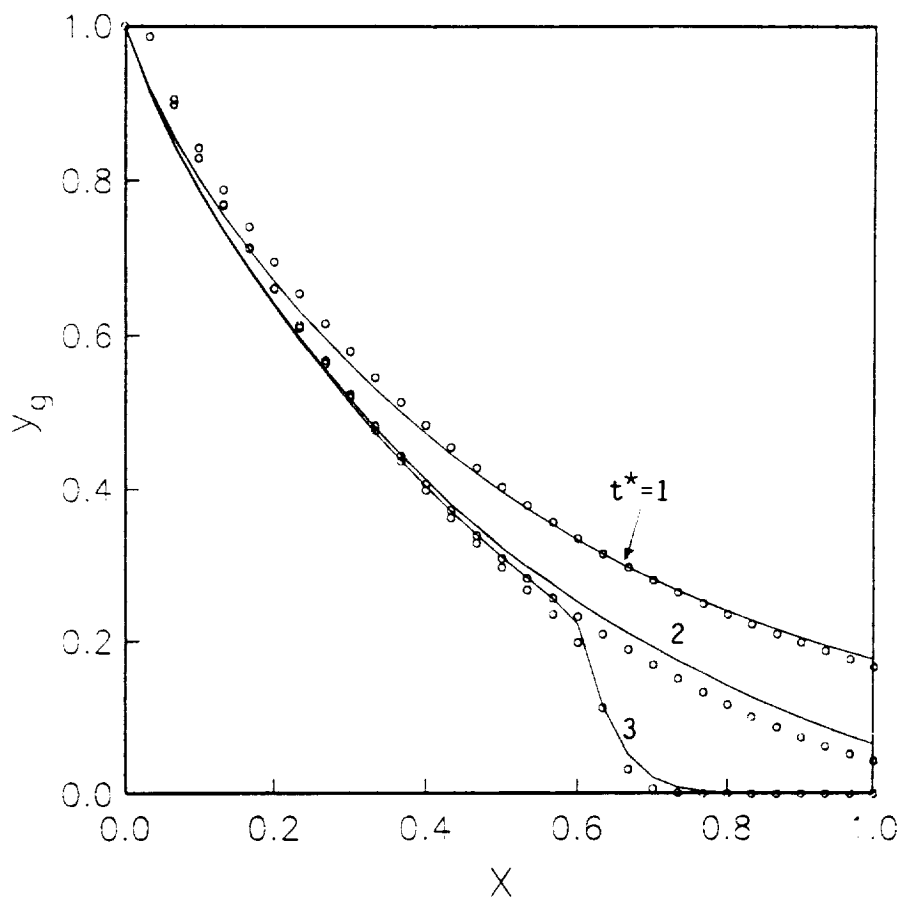


Figure 35 : Comparisons of two models for Case 1 on  $T_q$  at  $t = 1, 2, 3 \tau_{HT}$

Solid line : full transient model  
 Symbol O : energy integral model



**Figure 36 : Comparisons of two models for Case 1 on  $y_g$  at  $t = 1, 2, 3 \tau_{HT}$**

Solid line : full transient model  
 Symbol O : energy integral mode

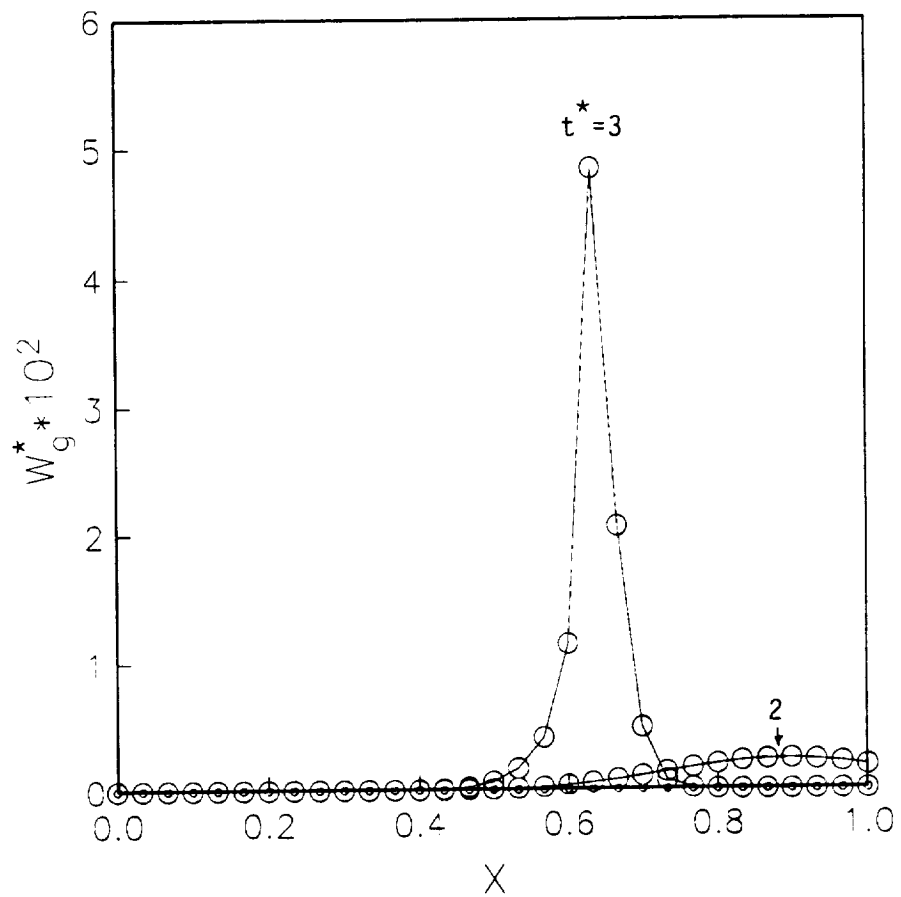


Figure 37 : Comparisons of two models for Case 1 on  $W_g^*$  at  $t = 1, 2, 3 \tau_{HT}$

Solid line : full transient model  
Symbol O : energy integral model

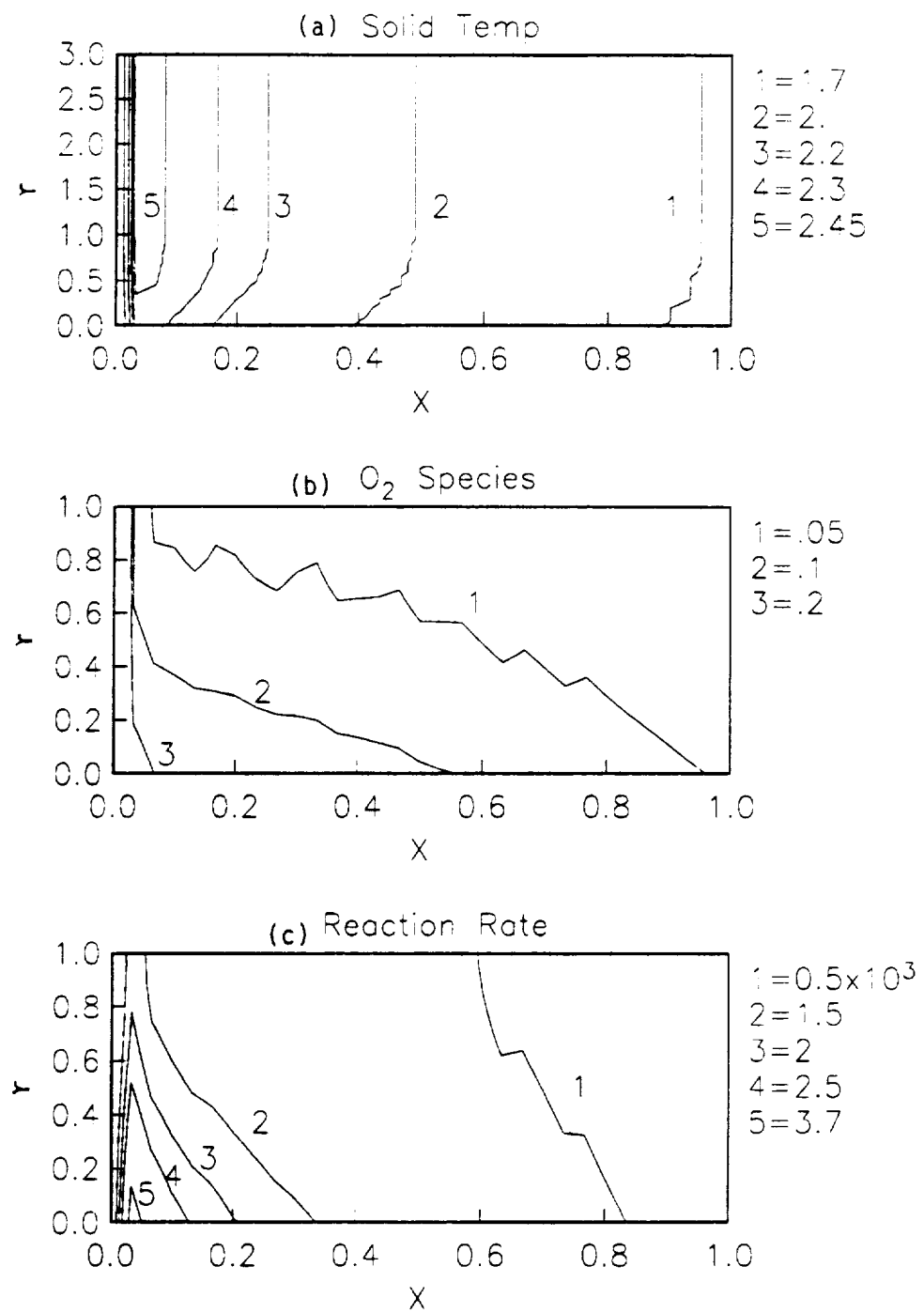


Figure 38 : Solid contours for Case 1 at  $t^* = 1 \tau_{HT}^*$   
by energy integral model

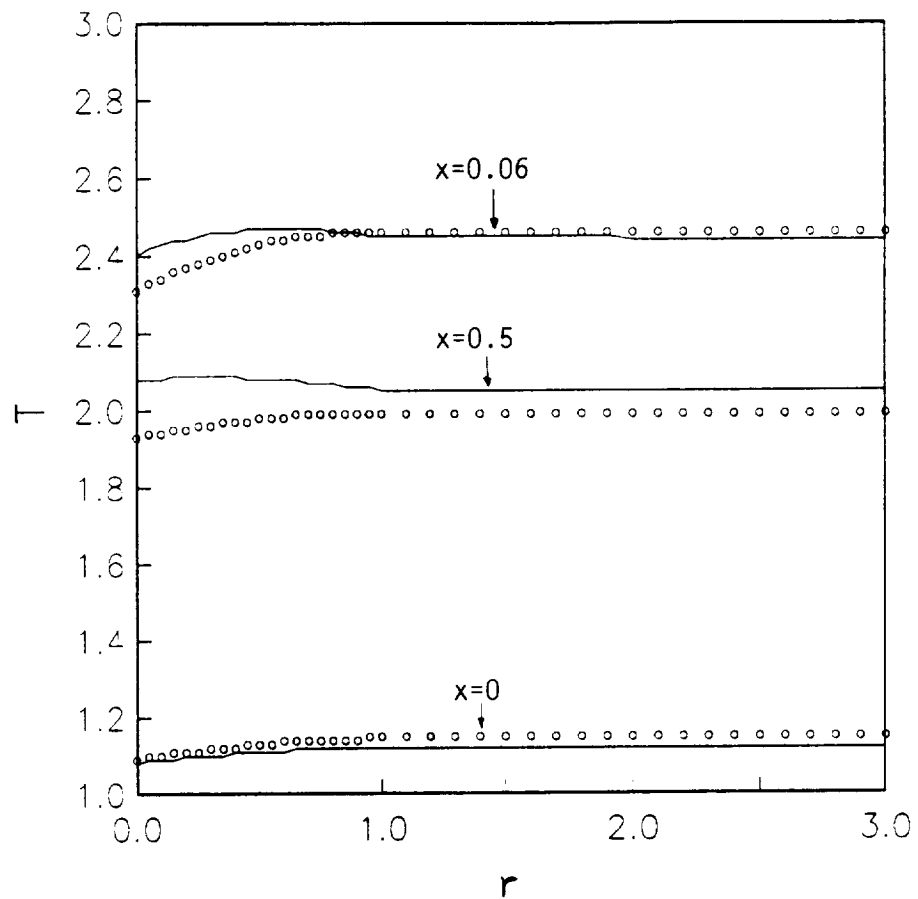
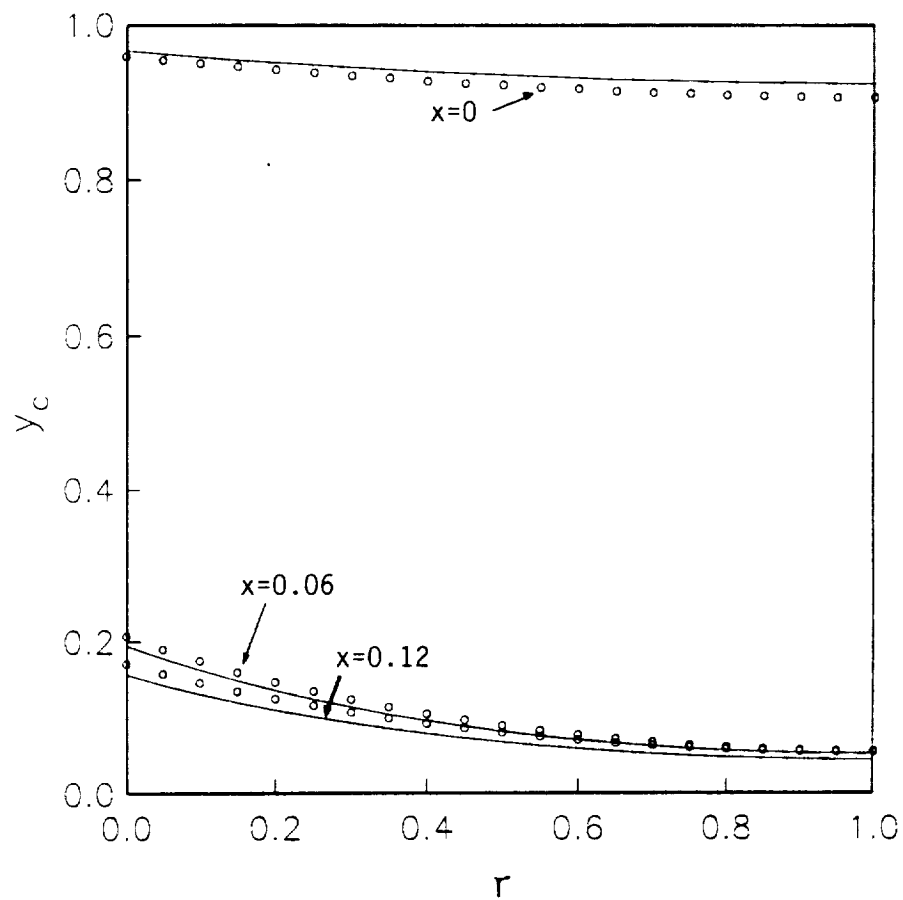


Figure 39 : Comparisons of two models for Case 1 on solid in-depth temperature at  $t = 1 \tau_{HT}$   
 Solid line : full transient model  
 Symbol  $\circ$  : energy integral model



**Figure 40 :** Comparisons of two models for Case 1 on solid in-depth species at  $t = 1 \tau_{HT}$   
 Solid line : full transient model  
 Symbol  $\circ$  : energy integral model

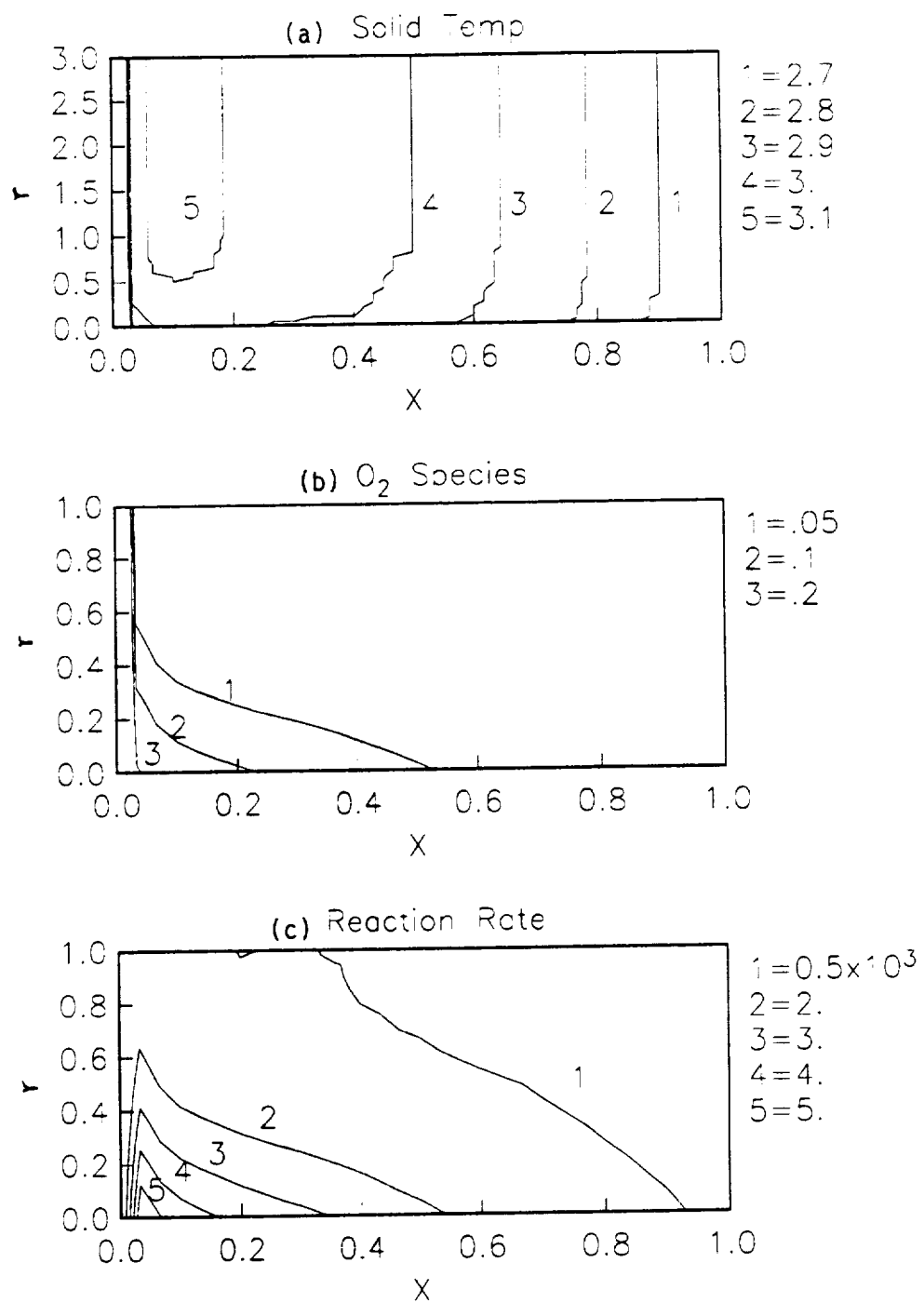


Figure 41 : Solid contours for Case 1 at  $t^* = 2 \tau_{HT}^*$   
by energy integral model

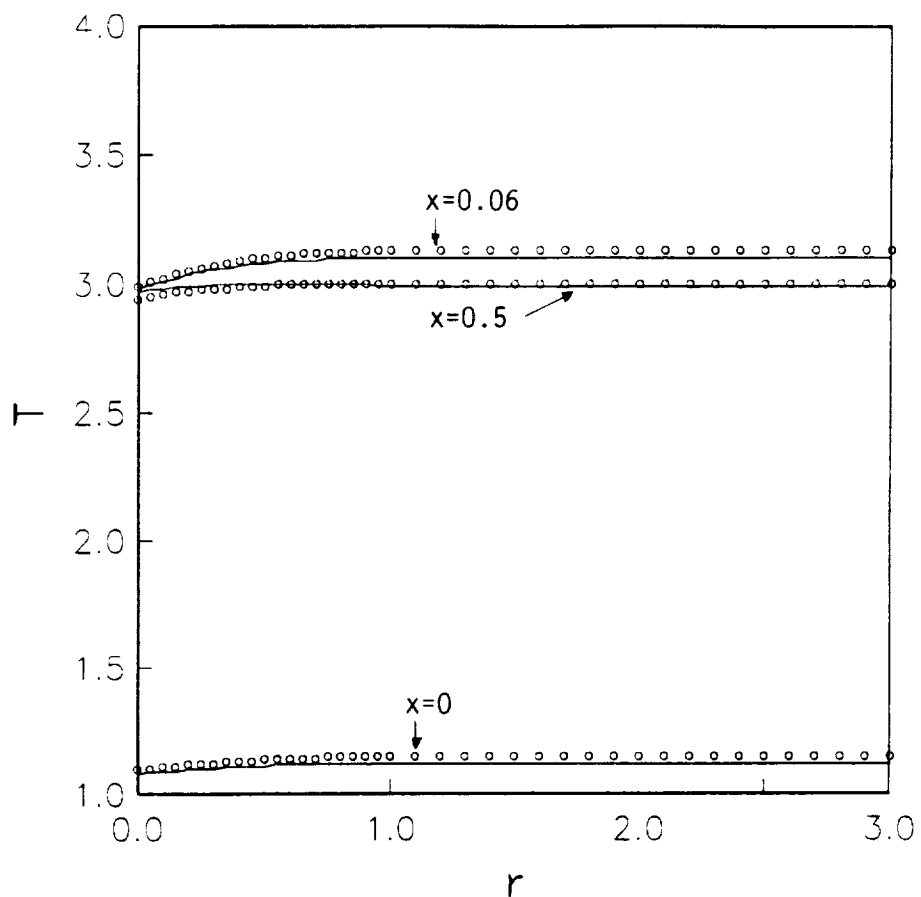
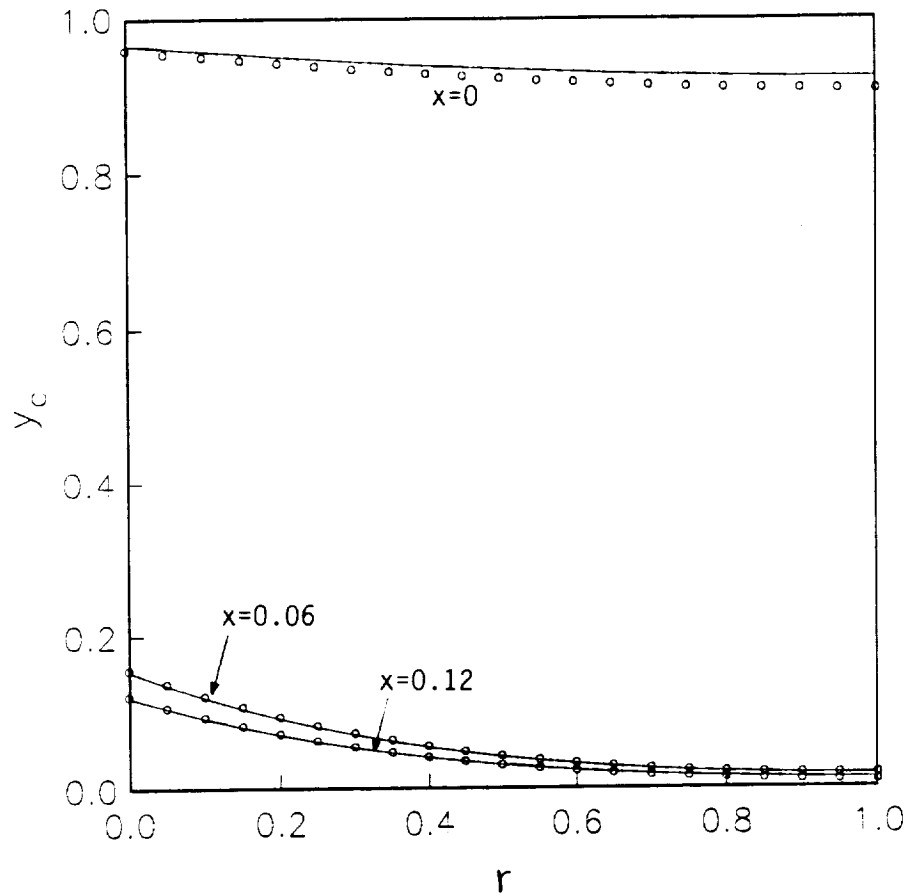


Figure 42 : Comparisons of two models for Case 1 on solid in-depth temperature at  $t = 2 \tau_{HT}$   
 Solid line : full transient model  
 Symbol  $\circ$  : energy integral model



**Figure 43 :** Comparisons of two models for Case 1 on solid in-depth species at  $t = 2 \tau_{HT}$   
 Solid line : full transient model  
 Symbol  $\circ$  : energy integral model

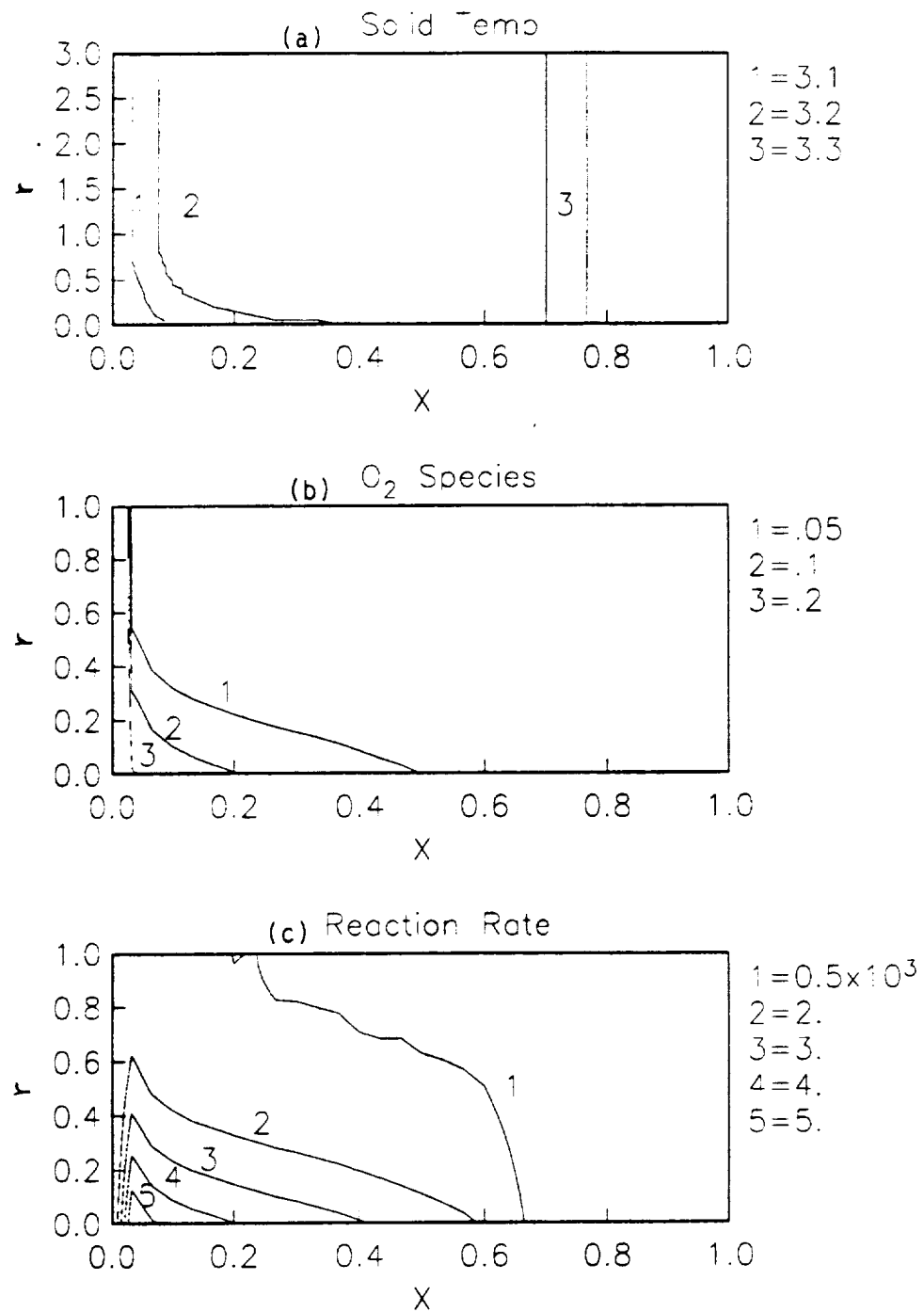


Figure 44 : Solid contours for Case 1 at  $t = 3 \tau_{\text{HT}}^*$   
by energy integral model

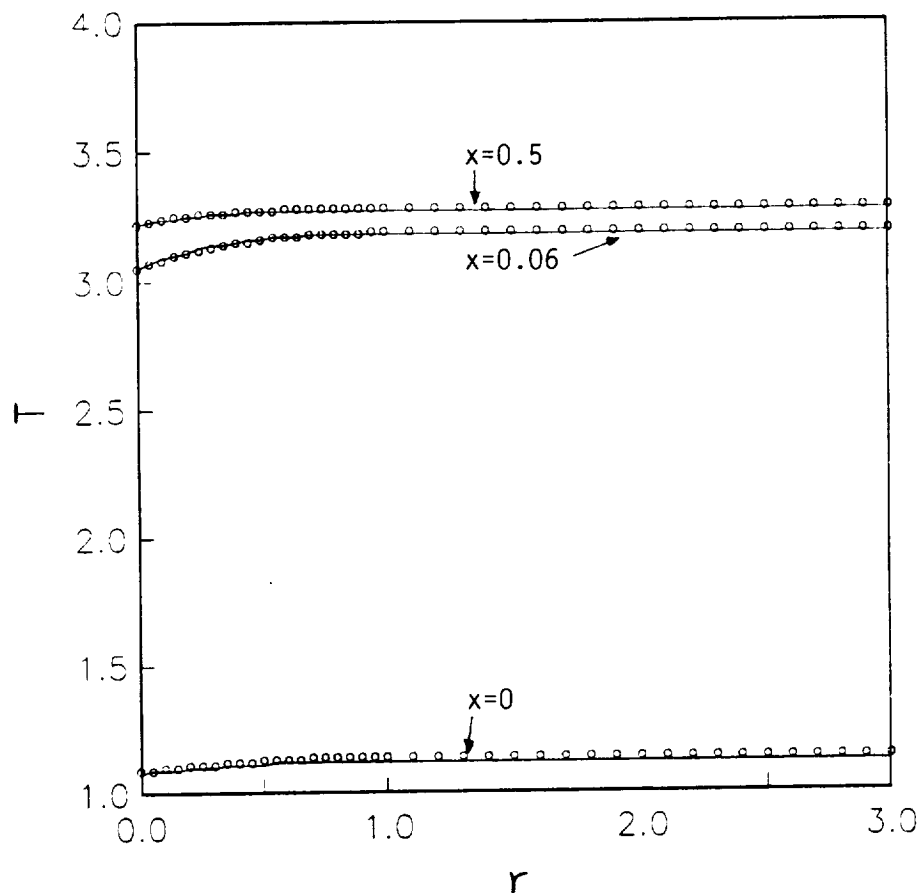
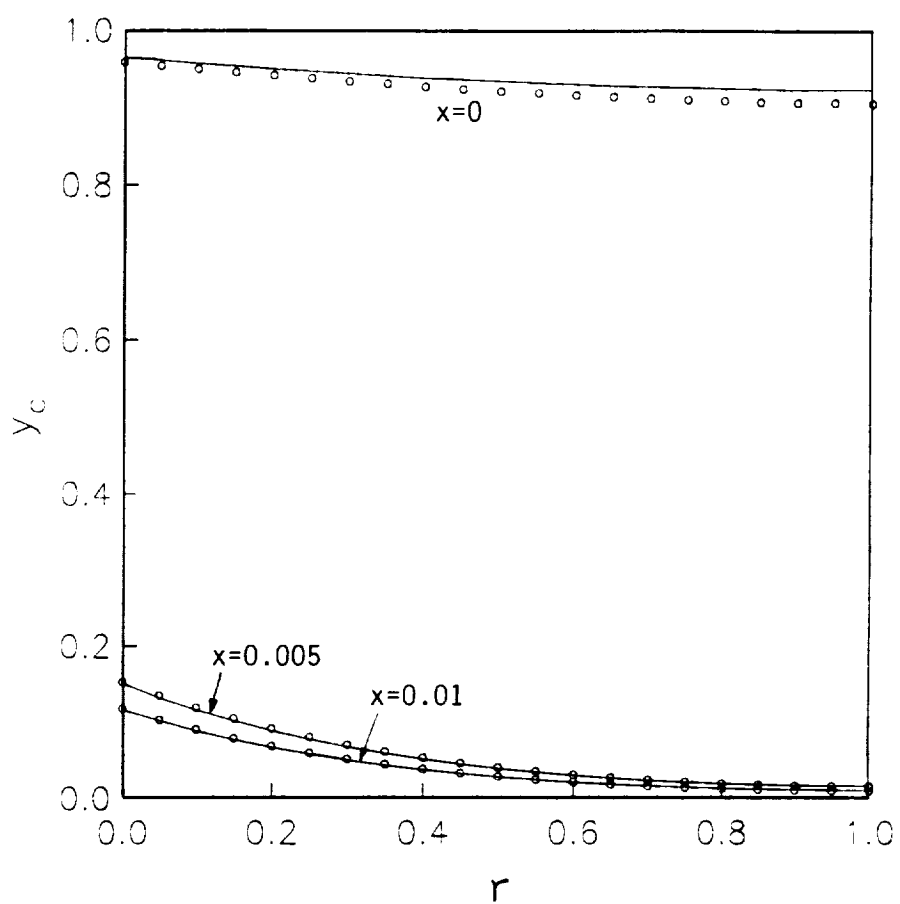
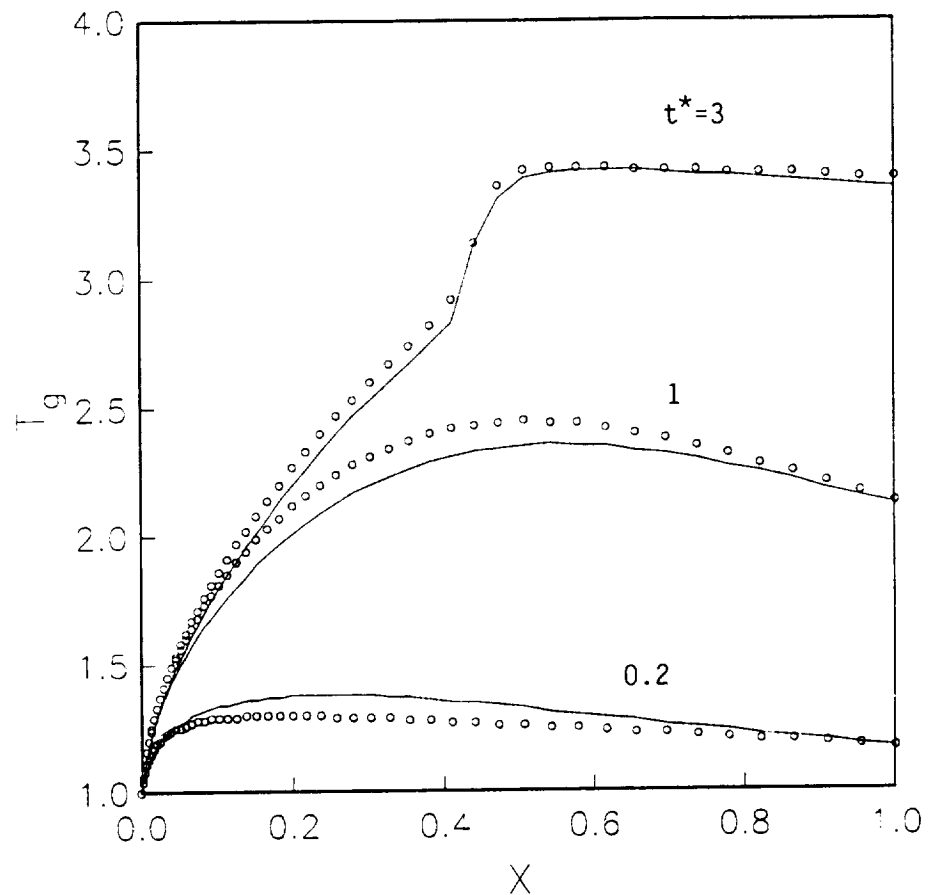


Figure 45 : Comparisons of two models for Case 1 on solid in-depth temperature at  $t = 3 \tau_{HT}$   
Solid line : full transient model  
Symbol  $\circ$  : energy integral model



**Figure 46 :** Comparisons of two models for Case 1 on solid in-depth species at  $t = 3 \tau_{HT}$   
**Solid line :** full transient model  
**Symbol o :** energy integral model



**Figure 47 :** Comparisons of two models for Case 3 on  $T_t$  at  $t = 0.2, 1, 3 \tau_{HT}$   
 Solid line : full transient model  
 Symbol  $\circ$  : energy integral model

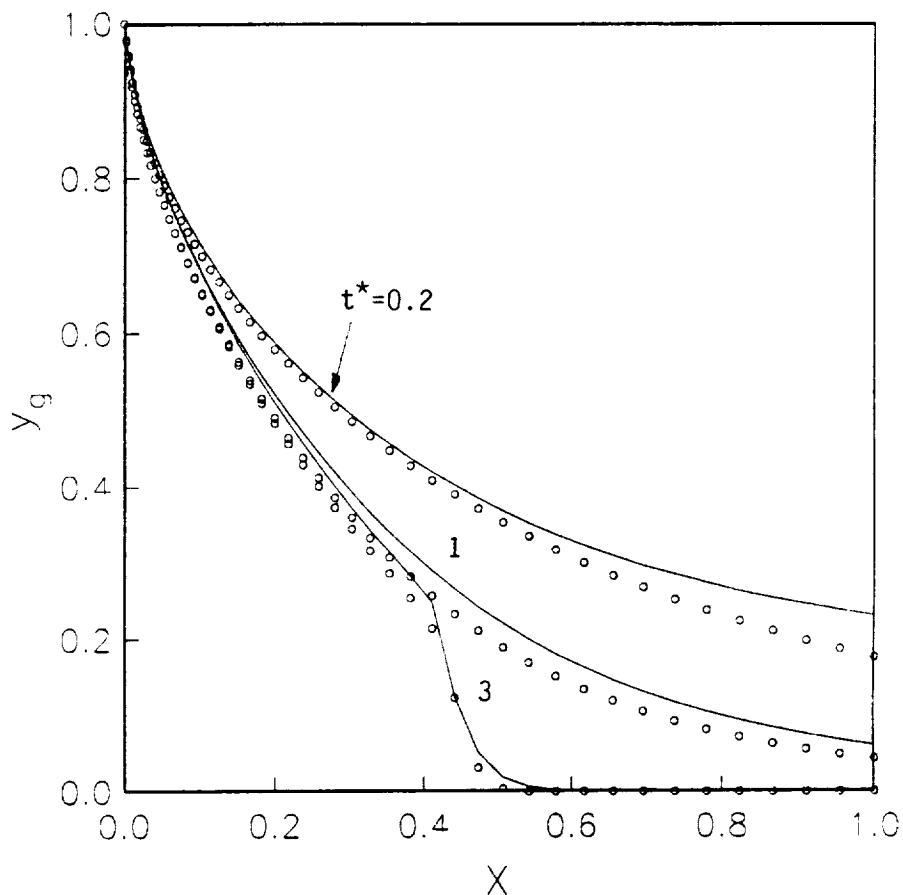


**Figure 48 : Comparisons of two models for Case 3 on  $y_g$  at  $t = 0.2, 1, 3 \tau_{HT}$**

Solid line : full transient model

Symbol  $\circ$  : energy integral model

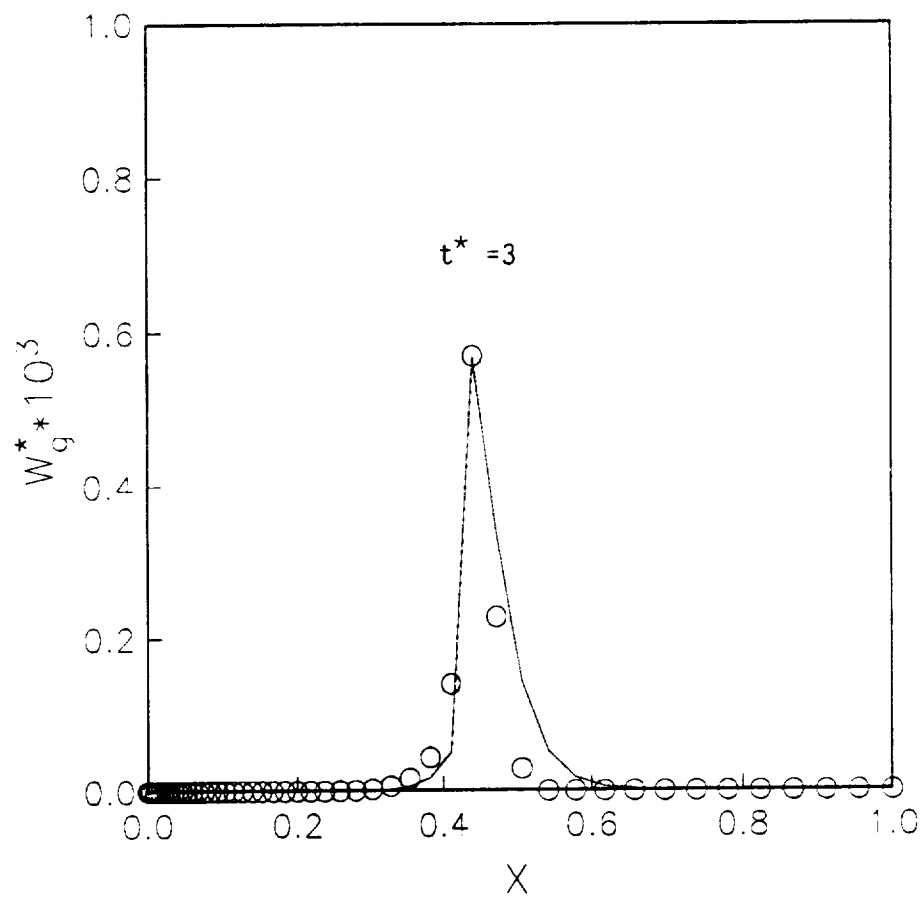
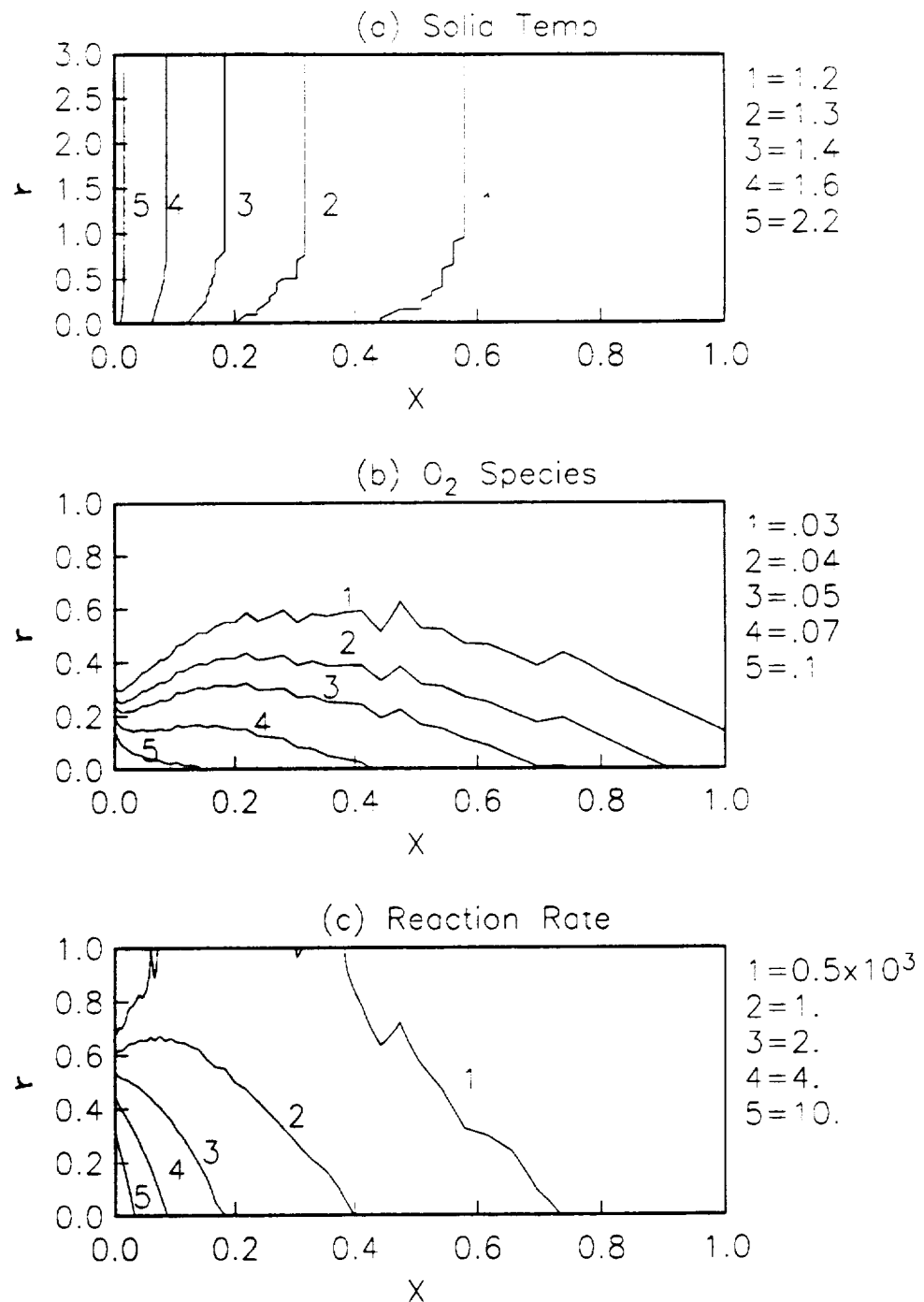


Figure 49 : Comparisons of two models for Case 3 on  $W_q^*$   
at  $t = 0.2, 1, 3 \tau_{HT}$   
Solid line : full transient model  
Symbol  $\circ$  : energy integral model



**Figure 50 :** Solid contours for Case 3 at  $t^* = 0.2 \tau_{HT}^*$   
by energy integral model  
Solid line : full transient model  
Symbol  $\circ$  : energy integral model

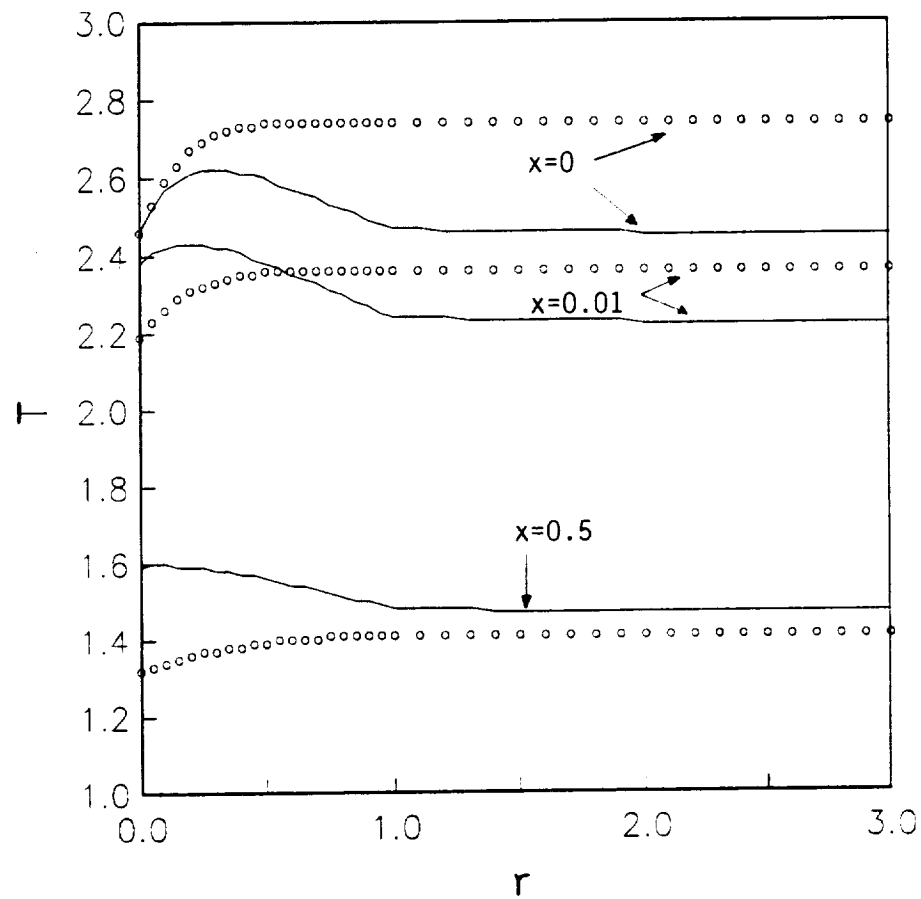
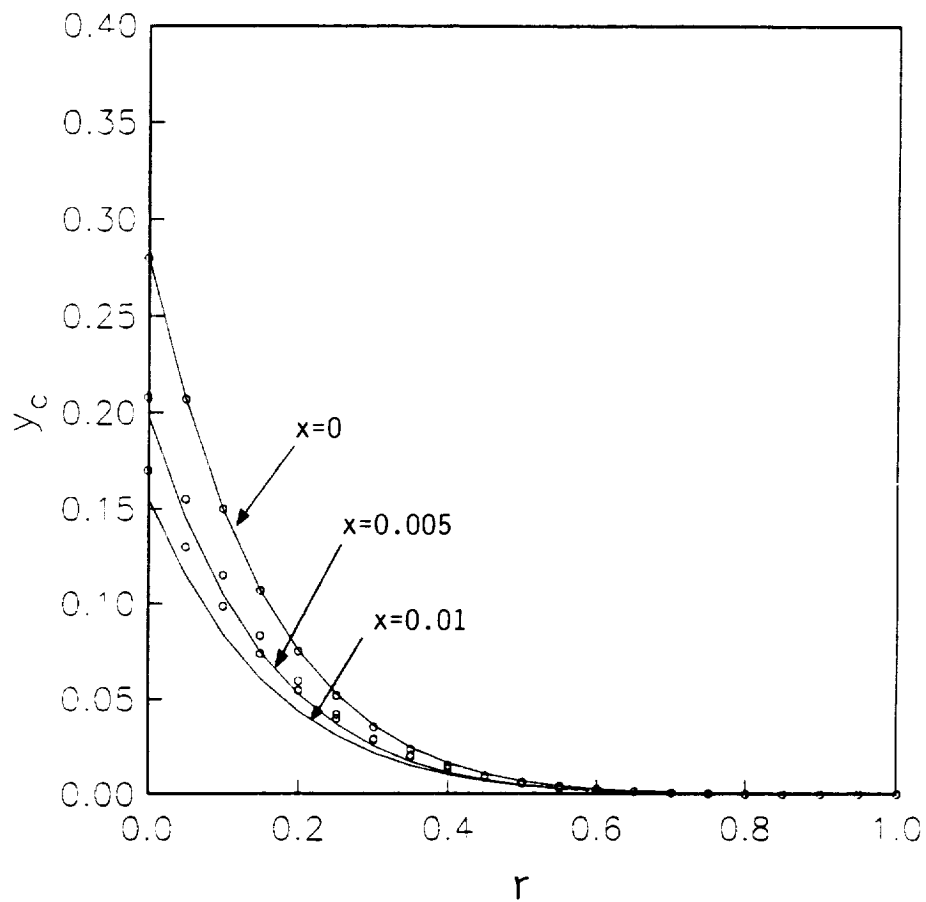


Figure 51 : Comparisons of two models for Case 3 on solid in-depth temperature at  $t = 0.2 \tau_{HT}$   
 Solid line : full transient model  
 Symbol  $\circ$  : energy integral model



**Figure 52 :** Comparisons of two models for Case 3 on solid in-depth species at  $t = 0.2 \tau_{HT}$   
 Solid line : full transient model  
 Symbol  $\circ$  : energy integral model

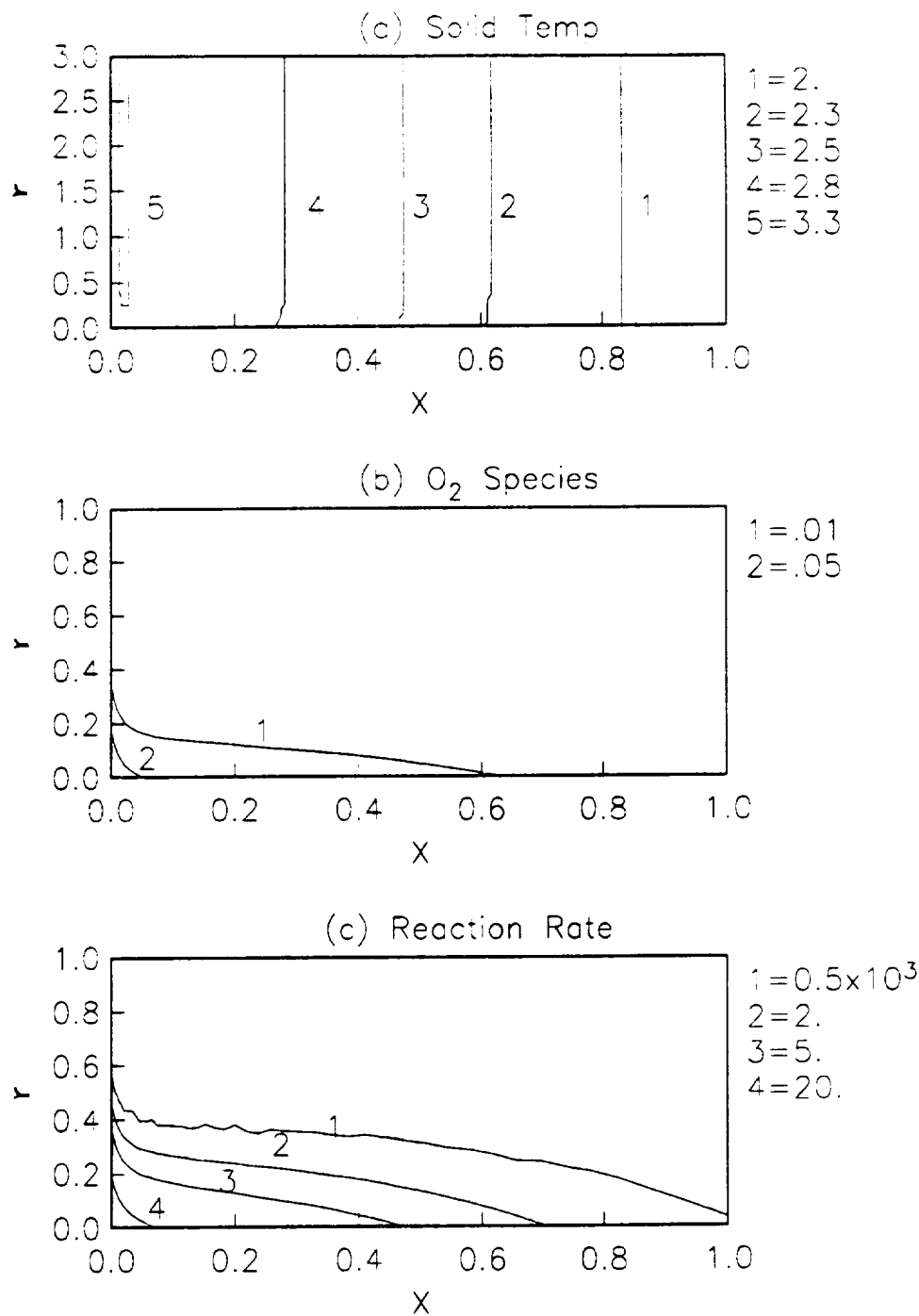


Figure 53 : Solid contours for Case 3 at  $t^* = 1 \tau_{HT}^*$   
by energy integral model

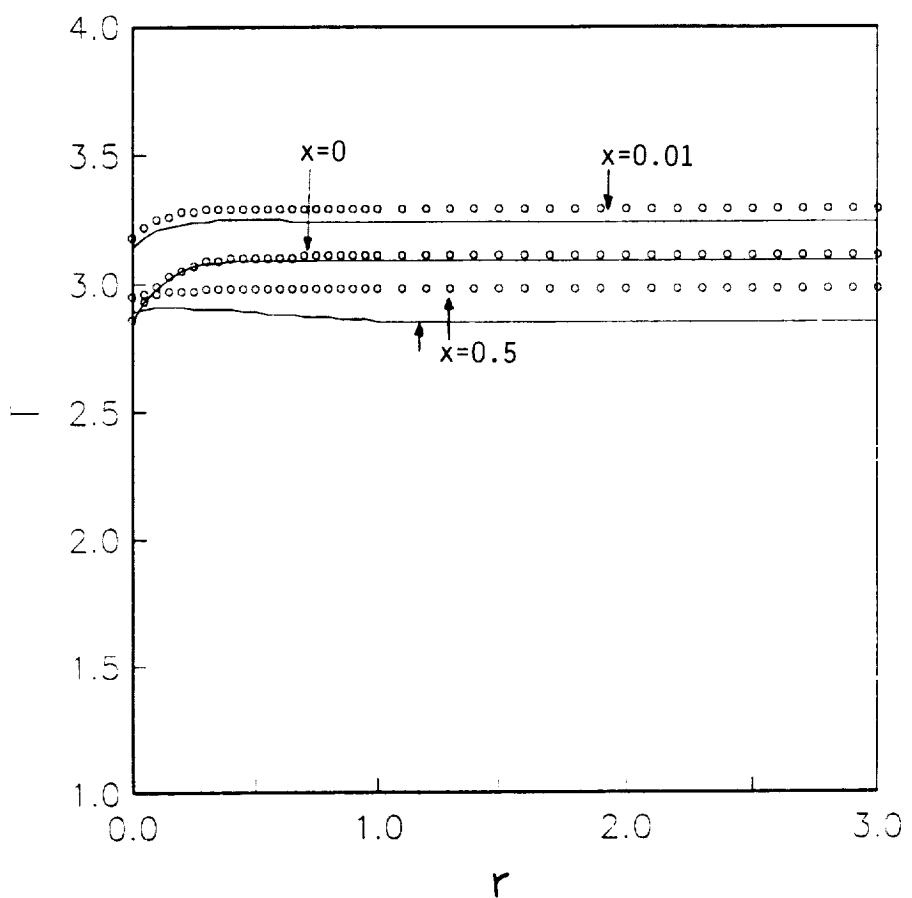
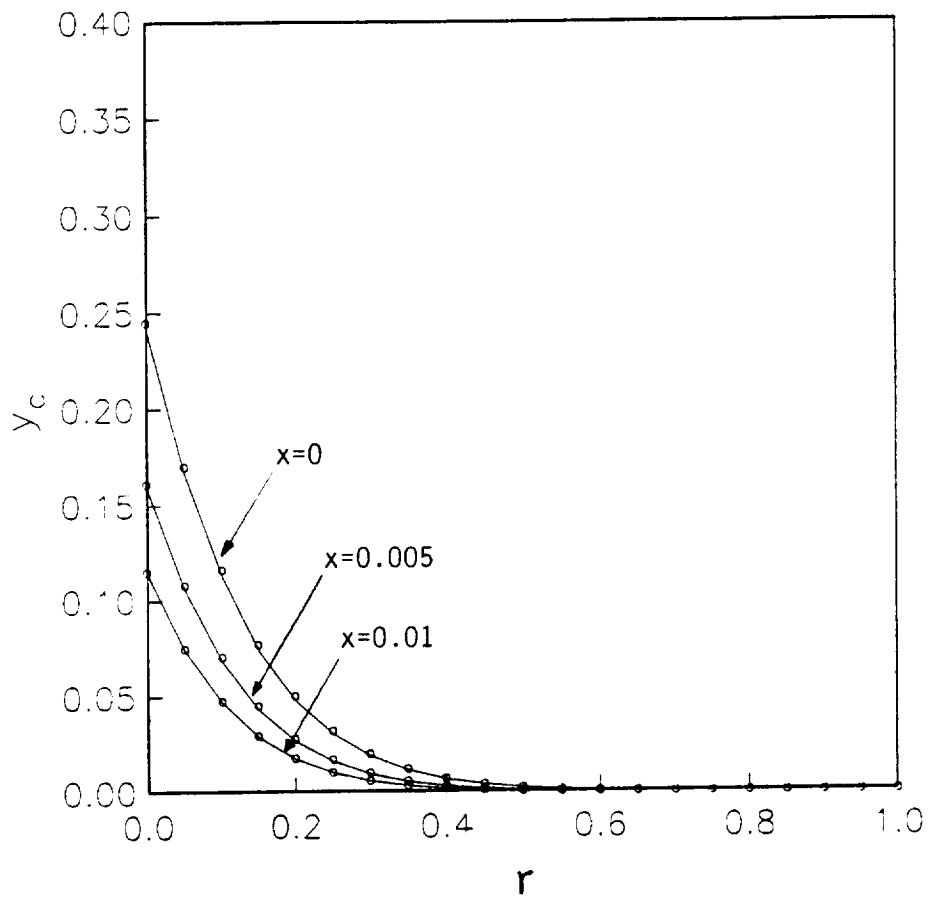
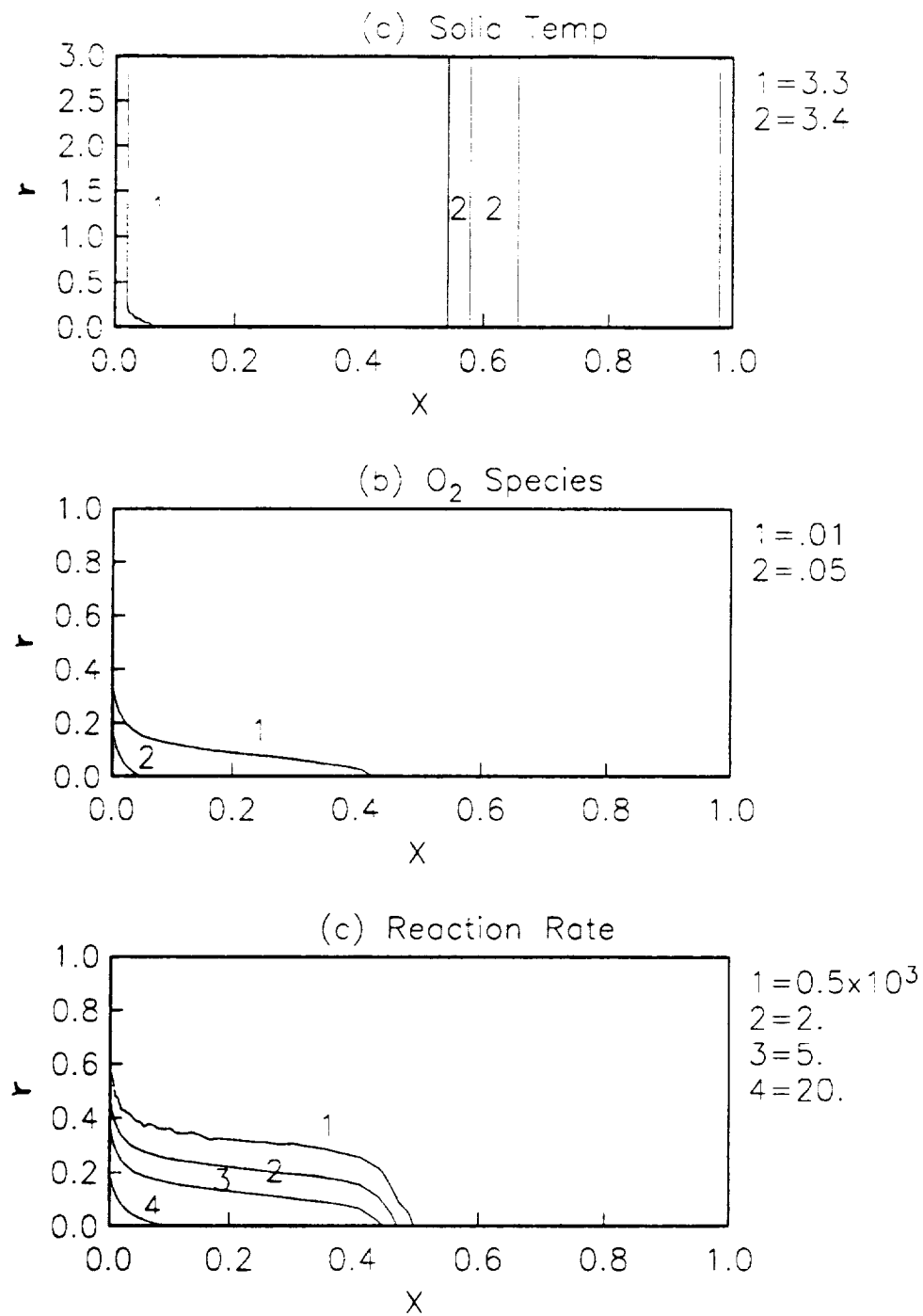


Figure 54 : Comparisons of two models for Case 3 on solid  
in-depth temperature at  $t = 1 \tau_{HT}$   
Solid line : full transient model  
Symbol  $\circ$  : energy integral model



**Figure 55 :** Comparisons of two models for Case 3 on solid in-depth species at  $t = 1 \tau_{HT}$

Solid line : full transient model  
 Symbol  $\circ$  : energy integral model



**Figure 56 :** Solid contours for Case 3 at  $t^* = 3 \tau_{HT}^*$  by energy integral model

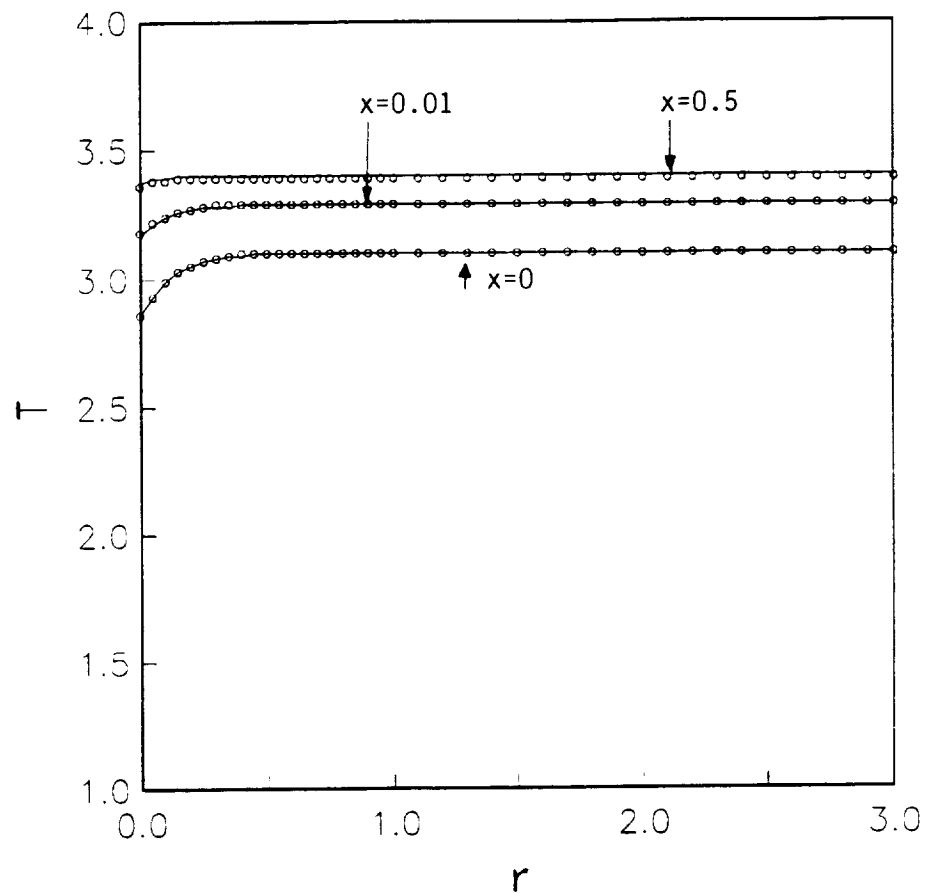
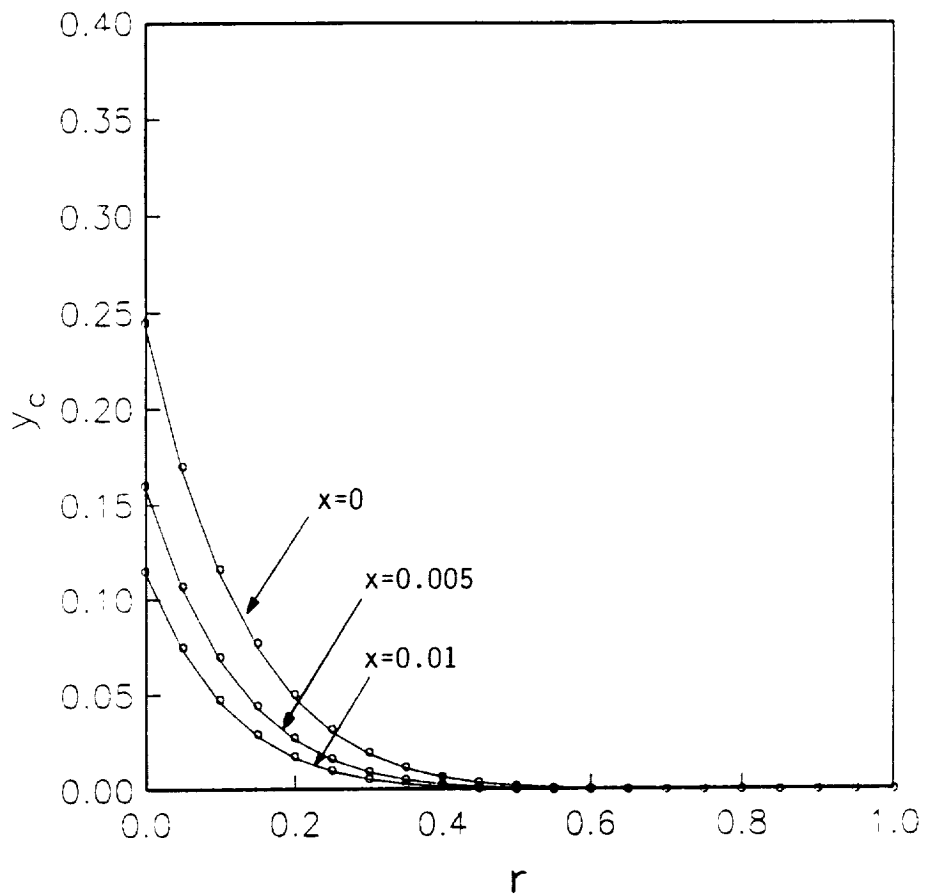


Figure 57 : Comparisons of two models for Case 3 on solid in-depth temperature at  $t = 3 \tau_{HT}$   
 Solid line : full transient model  
 Symbol  $\circ$  : energy integral model



**Figure 58 :** Comparisons of two models for Case 3 on solid in-depth species at  $t = 3 \tau_{HT}$   
 Solid line : full transient model  
 Symbol  $\circ$  : energy integral model

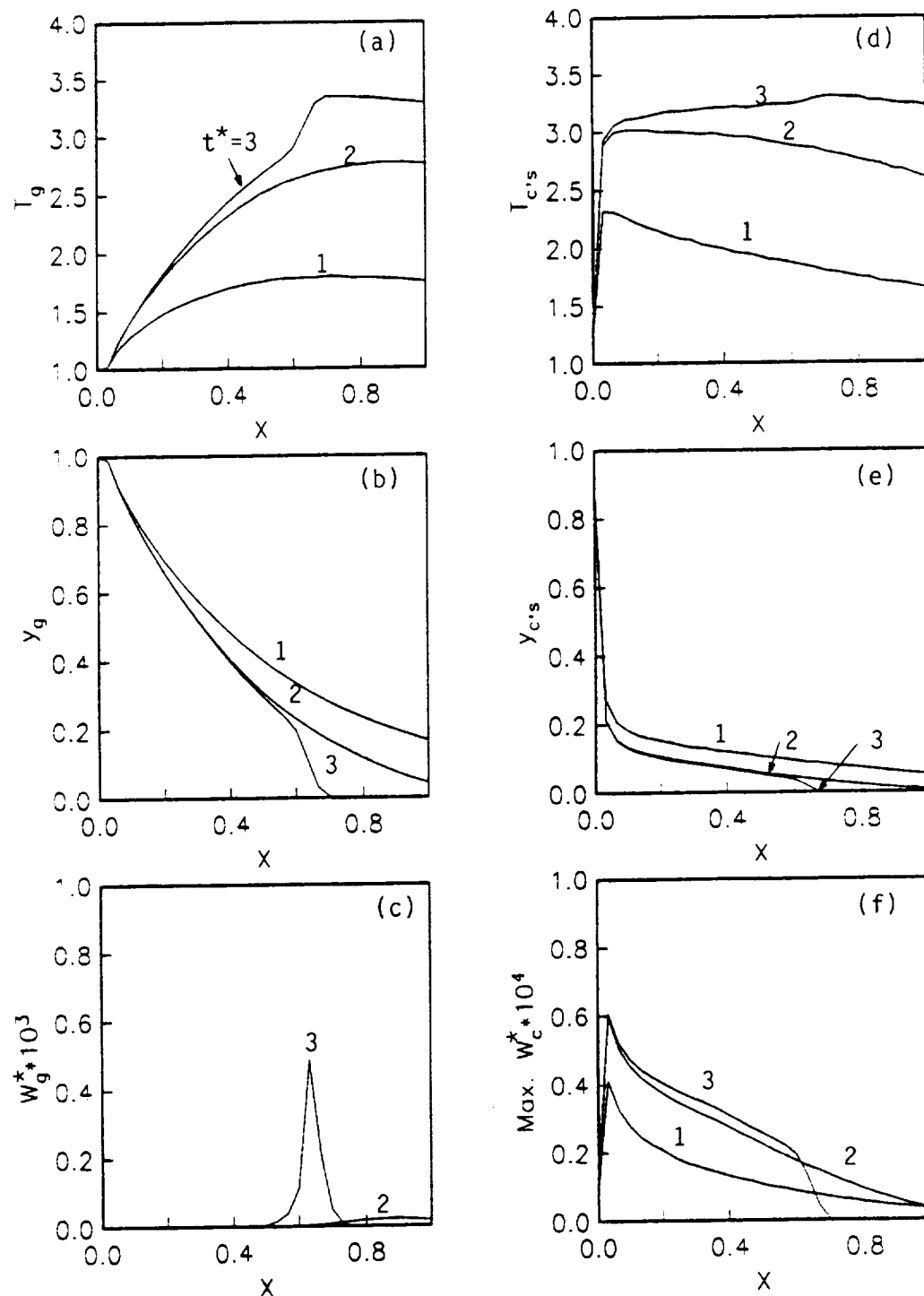
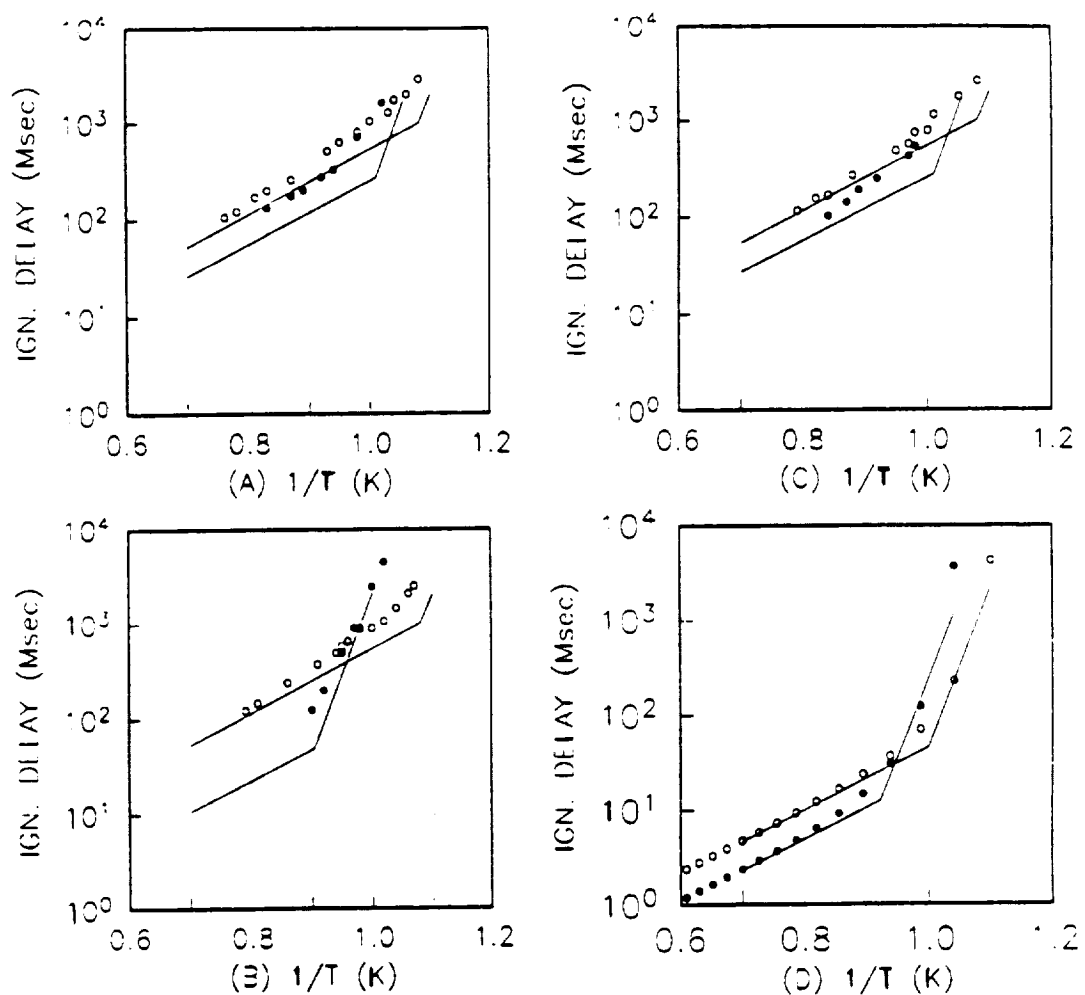


Figure 59 : Transient profiles for Case 5 at  $t^* = 1, 2, 3 \tau_{HT}^*$   
 $(\beta^* = 1.8 \text{ kg-pt/m}^3, L^* = 5 \text{ cm}, \phi = 8, \tau_{HT}^* = 2 \text{ sec})$



**Figure A.1 :** Comparisons of ignition delay time between model predicted by Eqs. (A.10), (A.11) and experimental data [14], [15].

Solid line : Model prediction

- (A) 4% Hz, 2% O<sub>2</sub>,  $\circ$  :  $p = 1$ ,  $\bullet$  :  $p = 2$  atm
- (B) 8% Hz, 2% O<sub>2</sub>,  $\circ$  :  $p = 1$ ,  $\bullet$  :  $p = 5$  atm
- (C) 12% Hz, 2% O<sub>2</sub>,  $\circ$  :  $p = 1$ ,  $\bullet$  :  $p = 2$  atm
- (D) 67% Hz, 33% O<sub>2</sub>,  $\circ$  :  $p = 1$ ,  $\bullet$  :  $p = 2$  atm

